

INFLUENCE OF GRAIN MISORIENTATION ON GRAIN  
GROWTH IN NANOCRYSTALLINE  
METALS

by

JUSTIN GLEN BRONS

GREGORY B. THOMPSON, COMMITTEE CHAIR

VIOLA L. ACOFF

MARK L. WEAVER

JINHUI SONG

LEILA J. LADANI

AMBER L. GENAU

A DISSERTATION

Submitted in partial fulfillment of the requirements  
for the degree of Doctor of Philosophy in the  
Department of Metallurgical and Materials  
Engineering in the Graduate School of  
The University of Alabama

TUSCALOOSA, ALABAMA

2013

Copyright Justin Glen Brons 2013  
ALL RIGHTS RESERVED

## ABSTRACT

It is well known that the grain size of a material controls its properties, including mechanical strength, electrical conduction, and corrosion resistance. Typically, a fine grain size is desirable, since it allows for these properties to be increased. Nanocrystalline materials have been engineered in order to maximize the benefits associated with this fine grain size. Unfortunately, the high density of grain boundaries for a given volume of the material leads to an increase in the excess energy that is associated with grain boundaries. This excess energy can act as a driving force for grain growth, which causes these nanocrystalline structures to be unstable, with this grain growth often times being detrimental to the material properties. This research investigated the influence of grain boundary mobility and the applied driving force on grain growth in nanocrystalline metal films by focusing on the role grain boundary misorientation plays in regulating grain growth. This was accomplished by completing two types of studies: (i) Annealing sputter-deposited thin films to study mobility in a case where the driving force is assumed to be dominated by grain boundary curvature and (ii) Mechanically indenting thin films with different microstructural features while submerged in liquid nitrogen. In terms of the latter study, the mobility was expected to be extremely low due to the cryogenic temperatures. Both sets of films were then characterized using precession-enhanced diffraction-based orientation analysis in the transmission electron microscope to quantify the evolution in grain size, grain morphology, and in the grain-to-grain misorientation.

## DEDICATION

For my loving wife and my supportive family, you drive me to be better each day.

## LIST OF ABBREVIATIONS AND SYMBOLS

Ag	Silver
AGG	Abnormal grain growth
Al	Aluminum
B	Binding energy
b	Burgers vector
CCD	Charge-coupled device
CINT	Center for Integrated Nanomaterials
CSL	Coincidence site lattice
Cu	Copper
DOE	Department of Energy
E	Elastic modulus (Young's modulus)
EBSD	Electron backscatter diffraction
EDS	Energy dispersive spectroscopy
FCC	Face-centered cubic
g	Grams
GBCD	Grain boundary character distribution
HOLZ	Higher-order Laue zone
Hz	Hertz
J	Joules

K	Degrees Kelvin
keV	Kiloelectron volts
M	Average grain boundary mobility
m	Meters
mJ	Millijoules
N	Newtons
n	Growth exponent
Ni	Nickel
nm	Nanometer
OIM	Orientation Imaging Microscopy
P	Driving force
PED	Precession-enhanced diffraction
PIPS	Precision ion polishing system
PLD	Pulsed laser deposition
R	Diameter of considered grain
$R_c$	Critical grain diameter
$R_m$	Mean grain radius
ROI	Region of interest
SEM	Scanning electron microscope
SFE	Stacking fault energy
t	Time

T	Temperature
$T_m$	Melting temperature
TEM	Transmission electron microscope
XRD	X-ray diffraction
$\gamma_{GB}$	Average grain boundary energy
$\gamma_s$	Elastic work done to create a free surface
$\Delta$	Change in
$\Delta\gamma$	Difference in average surface energy of abnormal and normal grains
$\Delta F$	Driving force for abnormal grain growth
$\epsilon_{yx}$	Shear strain
$\kappa$	Temperature dependent constant
$\mu$	Dislocation energy
$\rho$	Dislocation density
$\Sigma$	Coincidence site lattice value
$\tau$	Elastic stress
=	Equals
$\approx$	Approximately equal to
%	Percent
°	Degree
>	Greater than
<	Less than

## ACKNOWLEDGMENTS

I am pleased to have this opportunity to thank the colleagues, friends, and faculty members who have helped with this research project. I am most indebted to Professor Gregory Thompson, the chairman of this thesis and my research adviser, for sharing his expertise and wisdom regarding materials research. I would also like to thank all of my committee members, Professors Viola Acoff, Mark Weaver, Jinhui Song, Leila Ladani, and Amber Genau for their invaluable input, inspiring questions, and support of both the dissertation and my academic progress.

I would like to recognize the National Science Foundation for their financial support for my research through grant number EPS08-14103 and Sandia National Laboratories for supporting my work through the Department of Energy, Office of Basic Sciences. I also appreciate the use of the general user facilities in the Central Analytical Facility (CAF). I would like to thank my collaborators at Sandia National Laboratories in Albuquerque, NM: Dr. Brad Boyce, Dr. Henry Padilla, and Dr. Khalid Hatter.

Finally, I would like to thank my fellow colleagues: Mr. Chad Hornbuckle, Mr. Nicholas De Leon, and Mr. Bradford Schulz for discussions relating to TEM micrograph interpretation and FIB specimen preparation, the graduate students in Thompson's Research Group, and a special thanks to the Department of Metallurgical Engineering and CAF Staff for all the background work that kept my research productive.

## TABLE OF CONTENTS

ABSTRACT.....	ii
DEDICATION.....	iii
LIST OF ABBREVIATIONS AND SYMBOLS .....	iv
ACKNOWLEDGMENTS .....	vii
LIST OF TABLES.....	xi
LIST OF FIGURES .....	xii
1. INTRODUCTION .....	1
1.1 Motivation.....	1
1.2 Curvature Driven Grain Growth .....	3
1.3 Mechanical Driving Forces.....	5
1.4 Thin Films – A Special Case .....	7
1.5 Grain Boundary Character .....	9
1.6 Twin Boundary Motion .....	12
1.7 Precession-Enhanced Diffraction Orientation Analysis .....	15
2. A COMPARISON OF GRAIN BOUNDARY EVOLUTION.....	20
2.1 Abstract.....	20
2.2 Introduction.....	21
2.3 Experimental .....	25
2.4 Results.....	28

2.5 Discussion .....	37
2.6 Conclusions.....	43
2.7 Acknowledgements.....	44
2.8 References.....	44
3. STUDYING THE EFFECTS OF NICKEL ADDITIONS .....	48
3.1 Abstract.....	48
3.2 Introduction.....	49
3.3 Experimental .....	51
3.4 Results.....	52
3.5 Discussion .....	57
3.6 Conclusions.....	61
3.7 Acknowledgements.....	62
3.8 References.....	62
4. CRYOGENIC INDENTATION-INDUCED GRAIN GROWTH .....	65
4.1 Abstract.....	65
4.2 Introduction.....	66
4.3 Experimental .....	67
4.4 Results.....	70
4.5 Discussion .....	72
4.6 Conclusions.....	78
4.7 Acknowledgements.....	78

4.8 References.....	79
5. THE ROLE OF TWIN BOUNDARIES IN GRAIN GROWTH .....	80
5.1 Abstract.....	80
5.2 Introduction.....	81
5.3 Experimental.....	84
5.4 Results.....	87
5.5 Discussion.....	95
5.6 Conclusions.....	104
5.7 Acknowledgements.....	105
5.8 References.....	105
6. CONCLUSIONS AND FUTURE WORK.....	109
7. REFERENCES .....	113
8. APPENDICES .....	118
8.1 Appendix A. Procedure for nanoMEGAS ASTAR.....	117
8.2 Appendix B. Preparation of PED-Ready TEM Foils.....	136

## LIST OF TABLES

2.1 Selected Material Properties for the Metals Studied .....	26
---	----

## LIST OF FIGURES

1.1 $\Sigma 5$ CSL Boundary in two different, symmetrical, rotations .....	10
1.2 Graphical Representation of Precession Enhanced Diffraction.....	17
2.1 Evolution of Cu Microstructure during Annealing.....	29
2.2 Evolution of Ni Microstructure during Annealing .....	30
2.3 Texture Evolution with Temperature.....	31
2.4 Cumulative Grain Size Distribution Functions for Cu and Ni.....	33
2.5 CSL Boundary Evolution with Temperature .....	35
2.6 Twin Boundary Evolution in Cu.....	38
2.7 Evolution of Ni Grains at Various Temperatures .....	42
3.1 PED Orientation Maps for a Cu(Ni) Alloyed Thin Film .....	53
3.2 Cumulative Grain Size Distribution Plot for Cu(Ni) .....	55
3.3 Evolution of CSL Boundary Fractions in Cu(Ni).....	56
3.4 Cu(Ni) PED Orientation Maps with CSL Boundaries Overlaid.....	58
4.1 Cross-Sectional Schematic of Indentation Apparatus .....	69
4.2 As-Deposited Nanotwinned Cu Film in Cross-Section .....	71
4.3 Indented Nanotwinned Cu Film in Cross-Section .....	73
4.4 Region Specific Response of Nanotwinned Cu to Indentation.....	74
5.1 X-Ray Diffraction Pole Figures from the Nanotwinned Cu Film .....	86
5.2 Undeformed $\langle 100 \rangle$ Nanotwinned Cu Film in Cross Section.....	88

5.3 Undeformed Nanostructured Cu Film in Cross Section .....	90
5.4 Representative Indent after Cryogenic Indentation .....	91
5.5 Indented <100> Nanotwinned Cu Film in Cross Section .....	93
5.6 Indented Nanostructured Cu Film in Cross Section .....	94
5.7 Cumulative Grain Size Plots for the Different Regions .....	96
5.8 CSL Boundary Fractions for the Different Regions .....	99
A.1 nanoMEGAS Desktop Showing Digistar Control Software.....	118
A.2 Digistar Control Software Platform Showing Beam Scan.....	119
A.3 nanoMEGAS's Red Software Interface.....	121
A.4 nanoMEGAS's Red Software Scanning Control.....	123
A.5 nanoMEGAS's Grey Software Template Bank Creation .....	124
A.6 nanoMEGAS's Green Software How to Open an Image .....	126
A.7 nanoMEGAS's Green Software How to Select a Pattern .....	127
A.8 nanoMEGAS's Green Software How to Add Templates .....	128
A.9 nanoMEGAS's Green Software How to Optimize Center .....	129
A.10 nanoMEGAS's Green Software Camera Length.....	130
A.11 nanoMEGAS's Green Software How to Optimize Distortion.....	131
A.12 nanoMEGAS's Green Software How to Index Block File .....	132
A.13. nanoMEGAS's White Software How to View Indexed Maps .....	133
A.14 nanoMEGAS's White Software How to Export to *.ang .....	134

# CHAPTER 1

## INTRODUCTION

### 1.1 Motivation

Understanding and controlling grain growth is important to nearly every engineered material [1-4]. For materials that rely on strength, toughness, or formability, including most nanocrystalline materials, a stable, fine grain size is desirable [1]. For example, the mechanical strength of a metallic material can be significantly increased by grain size refinement [2]. Classically, this has been shown through the Hall-Petch relationship [5], but researchers have demonstrated the ability to synthesize and implement nanocrystalline grain structures, which are inherently governed by a different set of mechanisms. In addition to the improvements associated with these nanocrystalline length scales, researchers have been able to tailor the structure of materials to meet certain property requirements. An example of this is the inclusion of twin boundaries in nanocrystalline grains in order to improve the electrical conduction of Cu [6]. In addition to the size of the grains, the texture and orientation of the grains have been shown to dominate strength, as well as electrical and magnetic properties in polycrystalline materials [3]. Therefore, controlling both texture and grain orientation is equally important in optimizing property performance [3].

Grain growth occurs through the migration of grain boundaries, and the velocity of these migrating grain boundaries is typically represented by the product of a driving force and grain boundary mobility. Driving forces for this grain boundary migration can originate from a variety

of sources, including stored deformation energy, grain boundary energy, surface energy, elastic energy, or chemical and/or thermal gradients [4]. The mobility term in determining grain boundary motion is, simply stated, the means for atoms to diffuse in order to reduce the applied driving force. One can imagine that in order for a grain boundary to migrate within a polycrystalline material, the atoms in front of the leading edge of the boundary would need to move out of their current lattice positions and into new positions that match the lattice sites of the growing grain. This motion would then allow the boundary to progress one atomic diameter at a time [7].

In some cases, specific grains can grow more rapidly than others, leading to a small subset of large grains contained with a matrix of much smaller grains. This behavior is referred to as abnormal grain growth (AGG). In nanocrystalline materials, there is intrinsically a high density of grain boundaries per volume, as compared to coarse-grained materials. Because of the increased boundary content, there is excess energy associated with the grain structure of nanocrystalline materials. This excess energy can lead to grain instability, which in turn could be detrimental to the material properties, as was reported by Boyce and Padilla [8].

There were two main goals in this research. The first of these was to investigate the underpinnings of grain growth that occurs through the annealing of nanocrystalline metals, where the growth is driven by grain boundary curvature. The second goal was to investigate the underpinnings of grain growth that occurs as a function of nano-indentation within liquid nitrogen. In this second case, the driving force is high from the mechanical indentation, but the cryogenic temperatures should limit the grain boundary mobility.

## 1.2 Curvature Driven Grain Growth

Normal grain growth is considered a self-similar event, which simply means that the features (or in the case of a polycrystalline system, the grains) change in size in a uniform manner. It is typically characterized by an increase in the mean grain size with a simultaneous decrease in the total grain boundary length, which leads to a minimization in the total interfacial energy [9]. Analytical models for normal grain growth have been developed by researchers such as Hillert, Louat, and Zinke-Allmang [9-11] and are based on the particle coarsening theory. The concurrent result of such models is that the evolution of the mean grain size follows a scaling law:

$$(R_m)^n = Kt \quad [\text{Eq.1}]$$

where  $R_m$  is the mean grain radius,  $n$  is the growth exponent,  $K$  is a temperature dependent constant, and  $t$  is the time [10]. In particular, Hillert [9] proposed that for an individual grain, the rate of the normal growth could be approximated by

$$\frac{dR}{dt} = \frac{M\gamma_{gb}}{2} \left( \frac{1}{R_c} - \frac{1}{R} \right) \quad [\text{Eq.2}]$$

where  $M$  is average grain boundary mobility,  $\gamma_{gb}$  is average grain boundary energy,  $R_c$  is the critical grain diameter at which it neither grows or shrinks, and  $R$  is the diameter of the considered grain [9]. Therefore, this equation illustrates that the driving force is proportional to  $\gamma_{gb}/R$ , and the grain growth occurs as a function of the grain boundary energy and the grain boundary curvature.

Curvature-driven motion of grain boundaries leads to the lowering of the total surface area-to-volume ratio [12]. For example, an arbitrary element within a moving boundary does not typically sense a driving force for growth stemming from remote grain boundaries. Instead, the

force on this boundary element results from the curvature of the boundary. This curvature is caused by the fact that at the grain boundary junctions, mechanical equilibrium has been established, so any additional stress will cause the boundary to migrate via the induction of curvature [5]. A curved boundary then responds to a force by moving towards the center of the curvature in order to become straighter, thus reducing its area and in turn, its energy [5].

In contrast, during AGG, the grain size distribution does not remain self-similar. Rather, a bimodal distribution of grain sizes develops, where one of the modes is representative of the slowly growing grains, and the other mode represents the grains that have preferentially evolved to a larger size [5]. The distribution of the slowly growing grains will become smaller as the larger grains continue to evolve, and they will eventually disappear as they are consumed by the large, rapidly growing grains. Therefore, the AGG regime is characterized by only some of the grains growing larger at the expense of the smaller ones [13].

Typically, the curvature of a grain boundary is small, and this corresponds to the radius of the curvature being substantially larger than the grain size (by a factor of 5-to-10) [5]. Therefore, the driving force for normal grain growth is about 5 to 10 times smaller than it would be for AGG. Assuming that all grains have the same radius of curvature, the anisotropy in  $\gamma_{gb}$  would control which grains grow abnormally. To estimate the average excess energy of a grain boundary, the interface can be imagined by creating two free surfaces and then joining them together to form the boundary [14]. The grain boundary energy can then be written as

$$\gamma_{gb} = 2\gamma_s - B \quad [\text{Eq.3}]$$

where  $\gamma_s$  is the elastic work done to create a free surface (typically  $\sim (E/8) * 10^{-10}$  m, where E is the elastic modulus [14]) and B is the binding energy gained when two grain surfaces are brought together. Thus, the energy anisotropy from either  $\gamma_s$  or B arises because of differences in the

grain boundary structures. This grain boundary structure warrants a detailed microscopy-based study to provide the experimental inputs necessary to further develop these simple model concepts [14].

### **1.3 Mechanical Driving Forces**

When a grain in a metal is subjected to a mechanical load, dislocations propagate to allow for grain boundary motion, which is directly responsible for the grain growth necessary for deformation. While individual dislocation slip is still active in nanocrystalline metals with a grain size in the range of 20 to 50 nm [15-17], there is insufficient space for the collective dislocation interaction mechanisms found in coarse-grained metals, such as pileups and sub-grain formation. Instead, deformation is governed by dislocation nucleation and absorption at grain boundaries [16-19]. Boyce and Padilla [20] proposed that the persistent slip mechanism responsible for conventional fatigue crack initiation may be suppressed when the grain size is below a certain threshold, likely on the order of 100 nm or several hundred nanometers. This length scale threshold is between the grain sizes that could support collective dislocation activity and the grain sizes that could support individual dislocation activity. A survey of the available literature on the fatigue of nanocrystalline metals reveals that fatigue failure still occurs for nanocrystalline metals, often with nothing more than a modest improvement in performance over coarse-grained metals [21-22].

Perhaps the explanation for the lack of improvement in fatigue performance is related to the instability of nanocrystalline grain structures, which are even known to evolve during storage at room temperature [23]. The grain growth reported for fatigue experiments performed on nanocrystalline Cu by Witney *et. al.* [24] refers to modest overall grain growth, as opposed to the

discontinuous local coarsening observed in the monotonic loading experiments performed by Gianola *et al.* [25]. In addition, several numerical models exist to predict the evolution of nanocrystalline grain structures under both elastic [26, 27] and plastic [28-30] deformation. These observations are in agreement with the fact that nanocrystalline metals form coarse grain structures during fatigue loading and that fatigue mechanisms are influenced more by the evolved structure than by the initial.

Grain orientation can also have profound effects on growth behavior [31, 32], ranging from elastic mismatch accentuating the elastic driving force [26] to causing local variations in grain boundary mobility [33]. It is well known that the orientation of a face-centered cubic (FCC) single crystal rotates during uni-axial deformation [34] to take full advantage of available slip systems. Evidence of this is proposed in the conclusions of the experiments performed by Boyce and Padilla [20]. Their examination of the elongated coarse grains revealed the presence of several low-angle sub-boundaries, which may be remnants of previously existing smaller grains. This structure suggested a mechanism proposed by experimentation [35] and simulation [36, 37], in which neighboring grains under an external stress can rotate to a common orientation, effectively eliminating the high-angle grain boundaries between them and allowing collective dislocation mechanisms to occur.

In addition to traditional mechanically induced grain growth, Zhang *et al.* [38] have shown that growth can occur in nanocrystalline Cu films as a result of micro-indentation performed while the sample was submerged in liquid nitrogen. When the temperature is sufficient and a driving force is present, it is easily understood how and why a system would undergo grain growth; in the work by Zhang *et al.* [38], however, the mobility was significantly

hindered by the low temperature and the kinetics of grain growth are poorly understood. Additionally, the governing kinetics were not addressed in their experimental paper.

There have been a limited number of modeling simulations which have suggested that grain growth can occur as a function of mechanical loading, even in low temperature regimes. Sansoz and Dupont [39] and Battaile *et al.* [26] have modeled the case of stress-driven grain growth at 0 K. Both sets of researchers found that stress-driven grain growth is dominated by the elasticity, and in a lesser extent, the plastic strain in the material. The driving force for elastic energy is given as

$$P = \tau^2/2 (E_1^{-1} - E_2^{-1}) \quad [\text{Eq.4}]$$

where  $\tau$  is the elastic stress and  $E_1$  and  $E_2$  are the elastic moduli of neighboring grains. The plastic deformation energy is defined by  $P = \frac{1}{2} \rho \mu b^2$  where  $\rho$  is the dislocation density and  $\frac{1}{2} \mu b^2$  is the dislocation energy. Recent molecular dynamics simulations [12] of grain boundary motion have suggested that there are strong variations in mobility, especially at low temperatures. These mobilities will depend strongly on the grain boundary plane since the energy will be a function of the grain-to-grain misorientation angle [14]. Clearly, providing high fidelity experimental data on the evolution of grain boundary types is required to validate these simulations. This would provide the needed information to elucidate the governing mechanisms of grain growth under these driving forces and at low temperatures.

#### **1.4 Thin Films – A Special Case**

To study this phenomenon at the nanoscale, thin films can be investigated. They are extensively used in electronic materials, hard coatings, and optical coatings, making them a relevant study [2, 14, 39, 40]. To this point in the explanation of grain growth, AGG has been

considered to occur without specifying the geometry of the material. The dimensions of a thin film, however, must be considered when investigating grain growth. Grain growth in thin films is represented through a two-dimensional perspective. As a consequence, the influence of film height and surface (not grain boundary) energy must also be considered in the treatment of grain growth. Normal grain growth usually ceases when the grain size becomes comparable to the smallest specimen dimension, which in the case of thin films is the film thickness [5]. For the specific case of thin films, discontinuous growth of a few grains can be observed after continuous growth has come to an end.

The kinetic mechanisms of AGG, in thin films, were extensively studied by Thompson *et al.* [41-44]. In these models, the driving force for AGG,  $\Delta F$ , was approximated by

$$\Delta F \approx \frac{-(\gamma_{gb} + 2\Delta\gamma)}{h} \quad [\text{Eq.5}]$$

where  $h$  is the film thickness and  $\Delta\gamma$  is the difference between the average surface energy of abnormal grains and the average surface energy of normal grains. Therefore, the driving force in Equation 5 is different from that in Equation 2. The modification in driving force will need to be considered in this research, since nanocrystalline thin films are of interest.

Therefore, the fundamental scientific questions in the case of either thermal annealing or mechanical loading are: (1) How and what types of boundaries in nanocrystalline metals contribute to abnormal grain growth? (2) Does the growth occur at specific temperatures, preferentially in specific orientations or based on a particular curvature? (3) Since the material is crystalline, do specific orientations generate specific types of curvatures that are favorable for curvature driven growth in conditions, particularly when the thermal conditions are varied? A series of *in situ* and *ex situ* experiments were designed in order to investigate this grain growth behavior.

## 1.5 Grain Boundary Character

As described above, the grain boundary energy will dominate the grain growth behavior in the case of nanocrystalline materials. This energy is also directly related to the structure of the grain boundary. When some of the atomic sites in two crystals overlap in the boundary plane, a coincidence boundary can form and is used to describe specific orientations where the boundaries have “good fit,” typically associated with lower energies [14].

Coincidence site lattice (CSL) boundaries have been one of the most influential concepts in the study of grain boundaries during the past 60 years [14]. CSL misorientations are named by the inverse of the number of coincidence lattice sites in the grain boundary [14]. For example, considering a specific boundary in an FCC material, shown in Figure 1, if one-fifth of the sites are in coincidence, this is known as a  $\Sigma 5$  boundary [14]. A smaller  $\Sigma$  number is typically associated with special characteristics. As a consequence of this matching of the lattice points across the boundaries, coincidence site boundaries have lower energies than general boundaries. Rohrer [14] indicates that the energy anisotropy might have a strong link to the ideal crystal structure [14]. For Al and Cu at higher temperatures, there is agreement that minimum grain boundary energy occurs at the  $\Sigma 11$  boundary [14]; however, for Cu at low temperatures, this energy minimum moves closer to the  $\Sigma 9$  boundary [14]. This indicates that a temperature dependence of the grain boundary energy can exist, and this could be a contributing factor for AGG, where specific boundary energies can alternate as the lowest energy boundary.

In general, simulations confirm that for low-angle grain boundaries, the mobility rapidly drops [45]. To date, this has not been experimentally shown, but rather predicted. Through the experimental techniques utilized in this research, we have the capability to validate this type of

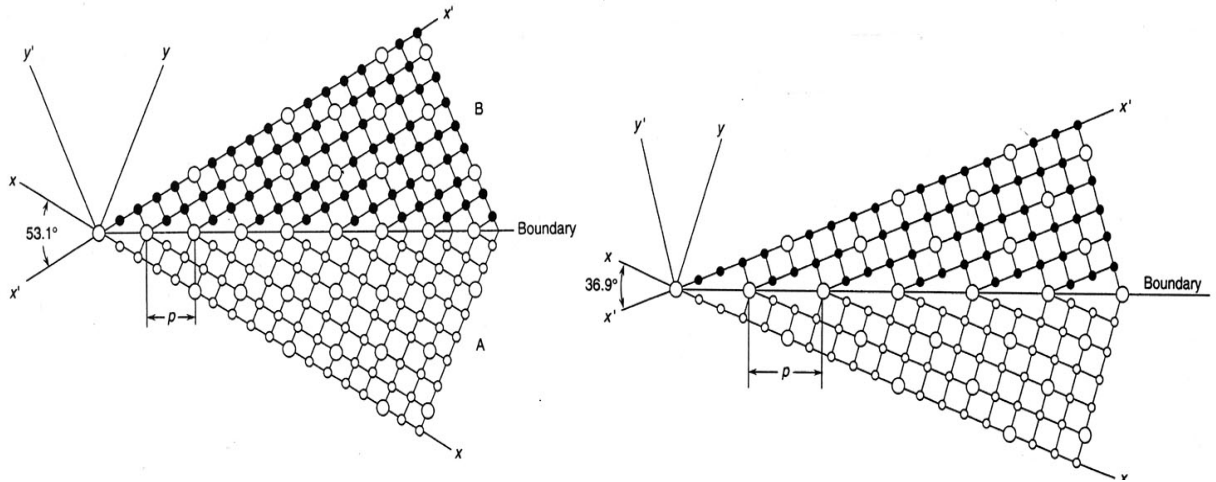


**Figure 1.1.** CSL configuration  $\Sigma 5$  in two different, symmetrical, rotations [45]

prediction. In addition, other CSL boundaries have been thoroughly simulated and modeled, but few experiments have provided validation to these predictions. For example, a  $\Sigma 5$  boundary has a lattice point agreement every fifth point, suggesting a reduced amount of 'free volume' in the boundary for atomic diffusion, it has been shown that it has high mobility relative to other boundaries [14]. The near- $\Sigma 7$   $40^\circ$  [14] boundary has also been reported to possess an anomalously high mobility [46]. This too was experimentally explored in this research by tracking individual grain boundary movement. By understanding the energetics and thermodynamics associated with specific grain boundaries, the governing mechanisms of grain growth could be investigated.

One characteristic of AGG is that it often appears to occur suddenly during annealing, as if there is an incubation time [47]. This could be related to variations in grain boundary energies and grain boundary mobilities with temperature, as is noted above. In Ni [13] and Ag [40], the incubation time for AGG was observed to decrease, and the density of abnormal grains was observed to increase, as the annealing temperature increased [47]. Yoon *et al.* [47] suggested that such temperature dependence was consistent with the step-growth mechanism, if the grain boundary roughening transition was taken into account. However, the evolution of the grain structure during the annealing treatments was not presented, and the dependence of AGG on the annealing temperature could not be fully characterized in real time [47]. Their conclusions were based on before-and-after observations as opposed to during the evolution.

To address this question of quantitative microstructure evolution during abnormal grain growth, a systematic study that measure and quantifies the number and type of boundaries as a function to annealing temperature is required. This was undertaken in this research. By

investigating the evolution of the grain boundaries *in situ*, this will provide information necessary to advance the fundamental understanding of grain growth phenomena.

## 1.6 Twin Boundary Motion

In addition to CSL boundaries, another set of boundaries known to exhibit special properties within a polycrystalline material is twin boundaries. Coherent twin boundaries,  $\Sigma 3$  {111}, are formed during the deposition process and are frequently observed in FCC metals that exhibit a low stacking fault energy (SFE), [48-51]. An array of Shockley partial dislocations, with equivalent Burgers vectors, can be used in order to represent the ends of these twin boundaries [52-56]. Because of the inherent nature associated with Shockley partial dislocations, the presence of twin boundaries in a polycrystalline structure produces a change in the crystallographic orientation between the matrix and the twinned crystal [57, 58]. Additionally, there is a discontinuity formed in the available slip systems, across the twin boundaries [59, 60]. This discontinuity means that a high resolved shear stress is required to transmit a single dislocation across a twin boundary – effectively strengthening the material [59-63].

Examples of this twin boundary-induced strengthening were presented by Lu *et al.* [6, 62, 63]. Their research showed that ultra-fine grained Cu with a high density of twin boundaries could achieve an uncommon combination of ultra-high strength and high ductility. Furthermore, Zhang *et al.* [1,2] reported that the inclusion of twin boundaries led to strengthening in austenitic stainless steel thin films by an order of magnitude, compared to their bulk counter part. In addition, they showed that a high tensile strength ( $\sim 1$  GPa) could be achieved in sputter-deposited nanotwinned Cu thin films. This high tensile strength was attributed to the fact that the slip systems in both the twinned and matrix crystals were symmetrical. This meant that both

sides of the twin boundary contained three conventional  $\{111\}$ -type glide planes which were not parallel to the twin boundary plane and contained three  $\{100\}$ -type glide planes that were not parallel to the twin boundary [48-51]. When the thin foils were subjected to a normal loaded (perpendicular to the twin boundary plane), the activity of the dislocations contained in the foil were the same, either on all  $\{111\}$ -type planes or on all  $\{100\}$ -type planes. Given the same number of slip systems and the same slip activity on the glide planes, plastic deformation can take place in symmetrical modes in both crystals within the twin boundary [59, 60].

Atomistic simulations have provided some insight into the interactions that occur between twin boundaries and the lattice glide dislocations, with respect to both the kinetics and the energetics of slip transmission across the coherent twin boundaries [52, 59, 64-66]. These studies supported the hypothesis that the interactions between lattice dislocations and twin boundaries could be a dominant factor in the strengthening process for metals containing twin boundaries [65]. Twin boundaries are nominally considered to be more resistant to migration, as compared to conventional grain boundaries, since their excess energies are an order of magnitude lower than that of other grain boundaries [67].

Although the twin boundaries are more resistant to migration than other grain boundaries, Chen *et al.* [68] explained that detwinning processes could occur, starting at 400 °C, along with the growth of grains. Dislocation arrays are often found at the migrating twin boundary front, and Chen *et al.* suggest that they are actively involved in the detwinning process. These dislocation arrays form not only at the ends of the receding twins, but also at the sites of dislocation walls that formed during processing. This allows twin boundaries to locally annihilate and convert into single dislocation lines, through detwinning mechanisms [68]. These mechanisms include the collective glide of partial dislocations at twin ends and the local

movement of dislocations. In the first case, detwinning occurs in a discontinuous step-wise process, while in the latter, twinned regions are converted back to the matrix orientation by dislocation movement [68].

The migration of the  $\Sigma 3 \{111\}$  coherent twin boundary, along its normal direction, is accomplished by the glide of twinning dislocations. These dislocations are characterized by Burgers vectors corresponding to Shockley partial dislocations, on the twin boundary plane [52]. These twinning dislocations are either nucleated from grain boundaries or can be formed as a result of a reaction between the lattice glide dislocations and the twin boundaries [59, 53-56]. A critical issue currently being disputed is whether or not these twin boundaries can be removed during deformation. To elucidate this behavior, *in situ* studies would be required, since *ex situ* studies may not reveal how detwinning occurs and which specific kinetic processes are involved during the annihilation of twin boundaries. Recently, Wang *et al.* [67] reported that the rapid migration behavior of incoherent twin boundaries in nanotwinned Cu films during *in situ* nanoindentation, which directly led to the motion of coherent twin boundaries.

When an incoherent twin boundary ( $\Sigma 3 \{112\}$ ) is subjected to a shear stress, Wang *et al.* [68] demonstrated that the net Peach-Koehler glide force is equal to zero, regardless of the magnitude of the applied shear stress. They used this theory to present an MD simulation of the room temperature migration of the incoherent twin boundaries [67]. Their developed model contained a  $\Sigma 3 \{112\}$  incoherent twin boundary with a thickness of 12 (111) planes and two  $\Sigma 3 \{111\}$  coherent twin boundaries, separated by the incoherent twin boundary [67]. This structure allowed for the net glide force acting on the incoherent twin boundary to be zero. They then subjected the modeled system to a constant shear strain of  $\epsilon_{yx} = 0.015$ , which corresponded to a shear stress of 0.45 GPa. What they found was that the emitted Shockley partial dislocations

move, and the incoherent twin boundary was able to migrate through the collective glide of those partials [67].

Wang *et al.* [67] also presented simulations, which suggested that detwinning could occur relatively easily for thin films [67]. The driving force for this detwinning was attributed to the interaction between two twin boundaries, arising from the variation in the energy of the twin boundaries. They also showed that shear stresses enable the incoherent twin boundaries to migrate with ease. They suggested that this is because the dissociation of the twinning dislocations, from the incoherent twin boundary, reduces the Peierls barrier to boundary motion [55, 67]. Additionally, Wang *et al.* [67] also suggested processes by which coherent twin boundaries can annihilate each other. When multiple twinning dislocations simultaneously nucleate at grain boundaries, the twinned crystal is reoriented into the matrix crystal, through collective glide [67].

### **1.7 Precession-Enhanced Diffraction Orientation Analysis**

In order to investigate the underpinnings of grain growth, the grain size, grain morphology, and grain-to-grain misorientation of each grain within a sample can be quantified using electron diffraction-based orientation mapping. Traditionally, orientation mapping has been performed with the use of electron-backscattered diffraction (EBSD) in the scanning electron microscope (SEM). The limitation of the spatial resolution in orientation imaging via EBSD, however, makes it difficult to investigate the microstructure of nanocrystalline metals. Several approaches towards orientation microscopy using diffraction methods in the TEM have been explored, and these include the automated analysis of convergent beam diffraction patterns, transmission Kikuchi patterns, and diffraction patterns reconstructed using dark field images

[69]. These methods, in principal, allow for a high spatial resolution in orientation mapping, but there are limitations that make these approaches unsuitable in many cases. The presence of strong dynamical effects, associated with the interaction between the emitted electron beam and a TEM foil, in electron diffraction is a limitation in many situations as the kinematical theory of electron diffraction is no longer applicable, leading to unreliable orientations. Improvements to the dynamical diffraction problem have been made by precessing the beam as it is scanned, in order to reduce the dynamical effects of the electron beam and by better sampling of spots in a higher-order Laue zone (HOLZ) [69]. This is the basis for the ASTAR system, manufactured by nanoMEGAS [70].

The ASTAR system allows for the possibility of reliable orientation/phase mapping with a spatial resolution down to 3 nm, within the TEM [70]. Precession enhanced electron diffraction (PED) was first introduced by Vincent and Midgley [71]. In PED, the incident electron beam is double-deflected in a conical manner such that the diffraction intensities can be integrated over the entire scan, as is presented in Figure 2. As the incident beam undergoes this precession, the diffraction pattern moves and quasi-kinematical diffraction conditions can be achieved. This is because the dynamical effects of the electron beam are reduced since the incident electron beam is no longer on-axis and fewer beams are excited simultaneously. The use of precession also allows for the collection of a higher number of reflections, including reflections from HOLZs, which is useful in improving the reliability in the orientation matching of an electron diffraction pattern [70]. Within the ASTAR platform, spot diffraction patterns are captured sequentially by the use of a high-speed optical CCD camera while an area on the sample is being scanned by a nano-sized quasi parallel probe [70]. Simultaneously, the incident electron beam is precessed about the optic axis, and the CCD camera captures the diffraction

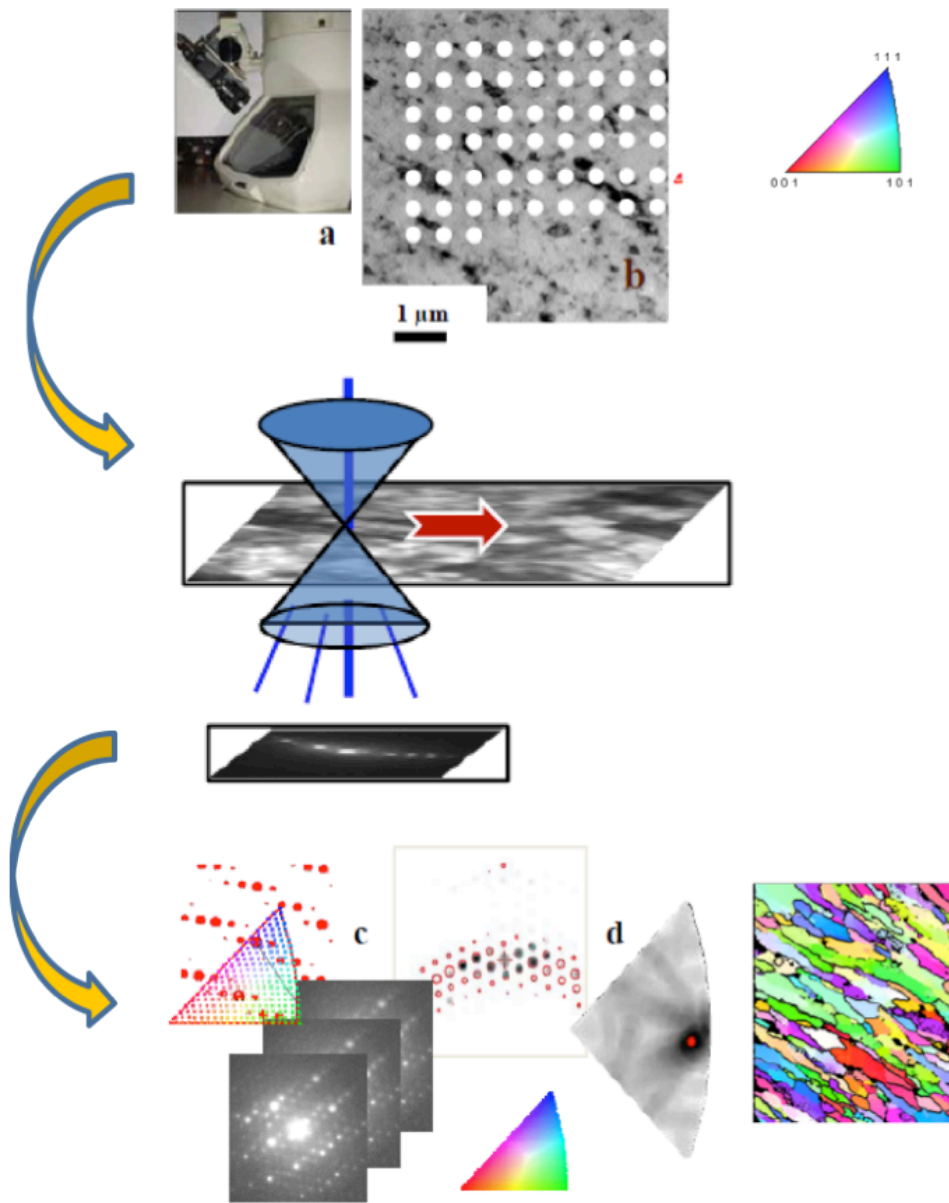


**Figure 1.2.** A graphical representation of the precession enhanced diffraction orientation procedure. (a) the sample is aligned in the TEM (b) a grid is defined over a region of interest (c) the beam is precessed and the acquired diffraction patterns are saved as a block file (d) the acquired diffraction patterns are compared to a bank of all possible patterns, and an orientation map is generated [70]

patterns that are projected onto the fluorescent screen at a rate of up to 180 frames per second [50]. As the beam is scanned over a pre-selected region of interest, an electron diffraction pattern from each step in the scan is recorded and stored.

Next, using the basic theory of kinematical diffraction, diffraction spot patterns, corresponding to all of the possible orientations within a specific crystallographic space group, are calculated and stored as a bank of possible patterns. Every experimentally collected diffraction pattern is compared to this template bank, and the degree to which a pre-calculated pattern matches the experimental pattern is represented by the correlation index (the highest correlation index indicates the best fit for matching). Finally, the ASTAR system allows the user to generate a virtual bright-field image, a correlation index map, and a reliability map, corresponding to the orientation map produced from the PED scan [72].

Since the orientation of a specific pattern is determined through the correlation index, there are situations where the highest correlation index value is not representative of the correct orientation, although it is identified as the “best fit” for the pattern. This can arise due to an electron diffraction pattern with poor contrast or from an ambiguous electron diffraction pattern. In order to improve the fidelity of the orientation maps, there are corrections applied using the TSL OIM 5 software platform. The two corrections that are utilized in this research were the ‘Grain Dilation’ and the ‘Neighbor Confidence Interval Correlation’ [73]. The ‘Grain Dilation’ function works as a clean-up method by using an iterative process that acts only on points that do not belong to any grains but have neighboring points which belong to grains. A point may be considered to not belong to a specific grain if it belongs to a grain group having fewer members than the minimum allowed grain size. If the majority of the neighbors belong to the same grain, then the orientation of the unmatched point is changed that that of the majority grain [73]. Next,

the ‘Neighbor Confidence Interval Correlation’ was performed on data points with a correlation index less than a defined confidence value. For the research presented in this dissertation, the confidence interval used was 95%. If a particular point has a correlation index less than this minimum value, then the neighbors are checked to see which has the highest correlation index. The orientation and the correlation index of the poorly matched point is reassigned to match the orientation of the neighboring point [73]. These two corrections were found to increase the matching in the orientation maps without aggressively changing the collected data.

## CHAPTER 2

### A COMPARISON OF GRAIN BOUNDARY EVOLUTION

Copyright © 2013 Acta Materialia Inc. Published by Elsevier Ltd.

#### A Comparison of Grain Boundary Evolution during Grain Growth in FCC Metals

J.G. Brons<sup>1</sup> and G.B. Thompson<sup>1</sup>

<sup>1</sup>The University of Alabama, Metallurgical Engineering Department, Tuscaloosa, AL

Keywords: Grain Growth, Precession Electron Diffraction, Orientation Microscopy, Coincidence Lattice, Nanocrystalline Thin Films, Abnormal Grain Growth

#### 2.1 Abstract

Grain growth of Cu and Ni thin films, subjected to *in situ* annealing within a transmission electron microscope, has been quantified using a precession-enhanced electron diffraction technique. The orientation of each grain and its misorientation, with respect to its neighboring grains, were calculated. The Cu underwent grain growth that maintained a monomodal grain size distribution, with its low angle grain boundaries being consumed, and the Ni exhibited grain growth in stages from normal-to-abnormal-to-‘normal’. The onset of Ni’s abnormal grain growth was accompanied by a sharp increase in the  $\Sigma 3$  and  $\Sigma 9$  boundary fractions, which is attributed to simulation predictions of their increased mobility. These  $\Sigma 3$  and  $\Sigma 9$  fractions then dropped to

their room temperature values during the third stage of grain growth. In addition to the  $\Sigma 3$  and  $\Sigma 9$  boundaries, the  $\Sigma 5$  and  $\Sigma 7$  boundaries also underwent an increase in total boundary fraction with increasing temperature in both metals.

## 2.2 Introduction

The strength, toughness, corrosion resistance, electrical properties, and optical properties of nanocrystalline materials are frequently grain size dependent [1-3]. For example, the bulk properties of polycrystalline materials can be significantly improved by controlling the grain size, the grain boundary character distribution, and the grain boundary connectivity [4]. The stability of these properties is of concern, since these fine grain sizes are associated with an inherently high driving force to coarsen [1, 2, 5]. Extending the processing and application of these fine grain materials requires validation of modeling predictions. Elucidating microstructural evolution is currently one of the central tasks of materials science [3, 5, 6].

Examples of microstructural instability in nanocrystalline metals include abnormal grain growth at low temperatures [7] as well as abnormal grain growth under cyclic loads [8]. Since grain boundary properties, such as energy and mobility, play a key role in determining the growth of grains, there has been a long-standing interest in these topics. Recent microstructural modeling that explicitly includes the variation of boundary properties with boundary type [9-13] has drawn even more interest to the topic. These studies utilize simple models for the variation in boundary properties with macroscopic boundary geometry, and they would benefit greatly from a more complete description of the property variations.

The conventional concept of grain growth, derived from coarse-grained polycrystalline studies [14] is that the process is driven by the reduction of the total grain boundary area in the material. The underlying mechanism involves curvature-driven grain boundary migration, where the motion of the grain boundaries is towards the center of their curvature [6, 11]. Normal grain growth occurs continuously, with grain boundary migration distributed uniformly over the interfacial network. This allows the grain size distribution to undergo self-similar growth behavior [15-17]. Normal grain growth occurs when there are no opposing energies to curvature driven growth. This description leads to a simple relationship between the grain boundary migration velocity,  $V$ , the interface mobility,  $M$ , and the driving force,  $P(V)$  [6]. Alternatively, abnormal grain growth may occur when the coarsening of some grains is suppressed or augmented by a variety of effects, such as grain boundary grooving, precipitate drag, significant distribution of grain boundary energies, and substrate interactions [15-17]. This causes the growth of a specific orientation to be favored, typically a low-energy, high-symmetry plane.

The microstructural instabilities of nanocrystalline metals have been observed through grain growth, including abnormal grain growth, at temperatures below 600 K in Au [18-20], Cu [19], Pd [21], and Ni [22]. Previous observations of abnormal grain growth have been attributed to the initial microstructure, including the distribution of grain sizes, misorientations, grain boundary energies and mobilities, triple junction mobilities, impurities, microstrains, and topological features such as curvature and the number of boundary faces [23, 24]. In addition, for films, the formation of grooves at grain boundaries has been noted to occur, and to contribute to the stagnation of grain growth. This was noted as early as 1956 by Mullins, who also noted that a grain with a low surface energy must avoid trapping of its boundaries by groove formation, leading to abnormal grain growth. This idea has since been elaborated on in the thin film grain

growth field and extended to include grains favored by strain energy minimization. To date, there has been considerable theoretical attention on abnormal grain growth [25, 26]. Most models propose that the initial grain size distribution is not uniform, but contains at least one large grain [27]. The models analyze possible growth mechanisms based on this large grain. Recently, Rios [24, 28] found that abnormal grain growth can occur, even when a uniform grain size distribution is present if grain growth is restricted by a pinning force.

While there is some understanding of how boundary properties vary, the variation of boundary properties has not yet been fully elucidated [29, 30]. A number of experimental and theoretical studies in the past decade have shown that polycrystalline materials develop an anisotropic grain boundary character distribution (GBCD) during grain growth [31, 32]. Results from experiment and simulation suggest there is an inverse relationship between the relative energy of a grain boundary and its total area in the polycrystal. While it is not possible to measure the frequency with which boundaries are eliminated, it is possible to determine which grain boundaries are shrinking and which are growing. Holm *et al.* [32] found, through atomistic modeling, that the boundary structure is the dominant influence on boundary energy for materials with the same crystal structure. For some boundaries, they observed a large number of configurations that minimize to approximately the same low-energy value [32]. Low-energy boundaries, such as low coincidence site lattice (CSL) boundaries, are more likely to grow [31].

Theoretical models for the misorientation distribution function predict that the population of special grain boundaries in polycrystals ranges from 20 to 60% [33]. Such a large fraction of special boundaries is rationalized by the annealing textures and existence of local clusters of special boundaries as discussed by Ralph and Randle [34]. Despite the numerous computational and experimental studies referenced above, very little of the actual grain boundary migration is

understood. In large part, this is because of difficulty in observing grain boundary migration. Typically, migration is inferred by characterizing the change in microstructure after annealing treatments. This study implements a step-wise annealing schedule so the motion of individual grain boundaries can be tracked as the grain boundaries evolved during annealing. This allows the tracking of not only the grain size, but also the evolution of specific boundary types and the overall texture of the film as it responds to the increase in temperature.

Previous experimental studies [35, 36] on grain boundary character distributions in low stacking fault energy (SFE) face-centered cubic (FCC) materials found that the distribution of coincidence site lattice (CSL) boundaries show a strong prevalence of  $\Sigma 3^n$  (where  $n = 1, 2, 3$ ) boundaries. As for FCC metals, there have been several computational studies [37, 38] investigating the structure and energy of grain boundaries. The evolution of the CSL boundary distributions has been found to be influenced by the processing conditions [39] and has been discussed in terms of the relative contributions of both the kinetic and geometric influences [40]. The main objective of this study is to experimentally assess the relative proportions of low- $\Sigma$  CSL boundaries in FCC metals to elucidate the role of special boundaries in microstructural evolution.

The designed study is unique in that we are able to determine the specific orientation of each grain, as well as the misorientation across each grain boundary. To date, the nanoscale size regime of grain growth has not been systematically studied because of the limitations of scanning electron microscopy (SEM) electron backscatter diffraction (EBSD) techniques when quantifying  $<50$  nm grains. This is because the spatial resolution of traditional EBSD scans is governed by the SEM electron optics. This work uses precession-enhanced diffraction orientation analysis for the transmission electron microscope (TEM) to generate pseudo-

kinematic electron diffraction conditions, allowing grain orientations to be captured to sizes approaching 5 nm. This allows the program to probe a length scale an order of magnitude smaller to elucidate how grain type (special boundaries, twins, or high angle boundaries) in nanocrystalline Cu and Ni contributes and evolves during grain growth.

Nanocrystalline thin films are optimal to investigate these outstanding questions because of their high grain boundary curvature and they possess a high surface area-to-volume ratio. Normal grain growth usually ceases when the grain size becomes comparable to the smallest specimen dimension, in this case the thickness of the thin film [11]. Because of this, the grain boundary energies will dominate the growth mechanisms since some grains will grow quickly to reach a diameter that is much larger than the film thickness. Hence, the majority of the grain growth will be two-dimensional [41].

### **2.3 Experimental**

Nanocrystalline Cu and Ni films were sputter deposited in an AJA ATC-1500 stainless steel magnetron-sputtering system with an approximate thickness of 45 nm onto 100 nm thick DuraSiN<sup>TM</sup> substrates. These two materials were chosen because of the similarities in their crystal structures, lattice parameters, melting temperatures, and stacking fault energies, as tabulated in Table 1. This allows for comparison of grain growth behavior independent of such material dependent variations. The deposited film thickness was selected because it allowed the films to be electron transparent without any further preparation methods. Fiducial markers were then focused ion beam (FIB) milled into the films using an FEI Quanta dual-beam FIB, so that any thermal drift could be corrected within the TEM. This ensured the same 4 x 4  $\mu\text{m}$  region of interest (ROI) was captured at each temperature step, by resetting the stage to the correct

**Table 2.1.** Selected material properties for metals studied [56, 57]

<b>Material</b>	<b>Crystal structure</b>	<b>T<sub>m</sub> (°C)</b>	<b>SFE (mJ/m<sup>2</sup>)</b>
Cu	FCC	1084	70-78
Ni	FCC	1455	90

location. Since the desired ROI was  $4 \times 4 \mu\text{m}$ , the fiducial markers were placed at  $20 \times 20 \mu\text{m}$  as to make certain that no edge effects from the markers were present near the grains of interest. The temperature schedule, determined from previous experimentation, was ambient ( $30 \text{ }^\circ\text{C}$ ),  $250 \text{ }^\circ\text{C}$ ,  $400 \text{ }^\circ\text{C}$ ,  $450 \text{ }^\circ\text{C}$ ,  $500 \text{ }^\circ\text{C}$ ,  $550 \text{ }^\circ\text{C}$ , and  $600 \text{ }^\circ\text{C}$ . Significant grain growth initiated at  $400^\circ\text{C}$  such that lower temperature scans were not required.

To achieve these temperatures an *in situ* Gatan 652 double-tilt heating holder was utilized within an FEI Tecnai F20 Supertwin TEM operated at  $200 \text{ keV}$ . As described by Hattar *et al.* [42], the temperature of the Gatan heating stages are accurate to within a few degrees, but there is some uncertainty about the actual temperature of the area being examined since it is not in intimate contact with the heating element. In order to perform the precession-enhanced electron diffraction, the NanoMEGAS ASTAR platform was used. The details of how the nanoMEGAS platform produces an orientation map can be found in reference [19]. The precession-enhanced diffraction-based orientation analysis was utilized with a  $1^\circ$  angle of precession with a scanning step size of  $10 \text{ nm}$ . As described by Hau-Riege and Thompson [43], the electron beam was averted from the sample at the end of the scan by closing the column valve, which minimized the beam effects on possible crystallographic transformations. In order to avoid thermally-induced drifting during the orientation mapping, the films were heated to and held at the desired temperature for 40 minutes to allow for grain growth, then cooled back to ambient temperature by turning off the heating source and allowing the stage to equilibrate. This nominally took about 30-45 minutes, depending on the peak temperature. In previous research [44], grain growth appeared to be complete after about 15 minutes of annealing, so the selected annealing time of 40 minutes is considered to be a sufficient amount of time to allow for grain growth.

After the orientation scans were collected, the data was converted for analysis using TSL OIM Analysis 5 software. The data was optimized using the Grain Dilation and Neighbor CI Correlation corrections. After optimization, the orientation of each of the grains, the misorientation distribution, and the CSL boundary fraction using Brandon's criterion [45] were calculated.

## 2.4 Results

Figures 1 and 2 are the orientation maps collected at each of the seven annealing temperatures outlined above (30, 250, 400, 450, 500, 550, and 600 °C) for Cu and Ni respectively. Each map shows the same ROI allowing individual grains to be tracked. At 30°C, the film consisted of equiaxed nanocrystalline grains with a primarily  $\{101\}$  orientation, as seen in Figure 1(a) and 2(a). As the annealing temperature increased, the grain size was found to increase, Figures 1(b)-(g) and 2(b)-(g), and the orientation of the individual grains shifted.

The orientation maps of the *in situ* Ni annealing experiment are presented in Figure 2. Starting at 250°C (Figure 2b), it is seen that a few grains, with a common near  $\{001\}$  orientation, start to grow much larger than the surrounding matrix grains. At 400 (Figure 2c) and 450°C (Figure 2d), these larger grains continue to grow much larger than the surrounding grains, although they also begin to grow. At the higher temperatures, 500 (Figure 2e), 550 (Figure 2f), and 600°C (Figure 2g), the boundaries of the large grains transition from faceted edges to rough and irregular edges.

To qualitatively view the texture evolution of the Cu and Ni films, the area fraction of  $\{001\}$ ,  $\{101\}$ , and  $\{111\}$  grains are plotted as a function of homologous temperature ( $T/T_m$ ) in Figures 3(a)–(c), respectively. After sputter-deposition, both the Cu and the Ni consisted almost

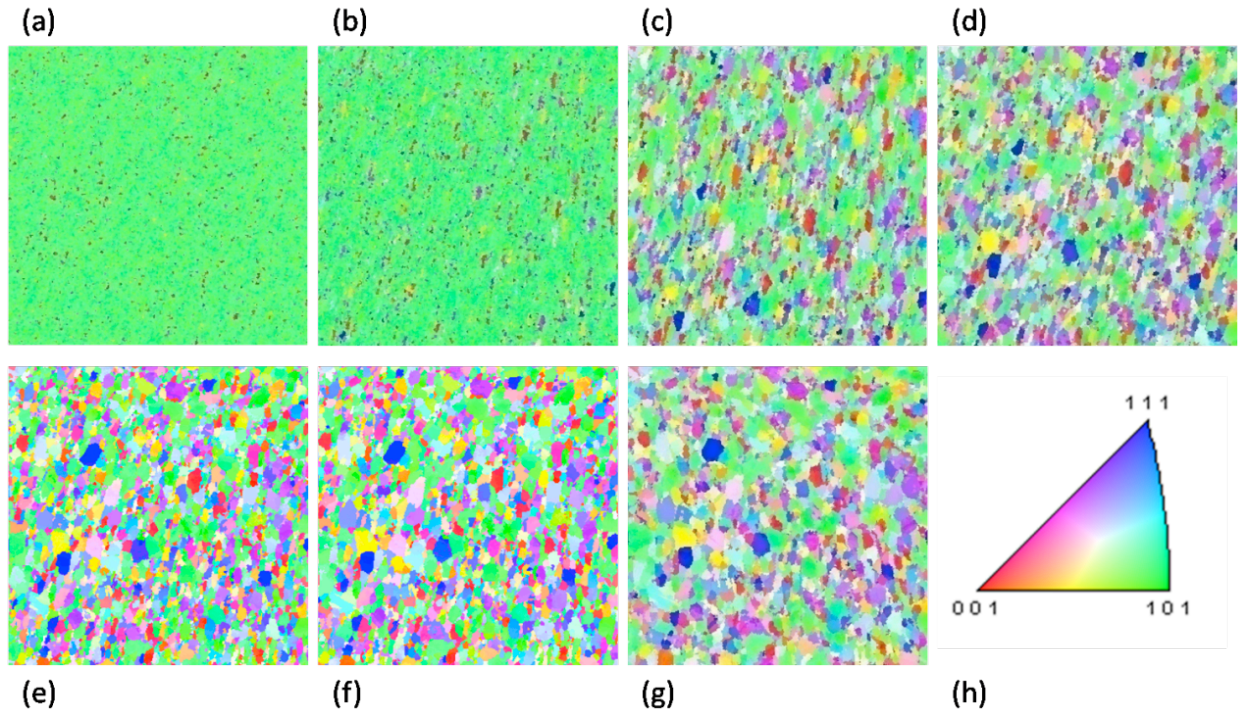


**Figure 2.1.** Evolution of Cu microstructure during annealing a) 30 °C b) 250 °C c) 400 °C d) 450 °C e) 500 °C f) 550 °C g) 600 °C h) Inverse Pole Figure. Each box is 4 $\mu$ m x 4 $\mu$ m.

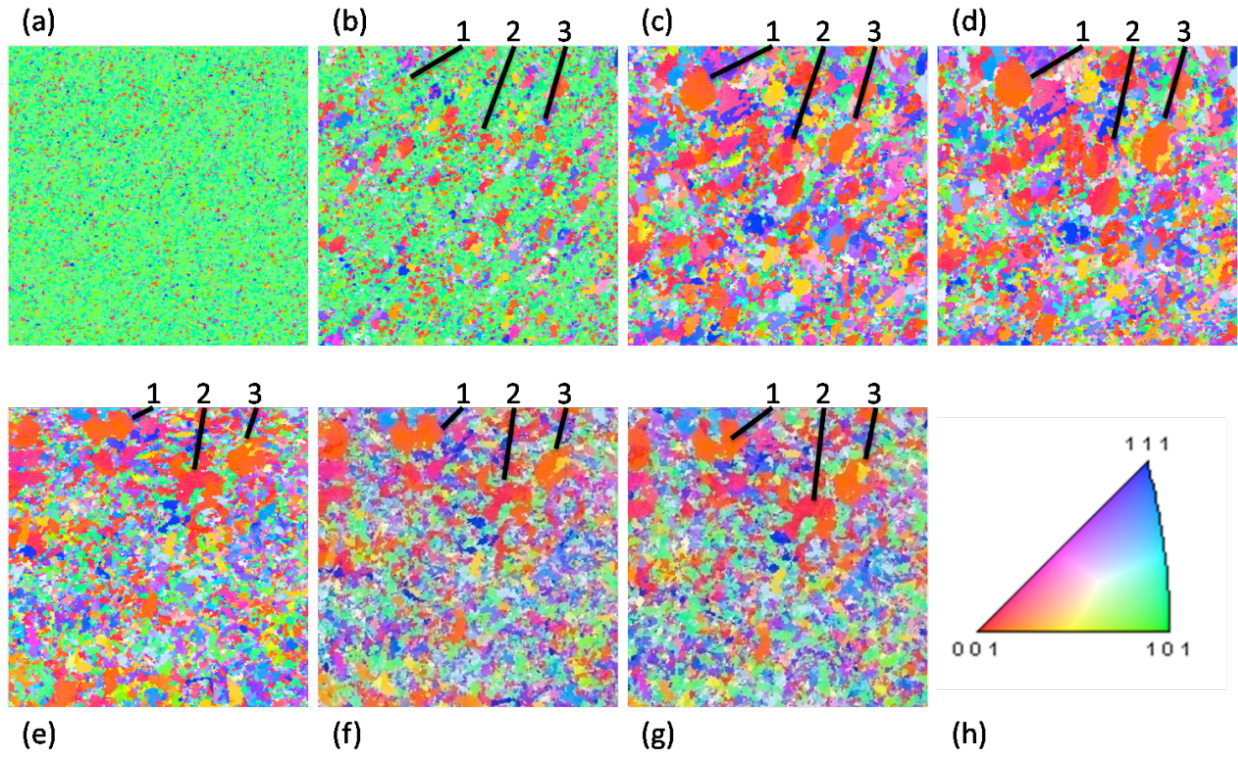


**Figure 2.2.** Evolution of Ni microstructure during annealing (a) 30 °C b) 250 °C c) 400 °C d) 450 °C e) 500 °C f) 550 °C g) 600 °C h) Inverse Pole Figure. Each box is 4μm x 4μm.

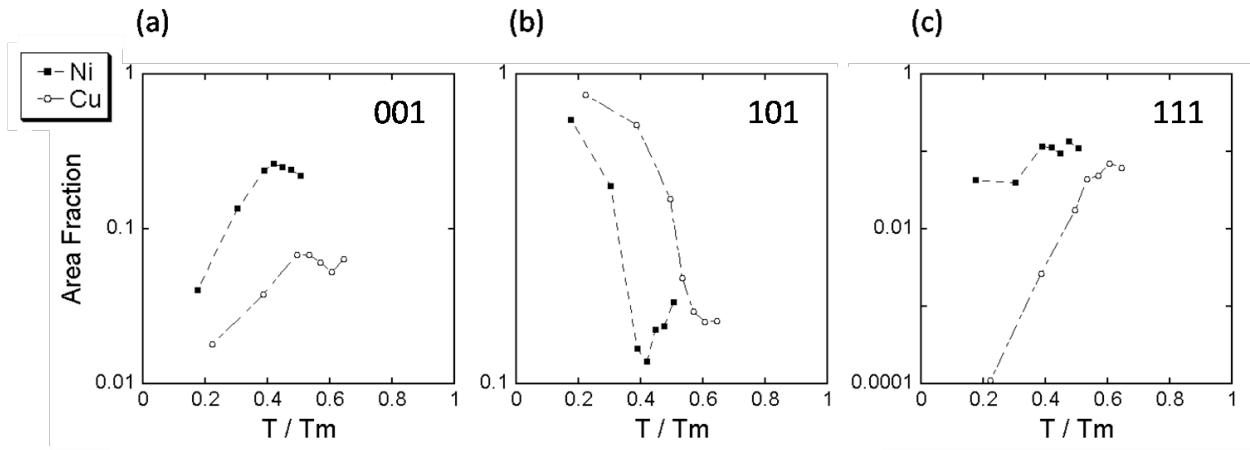


**Figure 2.3.** Texture evolution with temperature for the (a) {001} (b) {101} and (c) {111} orientations

entirely of grains with a  $\{101\}$  orientation. The Cu film exhibited a steady drop in the area fraction of  $\{101\}$  grains as grain growth progressed. At a homologous temperature of about 0.6, it had reached a minimum and remained steady for the remainder of the experiment. The area fraction of the  $\{111\}$  grains in the Cu grew sharply during the annealing, with most of the growth occurring before a homologous temperature of 0.5. The  $\{001\}$  grains also underwent growth during the initial stages, with the area fraction remaining relatively constant after a homologous temperature of about 0.5.

As the Ni film was annealed, there was a measured drop in the area fraction of the  $\{101\}$  grains. It was a sharp drop up to a homologous temperature of about 0.4, Figure 3(b). Then, the area fraction of  $\{101\}$  grains slowly began to rise throughout the rest of the annealing temperatures. While the  $\{101\}$  grains were consumed, there was an increase in the area fraction of the  $\{001\}$  grains, Figure 3(a), up until a homologous temperature of 0.4. After this point, the area fraction of the  $\{001\}$  grains remained relatively constant. The same type of growth was observed in the  $\{111\}$  grains, Figure 3(c), with the expansion in area fraction occurring initially with relatively no texture evolution occurring after a homologous temperature of about 0.4.

Quantitatively, this evolution of grain sizes in Cu and Ni, as a function of annealing temperature, is plotted on the graphs presented in Figure 4(a)-(b), respectively. It can be seen in Cu that initially there is a narrow distribution of grain sizes, indicative of the steep slope on the cumulative area fraction plot of Figure 4(a). As the annealing temperature reached 400°C, and higher, the curves became less steep, although the formation of ‘ledges’ in the curve is never observed.

In contrast, the Ni cumulative area fraction plot, Figure 4(b), shows some dramatic differences compared to Cu’s plot in Figure 4(a). It can be seen that after annealing at 250°C, the

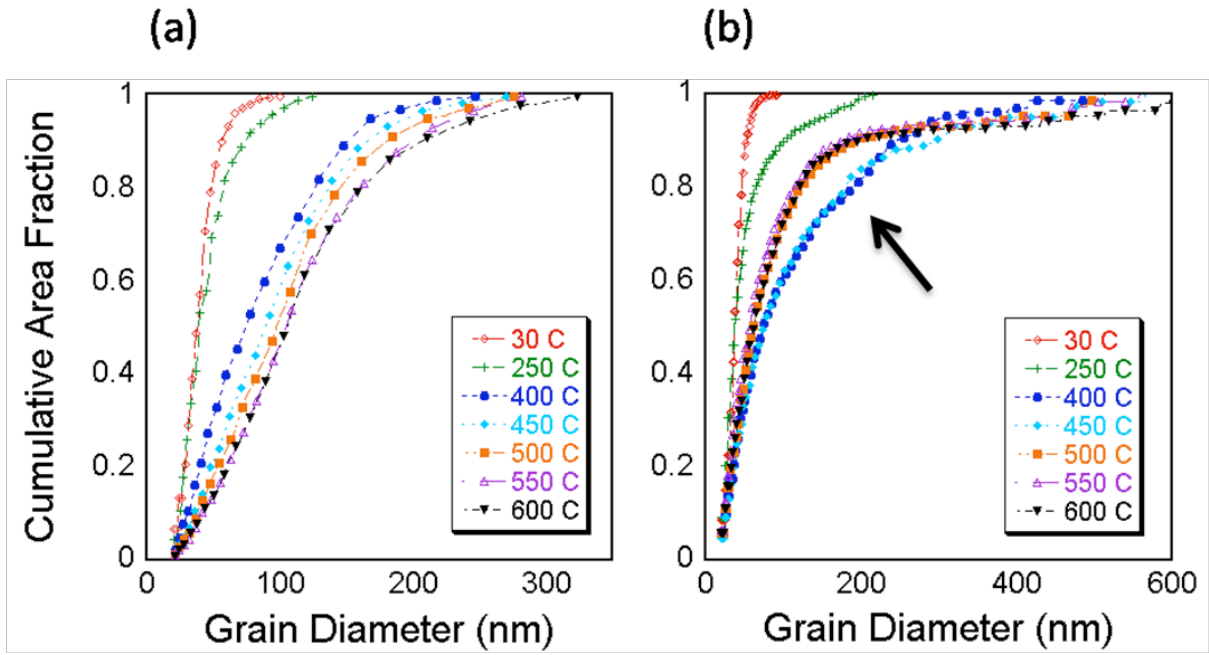


**Figure 2.4.** Cumulative area fractions for different grain sizes as a function of temperature for (a) Cu and (b) Ni

curvature of the cumulative area plot deviates from that of the initial grain size distribution. Next, the distribution of grain sizes between 400 and 450°C continues to change evident by the modulated slope, indicated by the arrow in Figure 4(b). This modulation at these two temperature steps is indicative of abnormal grain growth. After the 500, 550, and 600°C annealing steps, the grain size distribution is once again monomodal, indicative of a different mode of grain growth behavior, evident by the continuous nature of these curves with no abrupt slope modulations.

Since Cu and Ni have similar intrinsic material properties, Table 1, the observed difference in grain growth behavior must be linked to another material property. To provide quantitative understanding of this phenomenon, the characteristic nature of the grain boundary evolution is tracked. The character of the grain boundaries was determined by their misorientation across each grain. By applying Brandon's criterion [45], these misorientations were analyzed to determine the presence of CSL boundaries, since they have been reported to have special properties [12, 13, 17, 18, 32].

The dependence of the CSL boundary evolution on the homologous temperature is plotted in Figure 5. Figure 5(a) presents the evolution of the low angle boundaries ( $< 15^\circ$ ) during the annealing experiments. The Cu, which exhibited only grain growth with no abrupt shape modulations in the cumulative grain size distribution plot, exhibits a drop in the low angle boundary ( $\Sigma 1$ ) fraction at 400°C or a homologous temperature of about 0.5. Interestingly, the Ni film does not show any decrease in the low angle boundary fraction. This may be contributed to the peak annealing temperature being 600°C. Temperatures in excess of this value resulted in delamination of the film.

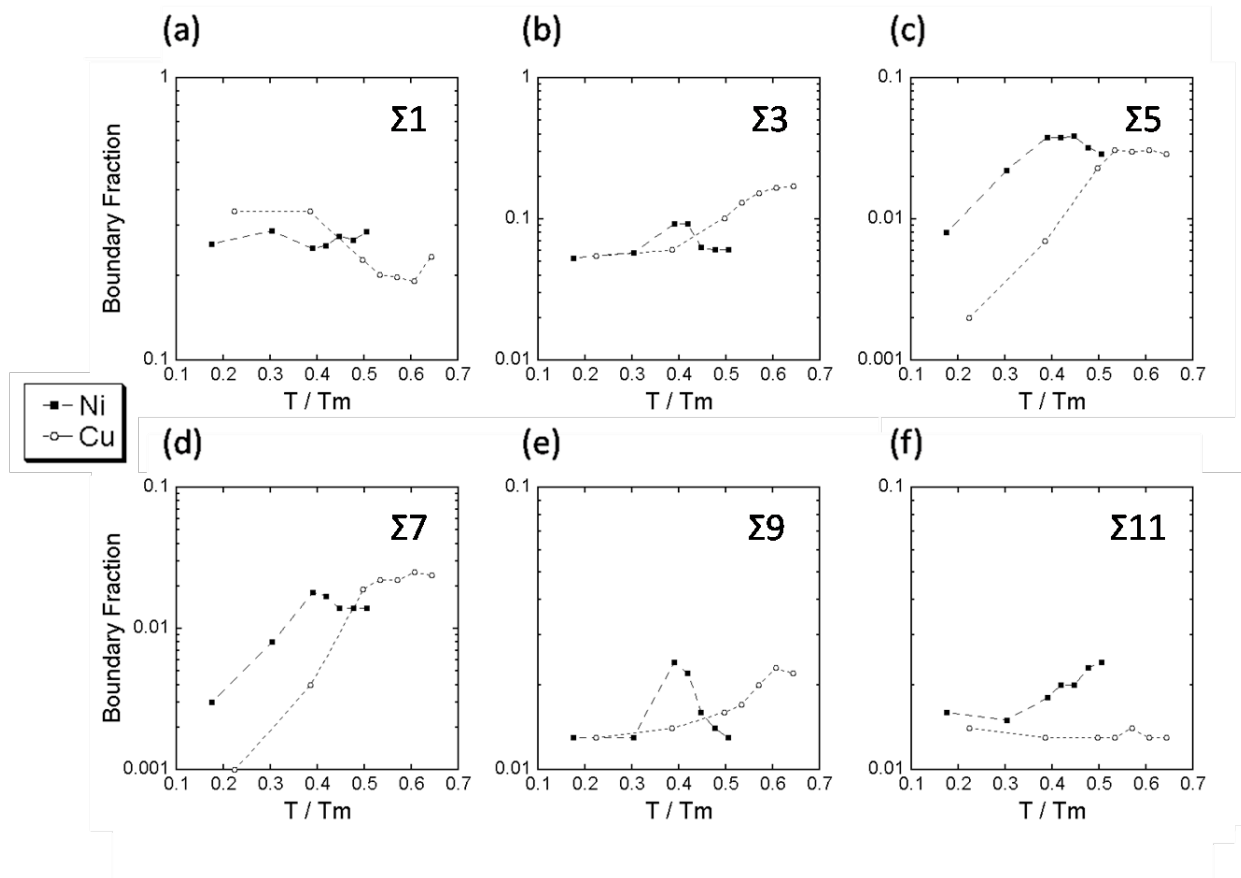


**Figure 2.5.** Coincidence site lattice boundaries as a function of the homologous temperature a)  $\Sigma 1$  b)  $\Sigma 3$  c)  $\Sigma 5$  d)  $\Sigma 7$  e)  $\Sigma 9$  f)  $\Sigma 11$

During the grain growth in Cu, there was a continual increase in  $\Sigma 3$  boundary fraction, Figure 5(b). For the abnormal grain growth behavior observed in Ni, there is a measured increase in the  $\Sigma 3$  boundary fraction only at the temperatures where a bimodal grain size distribution was present, Figure 4(b). This was at a homologous temperature of about 0.4.

Both the  $\Sigma 5$  and  $\Sigma 7$  boundaries, Figures 5(c)-(d), seem to scale together as the annealing progressed. For the Cu, both CSLs increase sharply up to a homologous temperature of about 0.4, at which point, they remain relatively constant. In the Ni film, the  $\Sigma 5$  and  $\Sigma 7$  boundary fractions increased from the ambient temperature state to a maximum value at a homologous temperature of about 0.3. They then stayed at their maximum boundary fraction while abnormal grain growth occurred and begin to slowly decrease after a monomodal grain size distribution, Figure 4(b), was once again present.

The  $\Sigma 9$  boundary fraction evolution with temperature, shown in Figure 5(e), shows a marked difference between Cu and Ni. Cu exhibited a  $\Sigma 9$  boundary fraction evolution that showed a slow-onset increase as the grain size evolved where as Ni showed a spike at the onset of abnormal grain growth. After Ni's abnormal grain growth completed, and a monomodal grain size distribution was once again observed, the  $\Sigma 9$  boundary fraction returned to its original, ambient temperature value.

The Cu exhibits a relatively constant  $\Sigma 11$  boundary fraction, Figure 5(f), over all of the temperature steps. In the Ni film, there is an increase in  $\Sigma 11$  boundary fraction at a homologous temperature of 0.4, which is the onset of abnormal grain growth. When the Ni grain size distribution returned to a monomodal state, at a homologous temperature of about 0.5, the  $\Sigma 11$  boundary fraction still continued to increase. This differs from Ni's  $\Sigma 3$ ,  $\Sigma 5$ ,  $\Sigma 7$ , and  $\Sigma 9$

observations which all underwent a reduction after the system returned to a state with a monomodal grain size distribution.

## 2.5 Discussion

The results of the CSL evolutions in the Cu film are in agreement with results seen in the simulations performed by Janssens *et al.* [46]. They predicted that the mobility of low-angle grain boundaries ( $\Sigma 1$ ) rapidly drops. Holm *et al.* [47] also explained that there is no mechanism to preserve low energy boundaries at the expense of high-angle boundaries. In this study, the low angle grain boundary fraction for Cu decreased as the higher-angle CSL boundaries experienced a growth in boundary fraction. Additionally, Janssens *et al.* [46] presented that the near- $\Sigma 7$   $40^\circ$  boundary has an anomalously high mobility and that grain boundaries with the  $\Sigma 3$  type misorientation also possess a very high mobility [47]. Among the  $\Sigma 3$  boundaries identified in the Cu film, many are thermal twins created during annealing. These twin boundaries allowed for a mode of grain growth, which maintained a monomodal grain size distribution because of their high mobility and relatively low boundary energies [23, 25, 48]. The twin boundaries are identified by the red boundaries (primary recrystallization twins) and blue boundaries (secondary recrystallization twins) within the ROI at 400, 500, and 600°C in Figures 6(a)-(c), respectively.

In polycrystals with many  $\Sigma 3$  boundaries, there is a tendency for  $\Sigma 3$  boundaries to form  $\Sigma 3$ - $\Sigma 3$ - $\Sigma 9$  triple junctions [49], so it is reasonable to expect that the  $\Sigma 9$  boundary fraction would scale with the  $\Sigma 3$  boundary fraction, as observed in these experiments. The  $\Sigma 3$  and  $\Sigma 7$  boundaries in Cu experienced the most growth during the grain boundary evolution which supports previous simulations that these CSLs have high mobilities [31, 32, 48, 49].

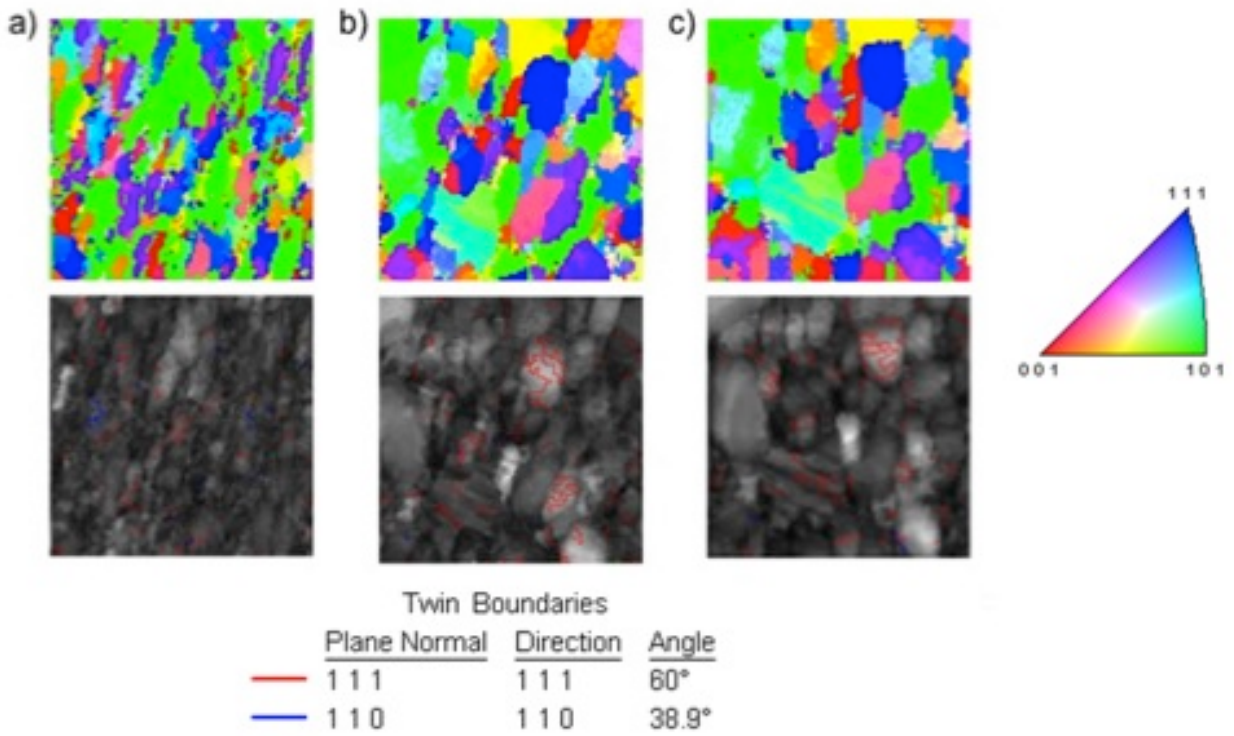


**Figure 2.6.** Twin boundary evolution in Cu at a) 400 b) 500 and c) 600. The top images are orientation maps and the bottom images are image quality maps with the primary twin boundary (red) and secondary twin boundary (blue) outlined. Each box is  $1\mu\text{m} \times 1\mu\text{m}$

It had been reported [2,50] that nanocrystalline Ni undergoes a multi-staged sequence of abnormal-to-normal-to-abnormal grain growth during isothermal annealing. In similar studies [45,51] Ni's microstructure developed in an erratic manner, characteristic of abnormal grain growth. These types of observations were confirmed in this study. As shown in the orientation maps in Figure 2, as well as the grain size distribution plot in Figure 4(b), abnormal grain growth was evident after the 400°C anneal. There were a few grains that grew to a size much larger than the surrounding matrix grains. Most of these grains were oriented in the  $\{100\}$  direction. Three of these grains are labeled 1, 2, and 3 within Figure 2. This abnormal grain growth continued through the 450°C anneal, where these  $\{100\}$  grains continued to grow much larger than the matrix nanograins around them. After 500°C, these large grains evolved in a different manner, where the grain size distribution was observed to be monomodal, observed in the cumulative grain size plot in Figure 4(b). At 550 and 600°C, this new stage of grain growth continued dominate. The Ni underwent a normal-to-abnormal-to-‘normal’ growth pattern suggesting that abnormal growth is not a continuous event. During the third stage of grain growth, the boundaries of the large grains, including grains 1, 2, and 3, became curved in a ‘horse-shoe shape’ and de-faceted.

Zhang *et al.* [52] reported that in  $\{100\}$  and  $\{111\}$  orientations the in-plane stresses were approximately equal for FCC symmetries, which is not the case for other orientations [52]. Additionally, the  $\{100\}$  oriented grains have the lowest strain energy [52]. Consequently, the abnormal growth of  $\{100\}$  oriented grains, and the change in texture from  $\{101\}$  to  $\{100\}$  after annealing, may be driven for the minimization of strain energy [52]. This orientation change is much more drastic in the Ni film compared to the Cu film, Figure 3(a). The most substantial texture change observed in the Cu can be seen in the  $\{111\}$ , Figure 3(c). Initially, the area

fraction of grains exhibiting a  $\{111\}$  orientation was almost non-existent, and this fraction increased almost three orders of magnitude. This is likely due to a significant contribution of surface energy minimization on the driving force for the grains to grow. Since abnormal grain growth can occur in specimens without sharp crystallographic textures, the bulk texture cannot solely drive the onset of abnormal grain growth.

As was previously reported for Ni [36], grain boundaries in large columnar grains became curved at numerous locations. A coalescence-type mechanism may be responsible for the initiation of abnormal grain growth in nanocrystalline Ni [53]. It is conceivable that a rotation mechanism could dominate during the initiation of abnormal grain growth, while a migration mechanism dominates once a large enough size advantage is achieved for the abnormally growing grains [45]. Uniform grain boundary energies would lead to grain boundary curvature as the driving force for grain growth, which would result in uniform expansion along all portions of the grain boundary [54]. Variations in grain boundary energy can account for the irregular shaped morphology of grains as well as the tendency for growth to sometimes progress from one location, stop, and begin at a different location [54]. When variability of grain boundary energy is factored in, the growth follows a more irregular path as the best means to minimize the total energy in the system [54].

To further quantify these different grain growth behaviors, the evolution of the CSL boundaries provides some insight. During Cu's grain growth, the grain size starts to evolve at 400 °C, and there is a decrease in the low angle boundary fraction at that point, Figure 5(a). Simultaneously, there is a sharp increase in the fraction of  $\Sigma 3$ ,  $\Sigma 5$ , and  $\Sigma 7$  boundaries, Figures 5(b)-(d), respectively. For the abnormal grain growth observed for Ni, there is no loss of low angle grain boundary fraction as the grain evolution progresses, also evident in Figure 5(a). For

Ni, after the onset of abnormal grain growth at 400°C, there is a significant increase in the fraction of  $\Sigma 3$ ,  $\Sigma 5$ ,  $\Sigma 7$ , and  $\Sigma 9$  boundaries, shown in Figures 5(b)-(e), respectively. After 450°C, there is a dramatic drop in the boundary fraction in  $\Sigma 3$  and  $\Sigma 9$  and gradual decrease in  $\Sigma 5$  and  $\Sigma 7$  when the monomodal grain size distribution was once again observed.

This increase is attributed to the high mobility of these special boundaries [9, 37, 46, 55]. The boundaries begin to undergo an expansion which facilitates the growth of a few grains. When these boundaries reach the surface, which is relatively easy because of the thin film geometry, they essentially grow out of the system, and as such no longer contribute to grain growth. At this point, the system returns to a monomodal grain size distribution and the CSL boundary fractions begin to return to their original, ambient temperature states. To investigate this concept of boundaries growing out of the sample, the morphology of a single abnormally growing grain is tracked against its neighbors at 250, 400, 450, and 500°C in Figure 7(a)-(d) in Ni.

In Figure 7(a), the grain (indicated by the arrow) in the center of the orientation map is of an  $\{001\}$  orientation with a  $\{111\}$  orientation grain growing through it. In the CSL map on the bottom of Figure 7(a), a network of  $\Sigma 3$  and  $\Sigma 9$  boundaries separating the two grains is plotted. After the Ni film was annealed at 400°C, Figure 7(b), the  $\{001\}$  orientation begins to dominate based its coverage fraction, and the  $\{111\}$  orientation consumed. In the CSL map on the bottom of Figure 7(b), the  $\Sigma 9$  boundary has dissipated from the grain while the  $\Sigma 3$  boundary is found separating the two grains. In Figure 7(c), the same region is presented after the film was annealed to 450°C. In this orientation map, the  $\{001\}$  orientation is still growing, while the  $\{111\}$  is continually being consumed. The CSL map in the bottom of Figure 7(c) shows that the  $\Sigma 3$  boundary is migrating downwards. At 500°C, Figure 7(d), it can be seen that the  $\{001\}$

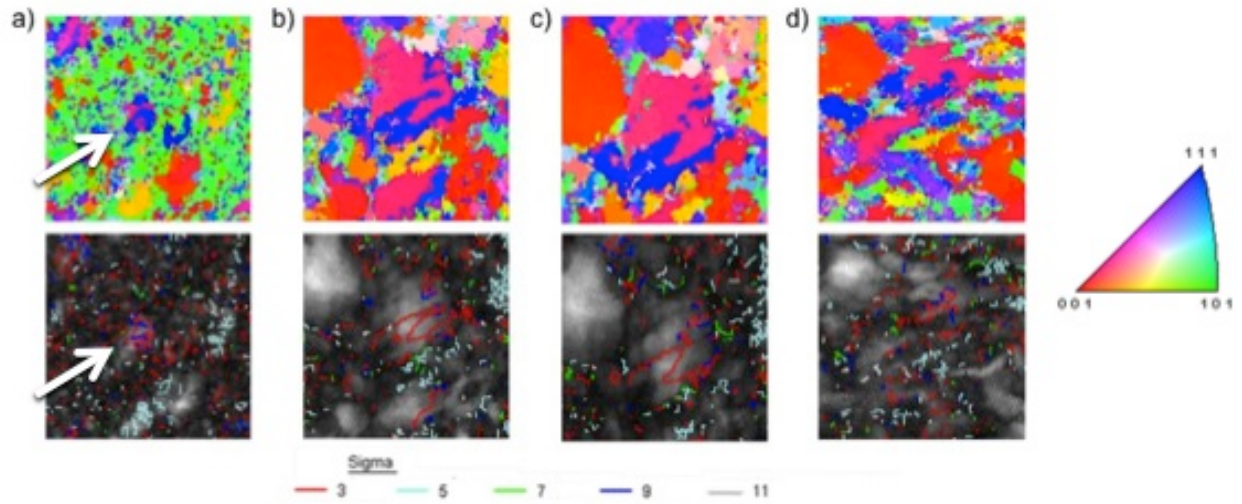


**Figure 2.7.** Evolution of Ni grains at various temperatures. a) 250 °C b) 400 °C c) 450 °C d) 500 °C . The top images are orientation maps and the bottom images are image quality maps with the CSL boundary type labeled. Each box is 1 $\mu$ m x 1 $\mu$ m

orientation has nearly completed consuming the  $\{111\}$  orientated grain. In the CSL map on the bottom of Figure 7(d), the  $\Sigma 3$  boundary length is significantly decreased compared to the previous plots in Figure 7(b)-(c). The loss of the  $\Sigma 3$  boundary length is suggestive that its high mobility allowed for the abnormal growth of this grain. The loss of this fast moving boundary caused the system to return to a more normal state of grain growth.

## 2.6 Conclusion

The current study has tracked grain morphology, boundary character, and grain orientation for a series of Cu and Ni films annealed up to 600°C. The Cu grains consumed the low angle grain boundaries with increases in the boundary fraction of  $\Sigma 3$ ,  $\Sigma 5$ ,  $\Sigma 7$ , and  $\Sigma 9$  during grain growth that led to a monomodal grain size distribution. Alternatively, Ni was found to undergo normal-to-abnormal-to-‘normal’ grain growth. The onset of abnormal grain growth resulted in no significant reduction of low angle boundaries but increases in the  $\Sigma 3$ ,  $\Sigma 5$ ,  $\Sigma 7$ ,  $\Sigma 9$ , and  $\Sigma 11$  boundary fractions and a texture evolution from  $\{101\}$  to  $\{001\}$ . The  $\Sigma 3$  and  $\Sigma 9$  boundaries peaked together during the abnormal grain growth stage. Their coincident behavior is contributed to twin boundaries. Once abnormal grain growth concluded the fraction of  $\Sigma 3$  and  $\Sigma 9$  boundaries returned to ambient temperature fraction values. This is contributed to these CSL boundaries possessing a high mobility allowing them to grow out of the system. It is concluded that strain energy minimization, *i.e.* texture evolution, surface energy minimization, and grain boundary mobility contribute to the onset of abnormal grain growth in the Ni film. The results of this work provide experimental validation of prior simulation work on the mobilities of boundaries and which may be contributing to abnormal grain growth.

## 2.7 Acknowledgements

This work was supported by support from the National Science Foundation through NSF-EPS-0814103. The authors also acknowledge Dr. Eric Homer for useful discussions on CSL boundaries.

## 2.8 References

1. Dannenberg R, Stach E, Groza JR, Dresser BJ. *Thin Solid Films* 2000;379:133.
2. Ebrahimi F, Li H. *Scripta Mater* 2006;55:263.
3. Olmsted DL, Foiles SM, Holm EA. *Acta Mater* 2009;57:3694.
4. Harada K, Tsurekawa S, Watanabe T, Palumbo G. *Scripta Mater* 2003;49:367.
5. Brandstetter S, Zhang K, Escudro A, Weertman JR, Van Swygenhoven H. *Scripta Mater* 2008;58:61.
6. Chen Z, Liu F, Wang HF, Yang W, Yang GC, Zhou YH. *Acta Mater* 2009;57:1466.
7. Kacher J, Robertson IM, Nowell M, Knapp J, Hattar K. *Mater Sci Eng A* 2011;528:1628.
8. Boyce BL, Padilla HA. *Metall Mater Trans A* 2011;42:1793.
9. Gruber J, George DC, Kuprat AP, Rohrer GS, Rollett AD. *Scripta Mater* 2005;53:351.
10. Holm EA, Hasson GN, Miodownik MA. *Acta Mater* 2001;49:2981.
11. Upmanyu M, Hassold GN, Kazaryan A, Holm EA, Wang Y, Patton B, et al. *Interface Sci* 2002;10:201.
12. Kinderlehrer D, Livshits I, Rohrer GS, Ta'asan S, Yu P. *Mater Sci Forum* 2004:1063.
13. Kazaryan A, Wang Y, Dregia SA, Patton BR. *Acta Mater* 2002;50:2491.
14. Gottstein G. *Physical Foundations of Materials Science*. New York: Springer; 2004.
15. Humphreys FJ, Hatherly M. *Recrystallization and related annealing phenomena*. Oxford: Elsevier; 1995.

16. Gottstein G, Shvindlerman LS. *Grain boundary migration in metals: thermodynamics, kinetics, applications*. Boca Raton (FL): CRC Press; 1999.
17. Haessner F, Hofman S. *Recrystallization of Metallic Materials*, Dr. Reiderer Verlag GmbH, Stuttgart; 1978:63.
18. Thompson CV. *Interface Sci* 1998;6:85.
19. Hattar K, Gregg J, Han J, Saif T, Robertson IM. *Mater. Res. Soc. Symp. Proc., Materials Research Society, Boston*, 2005.
20. Ruffino F, Grimaldi MG, Bongiorno C, Giannazzo F, Roccaforte F, Raineri V, Spinella C. *J Appl Phys* 2009;105:054311.
21. Ames M, Markmann J, Karos R, Michels A, Tschöpe A, Birringer R. *Acta Mater* 2008;56:4255.
22. Abraham M, Holdway P, Cerezo A, Smith GDW. *Mat Sci Forum* 2002;386-388:397.
23. Gottstein G, Shvindlerman LS, Zhao B. *Scripta Mater* 2010;62:914.
24. Rios PR, Glicksman ME. *Acta Mater* 2006;54:5313.
25. Srolovitz DJ, Grest GS, Anderson MP. *Acta Metall* 1985;33:2233.
26. Ling S, Anderson MP. *JOM* 1992;44:30.
27. Ivasishin OM, Shevchenko SV, Semiatin SL. *Scripta Mater* 2004;50:1241.
28. Rios PR. *Acta Metall* 1987;35:2805.
29. Upmánya M, Srolovitz DJ, Shvindlerman LS, Gottstein G. *Acta Mater* 1998;47:3901.
30. Demirel MC, Kuprat AP, George DC, Rollett AD. *Phys Rev Lett* 2003;90:016106.
31. Dillon SJ, Rohrer GS. *Acta Mater* 2009;57:1.
32. Holm EA, Olmsted DL, Foiles SM. *Scripta Mater* 2010;63:905.
33. Rybin WW, Titoviec J, Teplitskij DM. *Tiz Twierd Tiela* 1981;23:2000.
34. Randle V, Ralph B, Dingley D. *Acta Metall* 1988;36:267.
35. Capolungo L, Spearot DE, Cherkaoui M, McDowell DL, Qu J, Jacob KI. *J Mech Phys Solids* 2007;55:2300.

36. Chen C, Liu J, Wang Z. *Mater Sci Eng A* 2012;558:285.
37. Sutton AP, Balluffi RW. *Interfaces in Crystalline Materials*. Oxford: Clarendon Press; 1995.
38. Coffman VR, Sethna JP. *Phys Rev B* 2008;77:144111.
39. Randle V, Brown A. *Phil Mag A* 1989;59:1075.
40. Palumbo G, Aust KT. *Recrystallization* 1990;90:101.
41. Cheng L, Hibbard GB. *Mater Sci Eng A* 2008;492:128.
42. Hattar K, Follstaedt DM, Knapp JA, Robertson IM. *Acta Mater* 2008;56:794.
43. Hau-Riege SP, Thompson CV. *Appl Phys Lett* 2000;76:309.
44. Koo JB, Yoon DY. *Metall Mater Trans A* 2001;32A:1911.
45. Brandon D. *Acta Metall* 1966;14:1479.
46. Janssens KGF, Olmsted D, Holm EA, Foiles SM, Plimpton SJ, Derlet PM. *Nat Mater* 2006;5:124.
47. Holm EA, Hassold GN, Miodownik MA, *Acta Mater* 2001;49:2981.
48. Li J, Dillon SJ, Rohrer GS. *Acta Mater* 2009;57:4304.
49. Rohrer GS, Holm EA, Rollett AD, Foiles SM, Li J, Olmsted DL. *Acta Metall* 2010;58:5063.
50. Lim LC, Raj R. *Acta Metall* 1984;8:1177.
51. Rios PR. *Mater Sci Forum* 1996;204-206:247.
52. Zhang JM, Zhang Y, Xu KW. *J Cryst Growth* 2005;285:427.
53. Klement U, Erb U, El-Sherik AM, Aust KT. *Mater Sci Eng A* 1995;A203:177.
54. Kacher J, Robertson IM, Nowell M, Knapp J, Hattar K. *Mater Sci Eng A* 2011;528:1628.
55. Rohrer GS. *J Mater Sci* 2011;46:5881.
56. Remy L. 1975; PhD Thesis, Universite de Paris-Sud.

57. Venables JA. J Phys Chem Solids 1964;25:685.

**CHAPTER 3**  
**STUDYING THE EFFECTS OF NICKEL ADDITIONS**

**Submitted for Publication in *Thin Solid Films***

**Abnormalities Associated with Grain Growth in Solid Solution Cu(Ni) Thin Films**

J.G. Brons<sup>1</sup>, G.B. Thompson<sup>1</sup>

<sup>1</sup>The University of Alabama, Department of Metallurgical Engineering, Tuscaloosa, AL 35405

Keywords: Grain growth, thin film, precession-enhanced diffraction, abnormal growth, alloying

**3.1 Abstract**

A sputter-deposited Cu<sub>80</sub>Ni<sub>20</sub> solid solution film was heated *in situ* using a step-wise annealing schedule within a transmission electron microscope to observe the grain boundary character evolution associated with grain growth. The grain size distribution broadened with increasing temperature with a corresponding increase in the  $\Sigma 9$  boundary fraction. Particular grains grew at a faster rate than others, as compared to a Cu film, and is attributed to Ni segregation to the grain boundaries.

### 3.2 Introduction

Nanocrystalline metals are of interest for a variety of technological applications because of their grain size dependent mechanical [1,2], electrical [3], magnetic [4] and corrosion [5] properties. An inherent feature of nanocrystalline structures is the high fraction of grain boundaries within a given volume as compared to coarser grain materials. This increase in grain boundary fraction contributes to excess energy, which can result in grain growth at modest homologous temperatures [6-9]. In particular, when specific grains grow at a faster rate than their surrounding grains, referred to as abnormal grain growth, it has been shown to have detrimental effects on properties, such as mechanical fatigue life [8]. The origins of abnormal grain growth, particularly for single phase materials, are still a matter of much interest and research without a clear understanding of the governing mechanisms [10]. It is likely that grain boundary energies and their mobilities contribute to specific boundaries moving faster than others thereby allowing certain grains to grow preferentially.

Since such structural instability limits the application of nanocrystalline metals, researchers have attempted to stabilize these smaller grains. A mechanism proposed for improving the stability involves the reduction of grain boundary energy through the segregation of solute atoms to grain boundaries [11, 12, 13]. At elevated temperatures, the segregation of these solute atoms through alloying has been reported to minimize grain growth [14, 15, 16, 17]. Consequently, alloying can be used to extend the temperature range at which nanocrystalline structures could be preserved [13].

Thermal stability has often been associated with kinetic phenomena, where the addition of an alloying element decreases the grain boundary velocity. The structural stability may also be

enhanced by the preferential segregation of the solute to the grain boundary reducing the thermodynamic grain boundary energy [11, 13, 18, 19]. With this reduction in grain boundary energy, the driving force correspondingly would decrease. Specifically, Kim and Park [20] simulated grain boundary kinetics in terms of the segregation of solute atoms to the grain boundaries. They reported that when the driving force was small, the grain boundary velocity was low, allowing solute atoms to diffuse with the moving boundary. In this regime, migration kinetics are governed by solute diffusion near the grain boundary [20]. As the driving force increases, solute atoms gradually resist grain boundary motion, resulting from the increased grain boundary velocity [21]. To date, there have been limited experimental studies that have quantified the grain boundary evolution during grain growth for an alloyed material where such effects may occur.

The authors recently published a comparison between Cu and Ni grain growth [22]. The microstructural evolution for these thin films was characterized by quantifying the change in grain size, grain morphology, and grain-to-grain misorientation using precession-enhanced electron diffraction (PED). The Cu film exhibited grain growth which maintained a monomodal grain size distribution. This growth was accompanied by a consumption of the low-angle grain boundaries and an increase in the  $\Sigma 3$ ,  $\Sigma 5$ , and  $\Sigma 7$  coincidence site lattice (CSL) boundary fractions. The Ni film underwent transitions from monomodal-to-bimodal-to-monomodal grain size distributions [22]. The onset of the bimodal grain size distribution was accompanied by an increase in the  $\Sigma 3$  and  $\Sigma 9$  boundary fractions [22]. When these CSL boundaries were reduced in length, the grain size distribution returned to a monomodal growth state indicating their importance in the irregular grain size evolution. Clearly, these two face-centered cubic metals (FCC) exhibit different grain growth characteristics.

The Cu-Ni alloy provides an interesting case study, since each pure film exhibits different grain growth behaviors. Additionally, both Cu and Ni have mutual solid solubility, retaining the single-phase FCC structure. Surface segregation has been intensively studied for CuNi [23, 24] because of its importance in catalysis, with evidence that Ni segregates to grain boundaries for Cu-rich alloys. [25]. Consequently, such preferential Ni segregation to the grain boundaries of Cu could alter the self-similar grain evolution in Cu. In this study, a co-sputtered Cu<sub>80</sub>Ni<sub>20</sub> film was subjected to a similar annealing schedule as that previously reported for the Cu and Ni films [22]. Since the behavior of the two metal films, in their pure state, is known, the influence of alloying can be inferred from the experimental results and can provide new insights into how grain boundary character is influenced with solute alloying.

### 3.3 Experimental

Alloyed nanocrystalline thin films of Cu and Ni with an approximate composition of Cu<sub>80</sub>Ni<sub>20</sub> were sputter deposited in an AJA ATC-1500 stainless steel magnetron-sputtering system to an approximate thickness of 45 nm onto 100 nm thick DuraSiN<sup>TM</sup> substrates. The deposited film thickness allowed for electron transparency without further preparation. Fiducial markers were focused ion beam (FIB) milled into the film using an FEI Quanta dual-beam FIB. These markers allowed for correct repositioning of the 1 x 1 μm region of interest (ROI) after each heating experiment to ensure that the same boundaries in the ROI were tracked. The fiducial markers were placed at a distance of 20 x 20 μm from the ROI to make certain there were no edge effects from the markers themselves influencing the grain growth behavior. The film's composition was then verified using energy dispersive spectroscopy (EDS) within the transmission electron microscope (TEM). To anneal the films *in situ*, a Gatan 652 double-tilt

heating holder was utilized in the FEI Tecnai Supertwin TEM operated at 200 keV. As described by Hattar *et al.* [26], the temperature of the Gatan heating stages is accurate within a few degrees. The temperature schedule, determined from previous experimentation, was ambient (30 °C), 250 °C, 400 °C, 500 °C, and 600 °C.

PED was then employed with a 1° angle of precession and a scanning step size of 10 nm to determine the grain morphology, the grain size, and the grain-to-grain misorientation. The details of how the nanoMEGAS ASTAR platform produces a PED orientation map can be found in reference [27]. In order to avoid thermally-induced drifting during the orientation mapping, the films were heated to and held at the desired temperature for ~40 minutes to allow for grain growth, then cooled back to ambient temperature by turning off the heating source and allowing the stage to equilibrate before performing the PED scan. In previous research [28], grain growth appeared to be complete after about 15 minutes of annealing, so the selected annealing time of 40 minutes is considered to be sufficient to allow for grain growth.

### 3.4 Results

Figures 1(a-e) present the orientation maps collected at the five annealing temperatures: 30, 250, 400, 500, and 600 °C, respectively. Each map shows the same ROI, allowing individual grains and grain boundaries to be tracked. In Figure 1(a), the film was mostly comprised of {101} orientated grains, with a minor fraction of randomly orientated grains near the  $\bar{1}13$  orientation. As the annealing experiment progressed, these  $\bar{1}13$  oriented grains underwent the most growth, with the {101} grains being consumed in the process. After the 600 °C anneal, Figure 1(e), these  $\bar{1}13$  oriented grains had grown significantly larger than the surrounding grains.

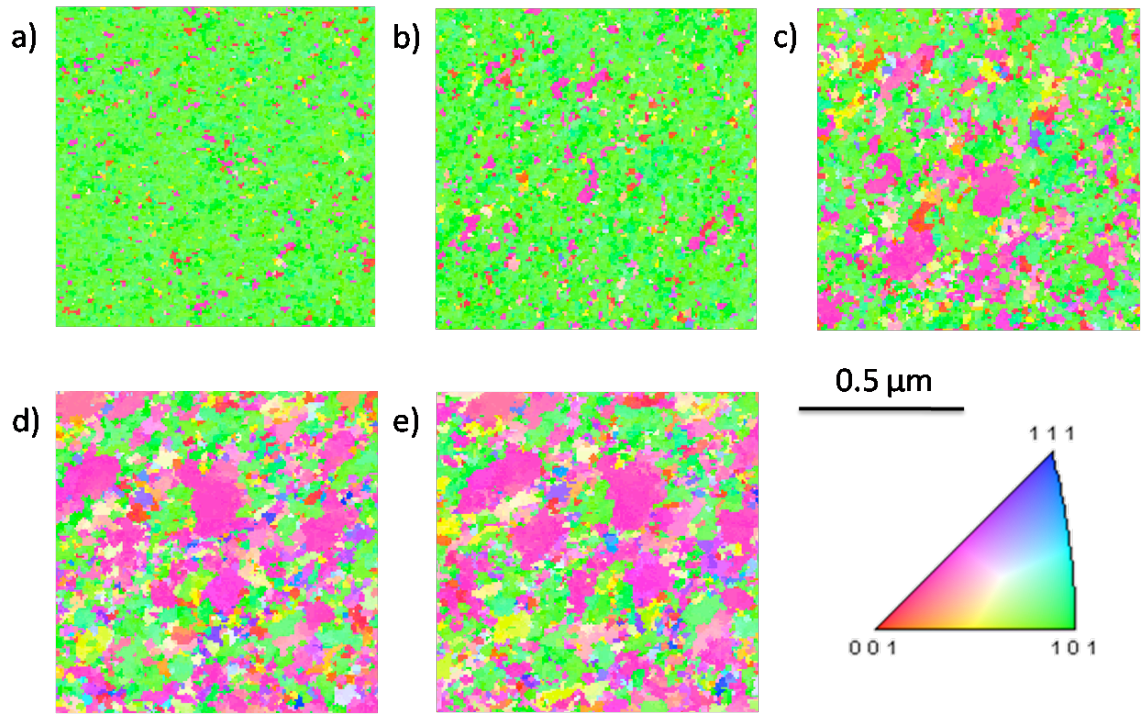


**Figure 3.1.** PED orientation maps of a  $1\mu\text{m} \times 1\mu\text{m}$  region of interest at pre-determined temperatures (a)  $30^\circ\text{C}$  (b)  $250^\circ\text{C}$  (c)  $400^\circ\text{C}$  (d)  $500^\circ\text{C}$  (e)  $600^\circ\text{C}$  and (f) inverse pole figure

The grain size distributions from each of the annealing temperatures are presented in Figure 2. Initially, more than 90% of the grains (by area) had a diameter less than 100 nm and 40% of the grains (by area) had a diameter less than 50 nm. As annealing progressed, the grain size distribution significantly broadened, and the largest grains underwent significant growth. After the 600 °C anneal, 40% of the grains (by area) had diameters less than 75 nm, with 80% of the grains (by area) having a diameter measuring less than 175 nm. There was a small subset of grains that grew to sizes larger than 500 nm in diameter.

Initially, the grain size distribution was monomodal, with an average grain size of  $34.8 \pm 15.2$  nm. After the 600 °C anneal, the average grain size increased to  $41.2 \pm 27.5$  nm. Though the grain size distribution has broadened significantly, with some of the largest grains being upwards of 500 nm, it is still considered to be a monomodal distribution since the standard deviation of the mean does not exceed twice that value [29]. The inability to clearly prove abnormal grain growth (bimodal distribution) may be a result that the number of counted grains decreases within the fixed ROI as the grains evolve.

To investigate the types of grain boundaries that developed during grain growth, the boundary fractions for specific low- $\Sigma$  CSL boundaries ( $\Sigma 1$ ,  $\Sigma 3$ ,  $\Sigma 5$ ,  $\Sigma 7$ ,  $\Sigma 9$ , and  $\Sigma 11$ ) were plotted against those previously observed in the Cu film [22], Figures 3(a-f), respectively. There was initially a much higher low-angle boundary fraction and a significantly lower  $\Sigma 3$  boundary fraction, Figures 3(a) and (b), respectively, between the pure and solid solution films. As the annealing progressed, the low angle grain boundaries were consumed, similar to the previous Cu [22]. The fraction of  $\Sigma 3$  boundaries in the  $\text{Cu}_{80}\text{Ni}_{20}$  alloy, however, was measured at an order of magnitude lower than in Cu. This fraction increased until 400 °C, at which point the  $\Sigma 3$  boundary fraction stayed relatively constant. The fraction of  $\Sigma 5$  boundaries also increased, in a

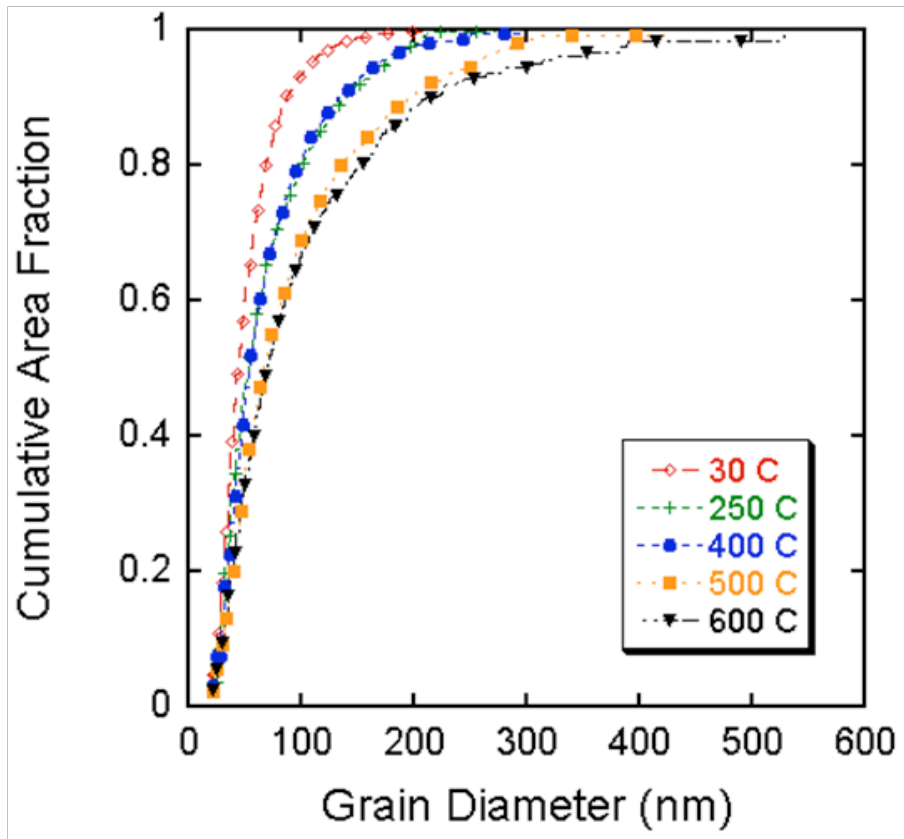


**Figure 3.2.** Cumulative grain size distribution plot quantifying each of the annealing temperatures

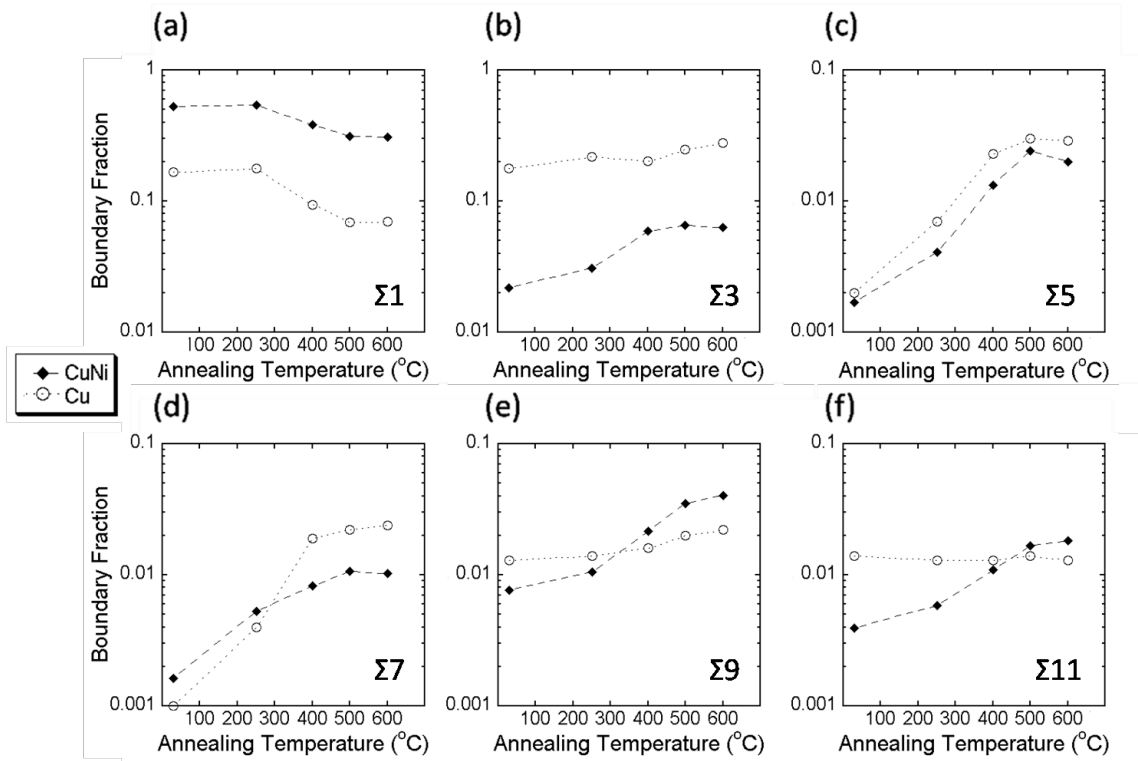


**Figure 3.3.** The evolution of the CSL boundary fractions in Cu<sub>80</sub>Ni<sub>20</sub> and Cu [6] as a function of the annealing temperature (a) Σ1 (b) Σ3 (c) Σ5 (d) Σ7 (e) Σ9 (f) Σ11

very similar manner to that of the pure Cu film [22]. The discrepancy between the previously studied Cu [22] and the Cu<sub>80</sub>Ni<sub>20</sub> alloy was in the  $\Sigma 9$  and  $\Sigma 11$  boundary fractions, Figure 3(e) and (f), respectively. While the  $\Sigma 9$  fraction in the previous study [22] remained relatively constant, the  $\Sigma 9$  boundary fraction for the alloy increased by a factor of five. The same increase was observed in the  $\Sigma 11$  boundary fraction, as well, while the  $\Sigma 11$  fraction decreased in the previously studied Cu film [22].

### 3.5 Discussion

It is clear from the results, significant differences in CSL boundary evolution occurred with the addition of Ni to the Cu thin film. After annealing at 600 °C, the Cu [22] grain size distribution was  $57.1 \pm 41.15$  nm, as compared to the Cu<sub>80</sub>Ni<sub>20</sub> being  $41.2 \pm 27.5$  nm; the alloying actually decreased the average grain size and the standard deviation of the mean, although graphically, it can be seen that alloying widened the distribution and increased the size of the largest grains. This lower mean grain size is attributed to the high fraction of small grains surrounding the larger  $\{\bar{1}13\}$  grains in the alloy. This variation is attributed to the differences in CSL boundary fraction evolution, which is likely associated with changes in grain boundary mobility. In Figure 3, the evolution of the CSL boundary fraction, as a function of annealing temperature, is presented, and in Figure 4(a-c), the PED orientation maps collected at 400, 500, and 600 °C, are presented with their corresponding CSL boundaries overlaid onto image quality maps.

Three evolving  $\{\bar{1}13\}$  oriented grains are indicated by arrows in the center of Figures 4(a-c). These grains grow to a much larger size than the surrounding matrix grains in the orientation maps. At 400 °C, Figure 4(a), the three  $\{\bar{1}13\}$  grains are outlined by  $\Sigma 9$  boundaries, and there is a

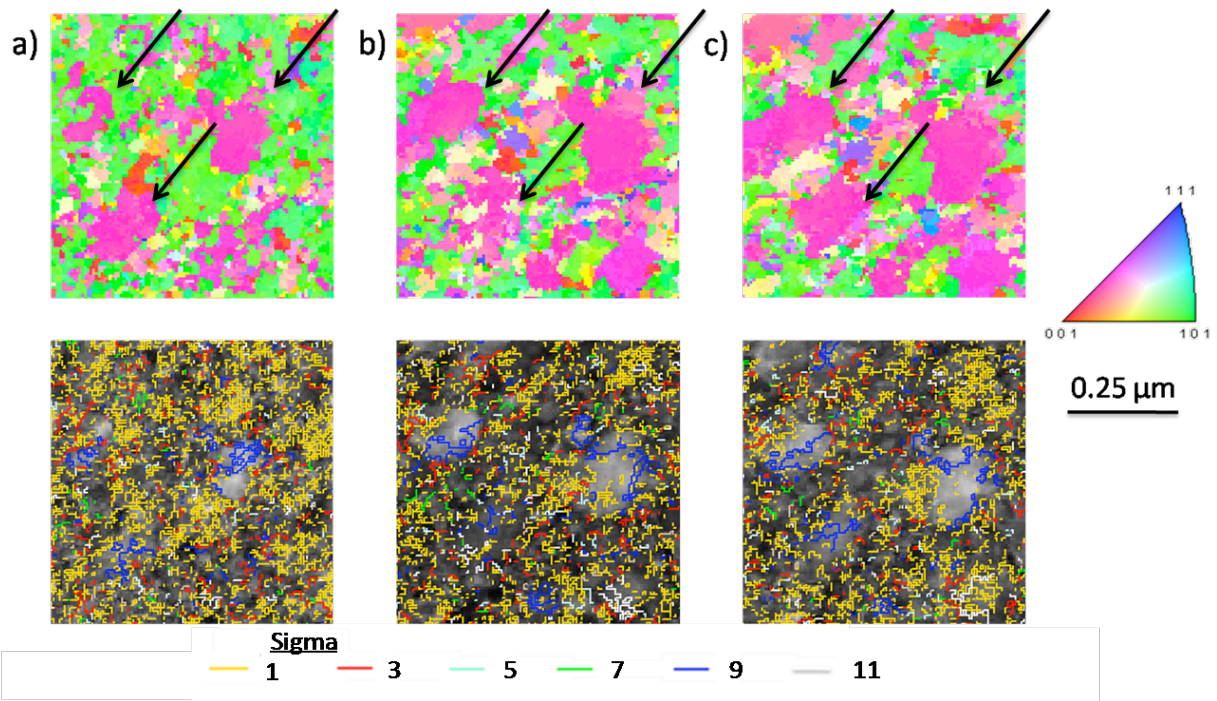


**Figure 3.4.** PED orientation maps and image quality maps with CSL boundaries overlaid at (a) 400°C (b) 500°C (c) 600°C

high density of low angle grain boundaries within the matrix. After annealing at 500 °C, Figure 4(b), these larger grains are still outlined by  $\Sigma 9$  boundaries, which have expanded, and the density of the low angle grain boundaries in the matrix has decreased. Finally, after annealing at 600 °C, Figure 4(c), the  $\{113\}$  oriented grains have evolved to an even larger size, and the  $\Sigma 9$  boundaries have continued to expand with the growth of these grains.

Atomistic simulations of nanocrystalline Cu alloys have shown that structural stabilization is contingent upon the distribution and character of the solute atom, and a certain minimum concentration of solute is necessary for grain size stabilization [30-32]. In the  $\text{Cu}_{80}\text{Ni}_{20}$  alloy investigated, the concentration of the solute within the alloy should be well above the required minimum needed for grain stabilization. Unfortunately, there have been a limited number of studies to determine which CSL boundaries would be more preferable for solute segregation than others [33-35]. Most numerical studies arbitrarily place solute atoms at the grain boundaries to determine their effect on grain boundary energy [30-32, 36]. Divinski et al. [37] measured grain boundary diffusivity of Ni in polycrystalline Cu to quantify grain boundary segregation. The results of Ni diffusivity around specific boundaries were also presented [37], and their results appear to contradict the general trend that special grain boundaries, with a low- $\Sigma$  number, are represented by “cusps” in the angle dependence of grain boundary diffusivity. Divinski et al. [37] also found that the absolute values of Ni grain boundary diffusivity are significantly smaller than the grain boundary self-diffusion of Cu. The larger surface tension value of Ni, in comparison to that of Cu, forces Ni to occupy sub-interface sites and slows down the Ni grain boundary diffusivity. This could be especially relevant for a thin film geometry where surface effects, such as grooving, could occur.

Since Ni is known to segregate in a Cu-rich alloy [37], it is reasonable to expect that the solute segregation could be a function of boundary type. Rapid grain boundary expansion was prevalent for the  $\Sigma 9$  boundary, and this is suggestive of the Ni solute atmosphere having little effect on the mobility of the  $\Sigma 9$  boundary. Consequently, a lower solute concentration at this boundary, relative to other boundaries, would reduce the solute drag effect [21]. This also suggests that solute drag can influence preferential grain growth under the specific circumstance in which a portion of the grain boundaries are allowed to break away from the solute atmosphere [20].

Aust and Rutter [38-40] proposed an alternative explanation that specific CSL boundaries could be less influenced by the addition of solute atoms. They suggested that the solute atoms could increase the atomic packing for specific CSL boundaries, which would lead to lower interaction energy for the motion normal to the boundary. This would then result in a reduction in the transition velocity, thereby allowing boundaries to migrate further in the high boundary velocity regime as compared to non-CSL boundaries [38-40]. The measured boundary fraction of  $\Sigma 9$  in this study continued to increase at each of the annealing steps. This is suggestive that the addition of Ni atoms allowed for the  $\Sigma 9$  boundary to possess a lower energy than the pure Cu film [22] previously studied.

Lee and Richards [41] reported that the CSL density decreased in pure Ni with increasing grain growth. This was attributed to minimization of the solute-boundary interactions which inhibited the mobility in low-energy boundaries. The conclusion of their work and the work of Schlegel et al. [42] was that annealing might increase the CSL boundary fraction in high-purity metals, while the CSL boundary fraction can be expected to decrease with grain growth in samples with impurities. In the experimental results of this paper, the boundary fractions of the

$\Sigma 3$ ,  $\Sigma 5$ , and  $\Sigma 7$  boundaries were considerably lower than those previously measured in Cu [22] and would be in agreement with conclusions discussed above. The only significant exception would be the  $\Sigma 9$  boundary, which increased in boundary fraction suggesting the influence of grain boundary segregation is more complex. The experimental results of this study provide forward feeding direction for future computational studies to focus on which specific CSL boundaries are affected by solute additions, so that the extent of Ni segregation on grain boundary energies and mobilities can be better elucidated.

### 3.6 Conclusions

A sputter-deposited  $\text{Cu}_{80}\text{Ni}_{20}$  thin film was annealed within a TEM in order to investigate the grain boundary character evolution associated with the observed grain growth. The grain size distribution for the alloy film was much broader than the previously investigated Cu film [22]. In addition, alloying led to a preferential evolution of  $\{\bar{1}13\}$  orientated grains. The boundary fraction of  $\Sigma 9$ , for the alloy film, was a factor of five larger than the pure Cu film. Additionally, the  $\Sigma 9$  were also directly associated with the large  $\{\bar{1}13\}$  orientated grains. From these results and previous published models [30-32, 36,37], it is proposed that the Ni additions occupied sub-interface sites as a result of Ni's higher surface tension which impeded motion of other CSL boundaries (e.g.  $\Sigma 3$  and  $\Sigma 7$ ). Though solute segregation has been proposed as a means to stabilize nanocrystalline grain structures [13] and appears promising, solute preference to specific CSL boundaries can result in abnormalities in grain growth and lead to destabilization of the grain structure. Further work in determining the extent of solute segregation as a function of CSL boundary type is needed.

### 3.7 Acknowledgements

This research was funded by the National Science Foundation through grant number EPS-0814103.

### 3.8 References

1. K.S. Kumar, H. Van Swygenhoven, S. Suresh. *Acta Mater.* 51 (2003) 5743.
2. M.A. Meyers, A. Mishra, D.J. Benson. *Prog Mater Sci.* 51 (2003) 387.
3. L. Lu, Y.F. Shen, X.H. Chen, L.H. Qian, K. Lu. *Science* 304 (2004) 422.
4. G. Herzer, *J Magn Magn Mater.* 294 (2005) 99.
5. L.P. Wang, J.Y. Zhang, Y. Gao, Q.J. Xue, L.T. Hu, T. Xu. *Scripta Mater.* 55 (2006) 657.
6. D.S. Gianola, D.H. Warner, J.F. Molinari, K.J. Hemker. *Scripta Mater* 55 (2006) 649.
7. D.S. Gianola, S.V. Petegem, M. Legros, S. Brandstetter, H.V. Swygenhoven, K.J. Hemker. *Acta Mater.* 54 (2006) 2253.
8. B.L. Boyce, H.A. Padilla. *Metall Mater Trans A* 42A (2011) 1793.
9. K. Zhang, J.R. Weertman, J.A. Eastman. *Appl Phys Lett* 87 (2005) 061921.
10. A. Kazaryan, Y. Wang, S.A. Dregia, B.R. Patton. *Acta Mater.* 50 (2002) 2491.
11. R. Kirchheim. *Acta Mater.* 50 (2002) 413.
12. J. Weissmuller. *Nanostruct Mater.* 3 (1993) 261.
13. A.J Detor, C.A. Schuh. *Acta Mater.* 55 (2007) 371.
14. E. Chassaing, M.P. Roumegas, M.F. Trichet. *J Appl Electrochem.* 25 (1995) 667.
15. A.O. Aning, Z. Wang, T.H. Courtney. *Acta Mater.* 41 (1993) 165.
16. T. Yamasaki, P. Schlossmacher, K. Ehrlich, Y. Ogino. *Nanostruct Mater.* 10 (1998) 375.
17. C.E. Krill, H. Ehrhardt, R. Birringer. *Z Metallkd.* 96 (1995) 1134.

18. F. Liu, R. Kirchheim. *J Cryst Growth*. 264 (2004) 385.
19. R. Kirchheim. *Acta Mater*. 50 (2002) 413.
20. S.G. Kim, Y.B. Park. *Acta Mater*. 56 (2008) 3739.
21. J.W. Cahn. *Acta Metall*. 10 (1962) 789.
22. J.G. Brons, G.B. Thompson. *Acta Mater*. 61 (2013) 3936.
23. T. Sakurai, T. Hashizume, A. Kobayashi, A. Sakai, S. Hyodo, Y. Kuk, H.W. Pickering. *Phys Rev B*. 34 (1986) 8379.
24. J.D. Rittner, D.N. Seidman. *Acta Mater*. 45 (1997) 3191.
25. T. Sakurai, T. Hashizume, A. Jimbo, A. Sakai, S. Hyodo. *Phys Rev Lett*. 55 (1985) 514.
26. K. Hattar, D.M. Follstaedt, J.A. Knapp, I.M. Robertson. *Acta Mater* 56 (2008) 794.
27. K. Hattar, J. Gregg, J. Han, T. Saif, I.M. Robertson. *Mater Res Soc Symp Proc., Materials Research Society, Boston* (2005).
28. J.B. Koo, D.Y. Yoon. *Metall Mater Trans A* 32A (2001) 1911.
29. J.L. Devore, R. Peck. (1997) *Statistics: The Exploration and Analysis of Data*. Belmont, CA: Duxbury Press.
30. P.C. Millett, R.P. Selvam, S. Bansal, A. Saxena. *Acta Mater*. 53 (2005) 3671.
31. P.C. Millett, R.P. Selvam, A. Saxena. *Acta Mater*. 54 (2006) 297.
32. P.C. Millett, R.P. Selvam, A. Saxena. *Acta Mater*. 55 (2007) 2329.
33. D. Bedorf, S.G. Mayr. *Scr Mater*. 57 (2007) 853.
34. S.G. Mayr, D. Bedorf. *Phys Rev B*. 76 (2007) 24111.
35. S.G. Mayr, D. Bedorf. *Phys Rev B*. 76 (2007) 24111.
36. R. Rajgarhia, D. Spearot, A. Saxena. *Metall Mater Trans A*. 41 (2010) 854.
37. S. Divinski, J. Ribbe, G. Schmitz, C. Herzig. *Acta Mater*. 55 (2007) 3337.
38. K.T. Aust, J.W. Rutter. *Trans Met Soc AIME*. 215 (1959) 119.
39. K.T. Aust, J.W. Rutter. *Trans Met Soc AIME*. 215 (1959) 820.

40. J.W. Rutter, K.T. Aust. *Trans Met Soc AIME*. 218 (1960) 682.

41. S.L. Lee, N.L. Richards. *Mater Sci Eng*. 405 (2005) 74.

42. S.M. Schlegel, S. Hopkins, M. Frary. *Scripta Mater*. 61 (2009) 88.

## CHAPTER 4

### CRYOGENIC INDENTATION-INDUCED GRAIN GROWTH

Copyright © 2013 Scripta Materialia Inc. Published by Elsevier Ltd.

#### Cryogenic Indentation-Induced Grain Growth in Nanotwinned Copper

J.G. Brons<sup>1</sup>, H.A. Padilla II<sup>2</sup>, G.B. Thompson<sup>1</sup>, B.L. Boyce<sup>2</sup>

<sup>1</sup>The University of Alabama, Department of Metallurgical Engineering, Tuscaloosa, AL 35405

<sup>2</sup>Sandia National Laboratories, Albuquerque, NM

Keywords: grain growth, indentation, nanotwin Cu, cryogenic grain growth, precession enhanced electron diffraction

#### 4.1 Abstract

Nanocrystalline Cu thin-films with as-deposited  $\Sigma 3$  twin boundaries were indented while immersed in liquid nitrogen. Quantification using precession-enhanced electron diffraction determined the crystallographic texture and grain-to-grain misorientation of the undeformed, pile-up, and compressed regions. Grains in the undeformed region retained a high density of  $\Sigma 3$  recrystallization twins whereas the pile-up showed significant coarsening, prevalent  $\Sigma 7$  subgrain formation and a decrease in twin boundaries. The abnormal grain growth is attributed to a detwinning mechanism. The compressed region showed significant grain refinement.

## 4.2 Introduction

Classically, grain growth is considered to be the product of a driving force and intrinsic boundary mobility. Driving forces originate from stored deformation energy, grain boundary energy, surface energy, elastic energy, or from a chemical and/or thermal gradient [1]. Boundary mobility refers to the kinetics necessary to allow the atoms to move in response to that driving force. Lack of sufficient mobility and driving force prevents systems from achieving their lowest energy microstructural configuration. Since mobility is thought to be related to atomic diffusion, temperatures of approximately one-half or higher of the homologous temperature ( $T_m$ ) are usually required to observe substantial grain growth [2]. When the grain growth is self-similar, it is referred to as normal growth. In some cases, a single grain or an aggregate of grains coarsen at a faster rate than others in the microstructure and is referred to as abnormal grain growth (AGG).

As grain sizes approach the nanometer regime, they can exhibit peculiar grain growth behavior not observed in larger grains. For example, nanocrystalline metals have been shown to undergo both moderate, widespread coarsening as well as dramatic AGG as a result of monotonic tensile deformation [3], high cycle fatigue [4], low cycle fatigue [5], and indentation [6] at moderate ( $<0.5T_m$ ) to low ( $\ll 0.5T_m$ ) temperatures. In the case of fine-grained Cu, samples that are simply left at room temperature have been shown to display abnormal coarsening [7]. Zhang *et al.* [6] have reported transmission electron microscopy (TEM) studies where AGG at room temperature occurred under *in situ* indentation. In this report, the starting grain size was 40 nm. After indentation, certain grains achieved sizes of nearly 300 nm. Even more surprising was a series of *ex situ* cryogenic indentations at  $-190^\circ\text{C}$  where the grains grew up to 700 nm. At

temperatures of a few hundred °C, typical boundary velocities for Cu are on the order of  $10^{-9}$  m/s [1]; at -190°C one might expect grain boundary migration to occur only on geologic timescales. To date, the ability for grains to grow under cryogenic indentation, where low temperatures are insufficient for reasonable mobility, is not well understood.

In this letter, a series of nanocrystalline copper films with a high density of twins have been subjected to indentation at liquid nitrogen temperatures. The films' grain boundary misorientations were quantified to understand which grain boundary types are present *after* cryogenic mechanically-induced grain growth. These remnant grain boundaries could be either pre-existing from the parent grain structure or induced by indentation, such as subgrains or cell walls; they could be either active boundaries which are responsible for grain growth or static boundaries which impede grain growth.

### 4.3 Experimental

Copper films ~500 nm thick were grown by a pulsed laser deposition (PLD) technique onto a polished 0.5 mm thick silicon substrate. The deposition was accomplished using a previously described setup [8] which has been upgraded with a 248 nm KrFeximer laser operating at 35 Hz and 500mJ. The base pressure during deposition was  $4 \times 10^{-7}$  torr. The deposition process led to columnar-type grains normal to the substrate with a high density of twin boundaries, oriented either horizontally or inclined to the substrate, as determined through TEM micrographs shown and discussed later in the letter. This type of microstructure is described as 'nanotwinned'. The twin-to-twin spacing was typically on the order of tens of nanometers. X-ray diffraction (XRD) measurements confirmed that the film had a strong {111} and weak {200} out-of-plane texture intensities.

Cryogenic indentation of the Cu film was carried out using a custom-built immersion indenter, shown schematically in Figure 1a. A sample is held in place by a spring loaded platen, visible in Figure 1a. The hollow tube allows a long rod to raise and lower the carriage containing the Vickers indenter tip, attached to a lightweight shuttle (Figure 1b). The shuttle holds the indenter tip normal to the sample, as well as serving to support small cylindrical tungsten weights, which can be added to increase the normal force applied during indentation (Figure 1c). For this experiment, additional weights were used to achieve 0.5 N normal force. The assembly was designed to operate either during immersion in a liquid cryogen or in air. For this experiment, the sample was submerged in liquid nitrogen (LN<sub>2</sub>). A 1 cm x 1 cm film-on-substrate sample was held in place by a spring-loaded platen, Figure 1b, after which the assembly head was submerged until rapid boiling of the LN<sub>2</sub> ceased signifying that the indenter temperature had equilibrated with its environment. The shuttle carriage was then lowered at a rate of approximately 0.08 mm/s until the indenter tip contacted the sample surface (Figure 1c) and held for 60 seconds. After 60 seconds of indentation, the tip was retracted and the sample was removed from the LN<sub>2</sub> and allowed to warm by sitting at room temperature.

Samples from the pre- and post- indentation film were prepared for TEM analysis with a focused ion beam (FIB) milling and lift out procedure [9] using a FEI Quanta 3D dual beam FIB with an *in situ* Omniprobe lift out micromanipulator. For the post-indentation sample, the site specific region was extracted such that the undeformed, pile-up, and compressed regions of the indent were captured in one foil. During the final milling steps, the acceleration voltage was reduced from 30 to 5 keV to reduce surface milling damage. After the foil had been extracted and attached to a TEM grid, the TEM specimen was polished further using a Gatan Precision Ion Polishing System (PIPS) at 2.5keV, 1.0 mA, and an inclination angle of 8 degrees. This last step

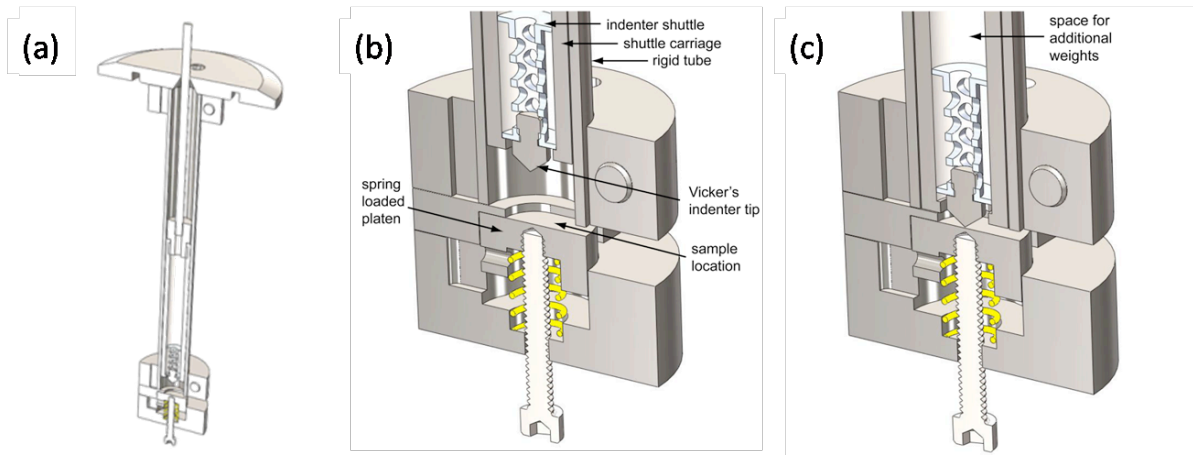


**Figure 4.1.** Cross-section schematic showing (a) components of the indenter apparatus as well as the (b) unloaded and (c) loaded positions. Cylindrical weights and sample are not shown.

was found to significantly improve foil quality by removing any residual FIB damage, yielding crisp bright field and precession-enhanced diffraction patterns. Particular care in preparation minimized any possibility of ion beam induced effects on grain growth [9]. The localized nature of the indentation facilitated side-by-side comparison of the as-deposited and deformed grain structures.

The TEM foils were analyzed in a FEI Tecnai F20 Supertwin TEM operating at an accelerating voltage of 200 kV and fitted with a NanoMEGAS© precession-enhanced diffraction orientation identification platform [10]. The NanoMEGAS platform generates pseudo-kinematical electron diffraction conditions, which allows grain orientation to be measured at a spatial resolution of  $\sim 10$  nm. This facilitates the collection and analysis of not only grain size but also misorientation distributions. The precession angle used was 1 degree at step sizes of 10 nm.

#### **4.4 Results**

The cross-sectional inverse pole figure orientation map of the undeformed film is shown in Figure 2b. A prevalence of  $\Sigma 5$  boundaries and low-angle boundaries at the substrate surface, where growth was initiated, is evident in the color trace map of boundary type. The columnar grains from the initial growth surface are separated by these series of low-angle grain boundaries, Figure 2c. Within these columnar grains,  $\Sigma 3$  twin boundaries spanned the grains' diameters. Brandon's criterion [11] was used to distinguish the misorientation range of these coincident site lattice values. In Figure 2d, the twins

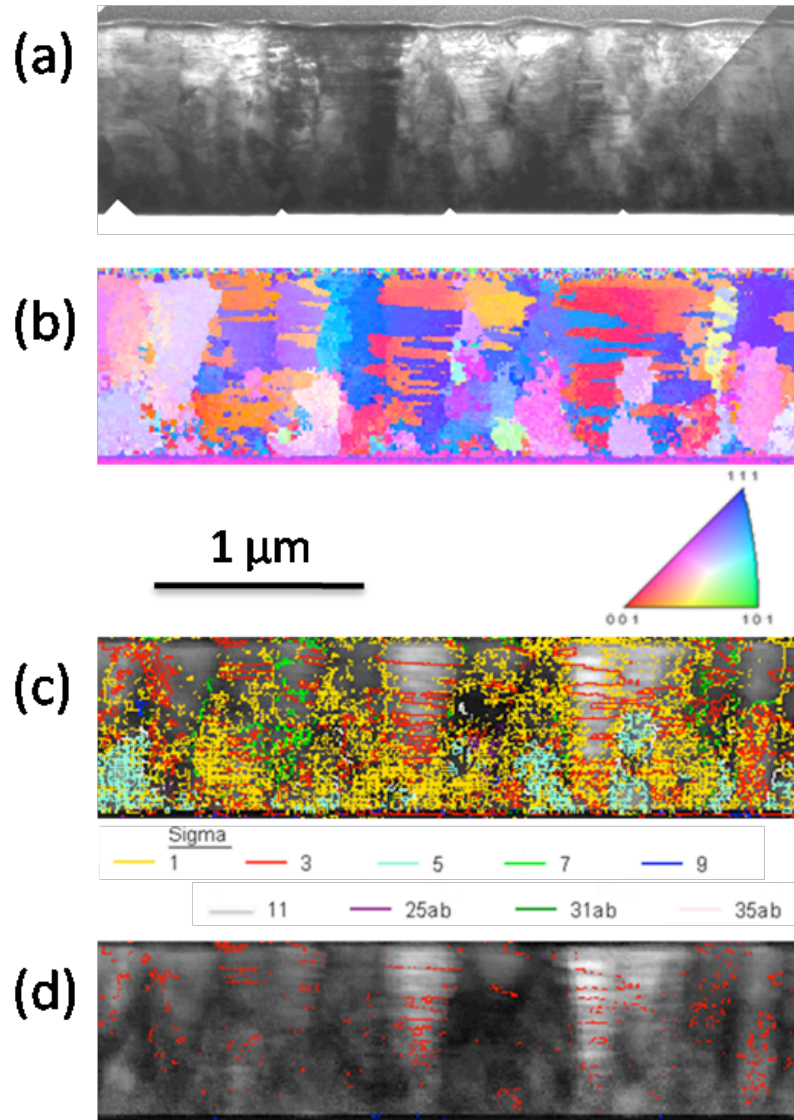


**Figure 4.2.** As-deposited nanotwinned Cu film in cross-section (a) TEM bright field image (b) inverse pole figure orientation map (c) image quality map with CSL boundaries highlighted (d) image quality map with twin boundaries highlighted in red

shown in red are the primary recrystallization twins with a plane normal of  $\{111\}$  and a direction of  $\langle 111 \rangle$ .

After cryogenic indentation, a complimentary series of images were captured in the indented material. Figure 3a shows SEM plan and tilted views of an indented region, with indication of the orientation of the cross-sectional FIB milling. The grain orientation map of the indented sample is shown in Figure 3c. Within this figure, clear evidence of grain coarsening is present in the pile-up region near the edge of the indent. Many of these coarsened grains show what appear to be lamellar twin structures. The grains in the central region of the indent have undergone significant refinement. Outside the indented region (labeled 'undeformed' in Figure 3c), the material resembles the pre-tested images of Figure 2 providing confidence that the grain size changes are not from the specimen preparation. In Figure 3d, the CSL boundaries in the indented sample are mapped. It can be seen that the large lamellar grains in the pile-up region are separated by  $\Sigma 3$  boundaries with  $\Sigma 7$  subgrain boundaries within these large grains. The low angle grain boundaries seem to be depleted within the pile-up region as well. Although the large grains are separated by  $\Sigma 3$  boundaries, Figure 3e reveals very few twin boundaries within the pile-up region as compared to the undeformed region on the left of the pile-up.

#### **4.5 Discussion**

Clearly, the indentation of the nanotwinned film resulted in substantial AGG in the pile-up region. This is most evident by the cumulative density function of grain size for the different regions as shown in Figure 4a. In the undeformed region, a high fraction of low-angle,  $\Sigma 3$  and

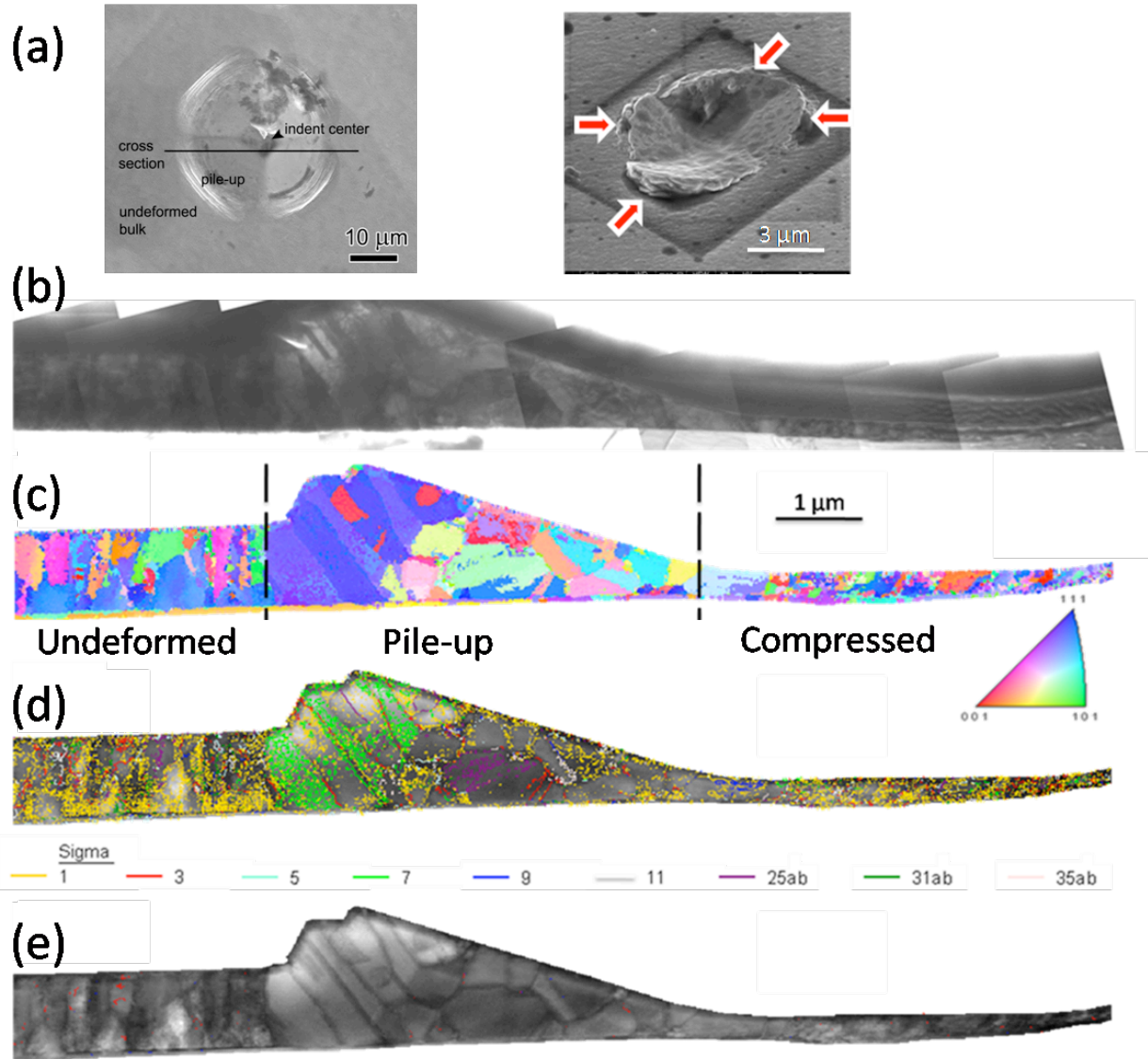


**Figure 4.3.** Indented nanotwinned Cu film in (a) SEM image of indent with lines/arrows showing site specific foil lift-out locations (b) TEM bright field image (c) inverse pole figure orientation map (d) image quality map with CSL boundaries highlighted (e) image quality map with twin boundaries highlighted in red

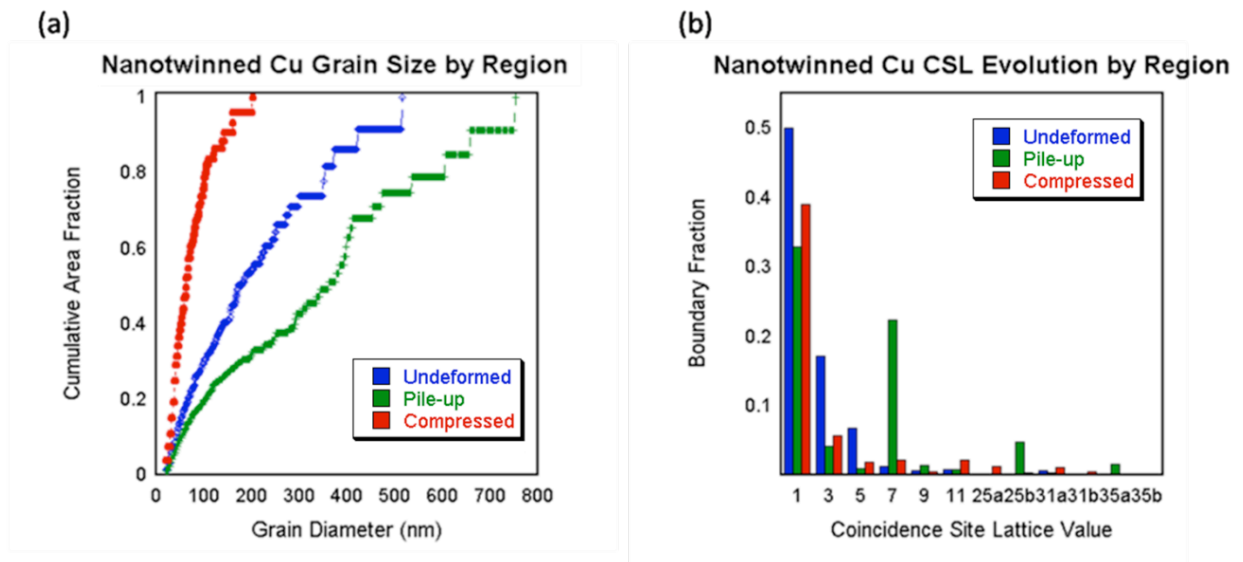


**Figure 4.4.** Region-specific response of nanotwinned Cu to mechanical indentation at cryogenic temperatures (a) grain size evolution and (b) CSL boundary evolution

$\Sigma 5$  grain boundaries exist. These  $\Sigma 3$  boundaries are indicative of the high density of twins developed during the deposition. The  $\Sigma 5$  boundaries were observed at the substrate interface, possibly associated with the initial growth behavior of the film. Within the pile-up region, the fraction of low angle,  $\Sigma 3$ , and  $\Sigma 5$  boundaries are significantly reduced. There is, however, a strong  $\Sigma 7$  accumulation in the pile-up as compared to either of the other regions, as shown in the histogram of Figure 4b. There is also an increased fraction of  $\Sigma 25b$  within the pile-up region. These can also be seen as subgrains within some of the larger grains in Figure 3d. Within the indented region, the refinement of the grain size is a result of the compression of the grains between the tip and the hard silicon substrate. Similar grain refinement under compression loading has been reported in other systems [12]. The distinct differences in grain size and CSL boundary type within these three regions are likely influenced by the complex stress state and boundary conditions imposed during the indentation process. At the center of the indent, the stress state is dominated by compression, whereas at the flanks of the indents near the edges, more substantial shear stresses exist.

The idea of substantial, rapid grain growth at cryogenic temperatures may seem to violate traditional metallurgical notions of migration kinetics. However, recent modeling results have provided insight into the possible explanations for mechanically-induced grain growth at cryogenic temperatures. Sansoz and Dupont [13] performed molecular statics calculations of nanocrystalline Al at 0 Kelvin. The growth of the grains in their simulation was attributed to a shear-coupled boundary motion mechanism. Additionally, molecular dynamics simulations performed by Janssens *et al.* [14] were able to estimate grain boundary mobility as a function of misorientation angle. Although the exact nature of the mechanisms controlling boundary mobility is still uncertain, it is accepted that the mobility strongly depends on the

crystallographic misorientation between neighboring grains. Certain grain boundaries with a  $\Sigma 3$  type misorientation were noted to have a substantially higher mobility relative to other boundaries [14]. They reported that the near- $\Sigma 7$   $40^\circ$  [111] boundary has an anomalously high mobility [14]. Olmsted *et al.* [15] also showed that there are several different types of  $\Sigma 7$  boundaries that have very high mobilities, but not all  $\Sigma 7$  boundaries have this high mobility. Olmsted *et al.* [15] have also shown grain growth through simulations of boundary mobility and misorientation type. In their work, performed for Ni, the lowest energy boundary was found to be the coherent twin boundary  $\Sigma 3$   $60^\circ$  (111). While the coherent twin is a  $\Sigma 3$  boundary, it is important to note that there are forty-one types of  $\Sigma 3$  boundaries, which all have the same misorientation between the grains, but possess different inclination planes and therefore possess a range of mobility values. The Ni  $\Sigma 3$  boundaries had a range of energies from  $0.06 \text{ J/m}^2$  (coherent twin) to  $1.0 \text{ J/m}^2$  [15]. Grain boundary energy, as noted previously, can provide a significant driving force for grain coarsening and contribute to which grains coarsen at a faster rate than their neighbors.

Table 1 shows the number fraction of the coherent twin boundary,  $\Sigma 3$   $60^\circ$  (111), in both the undeformed and the indented samples. In the undeformed material, it can be seen that of the 40,812 boundaries analyzed, 4.9% of them were classified as coherent twin boundaries. After cryogenic indentation, this fraction was reduced to only 0.4% coherent twin boundaries, an order of magnitude difference. The significant reduction of twins suggests that a plausible mechanism of the grain coarsening was detwinning within the film under the indent, as described by Wang *et al.* [16].

Field *et al.* [17] reported that grain growth is heavily dependent upon the twinning processes at low temperatures. The twinned structure generally alters the energy and the

mobility of a mobile interface. It has been shown that the slowest growing grains obtain the highest fraction of twin boundaries, as the new twin orientations presumably increase the boundary energy at positions where there is insufficient driving force to continue growth [16]. The presence of the twins intersecting a grain boundary suppresses the mobility of that boundary, which can facilitate the primary recrystallization process. When the grain boundary migration rate is high, few twins generally develop, while when the growth rate is low, more twins are found within the material. The lack of twins in the pile-up, though presumably present prior to deformation based on the undeformed analysis, suggest that these grains grew quickly, as described by Field *et al.* [16]. Hence, the lack of twins is a result of a detwinning process accomplished by the collective glide of multiple twinning dislocations that form an incoherent twin boundary. Moreover, Wang *et al.* [17] showed that detwinning can easily occur for thin films, and the driving force for such mechanisms is attributed to variations in the excess energy of coherent twin boundaries [17], as experimentally quantified to exist in the film's of this letter. These results imply that the high density of twins and their subsequent detwinning can be a dominant deformation mechanism and result in grain coarsening and the abnormal growth seen in the pile-up region.

To date, this research has investigated the pre- and post- cryogenic indentation microstructure using TEM characterization. The results have shown there is AGG that occurs in the pile-up region while there is a depletion of twin boundaries in this region. What is not yet known is if this grain growth actually occurs *during* the indention or upon heating back to ambient temperature after indentation. This same question can also be raised regarding the previous research performed by Zhang *et al.* [6]. To answer this existing uncertainty, we are currently performing an *in situ* cryogenic indentation experiment.

## 4.6 Conclusion

Nanocrystalline Cu thin films were deposited via PLD onto polished Si substrates, developing a columnar grain morphology with a high density of twins. The film was subjected to 0.5 N indentation at 77K. Subsequent quantification using precession enhanced electron diffraction determined the grain texture and grain-to-grain misorientation. Three regions were identified: (i) undeformed which preserved the as-deposited microstructure (ii) pile-up and (iii) refined grains under the indent. The grains within the undeformed film retained a high density of  $\Sigma 3$  boundary twins whereas the pile-up region showed significant grain coarsening, prevalent  $\Sigma 7$  subgrain orientations and an order of magnitude decrease in  $\Sigma 3$  twin boundaries. Coupling these experimental results with prior simulations [16,17] suggests that detwinning is likely the contributing mechanism that allowed the grains to coarsen at significantly low homologous temperature, where diffusion based mobility would be inactive.

## 4.7 Acknowledgements

This work was supported by the US Department of Energy, Office of Basic Energy Sciences. JGB and GBT received additional supplementary support from NSF-EPS-0814103. The authors acknowledge Dr. Khalid Hattar for performing the pulsed laser depositions and Dr. Eric Homer for useful discussions on CSL boundaries. FIB access was provided by DOE's Center for Integrated NanoTechnology (CINT). Sandia is a multiprogram laboratory operated by Sandia Corporation, a Lockheed Martin Company, for the United States Department of Energy's National Nuclear Security Administration under contract DE-AC04-94AL85000.

## 4.8 References

1. G. Gottstein, L.S. Shvindlerman, "Grain Boundary Migration in Metals: Thermodynamics, Kinetics, Applications." CRC Press, Boca Raton, 1999.
2. C.M. Hefferan., S.F. Li, J. Lind, U. Lienert, A.D. Rollett, R.M. Suter, Mater. Sci. Forum. 715 (2012) 447.
3. D.S. Gianola, D.H. Warner, J.F. Molinari, K.J. Hemker, Scr. Mater. 55 (2006) 649.
4. B.L. Boyce, H.A. Padilla, Metall. Mater. Trans. A. 42A (2011) 1793.
5. H.W. Hoppel, Z.M. Zhou, H. Mughrabi, R.Z. Valiev, Phil. Mag, 82 (2002) 1781.
6. K. Zhang,, J.R. Weertman, J.A. Eastman, Appl. Phys. Lett. 87 (2005) 6192.
7. J.M.E. Harper, C. Cabral, P.C. Andricacos, L. Gignac, I.C. Noyan, K.P. Rodbell, C.K. Hu, J. Appl. Phys. 86 (1999) 2516.
8. J.A. Knapp, D.M. Follstaedt, S.M. Myers, J. Appl. Phys. 79 (1998) 1116.
9. L.A. Giannuzzi, F.A. Stevie. "Introduction to Focused Ion Beams." Springer, New York, 2005.
10. A. Avilov, K. Kuligin, S. Nicolopoulos, M. Nickolskiy, K. Boulahya, J. Portillo, G. Lepeshov, B. Sobolev, J.P. Collette, N. Martin, A.C. Robbins, P. Fischione. Ultramicroscopy 107 (2007) 431.
11. D. Brandon, Acta Metall. 14 (1966) 1479.
12. W. Blum, Y.J. Li, K. Durst, Acta Mater. 57 (2009) 5207.
13. F. Sansoz, V. Dupont, Appl. Phys. Lett. 89 (2006) 111901.
14. K.G.F. Janssens, D.L. Olmsted, E.A. Holm, S.M. Foiles, S.J. Plimpton, P.M. Derlet. Nat. Mater. 5 (2006) 124.
15. D.L. Olmsted, S.M. Foiles, E.A. Holm, Acta Mater. 57 (2009) 3704.
16. J. Wang,, N. Li, O. Anderoglu, X. Zhang, A. Misra, J.Y. Huang, J.P. Hirth. Acta Mater. 6 (2010) 2262.
17. D.P. Field, L.T. Bradford, M.M. Nowell, T.M. Lillo, Acta Mater. 55 (2007) 4233-4241.

## CHAPTER 5

### THE ROLE OF TWIN BOUNDARIES IN GRAIN GROWTH

Submitted for Publication in *Advanced Functional Materials*

#### The Role of Copper Twin Boundaries in Cryogenic Indentation-Induced Grain Growth

J.G. Brons<sup>1</sup>, H.A. Padilla II<sup>2</sup>, K. Hattar<sup>2</sup>, G.B. Thompson<sup>1</sup>, B.L. Boyce<sup>2</sup>

<sup>1</sup>The University of Alabama, Department of Metallurgical Engineering, Tuscaloosa, AL 35405

<sup>2</sup>Sandia National Laboratories, Albuquerque, NM

#### 5.1 Abstract

Nanostructured Cu films with and without a high density of twin boundaries in the  $\langle 100 \rangle$  orientation were indented at approximately 77 K with a load of 0.5 N. Utilizing precession-enhanced electron diffraction in the transmission electron microscope, the crystallographic texture, grain size, and grain-to-grain misorientation were quantified. Unlike previously analyzed nanotwinned  $\langle 111 \rangle$  Cu, which underwent grain growth in the pile-up region of the indent with a substantial increase in the  $\Sigma 7$  boundary fraction, the nanotwinned  $\langle 100 \rangle$  Cu underwent grain growth with marked increases in the  $\Sigma 3$  and  $\Sigma 5$  boundary fractions. The untwinned Cu film without twin boundaries experienced little to no statistically observed grain growth. The twinned grain structure seems to facilitate the observed grain growth, either as a

result of the increased mobility of the twin boundaries and/or a complex mechanically-induced detwinning mechanism.

## 5.2 Introduction

The high density of grain boundaries present in nanocrystalline metals can result in grain instability because of their inherent driving forces [1]. Grain growth occurs by the motion of grain boundaries, the velocity of which is represented by the product of a driving force and a boundary mobility. Since mobility is often dependent on atomic diffusion, temperatures of approximately one-half or higher of the melting temperature are usually required to observe substantial grain growth [2]. However, it has been reported that nanocrystalline grains have grown spontaneously in a matter of days while held at room temperature [3-5]. Additionally, for temperatures well below half of the melting temperature, it has been shown in a number of investigations [5-12] that mechanical loading can accelerate grain growth in nanocrystalline metals. Specifically, the work by Zhang *et al.* [1, 7] presented transmission electron microscopy (TEM) studies in which grain growth at room temperature occurred via indentation. In their reports, the starting grain size was approximately 40 nm, and after indentation, certain grains achieved sizes of nearly 300 nm. Even more surprising was a series of cryogenic indentations at 77 K where the grains grew up to 700 nm [1]. At temperatures of several hundred degrees Kelvin, typical boundary velocities for Cu are on the order of  $10^{-9}$  m/s [13], and at 77 K, one might expect grain boundary migration to occur only on geological time scales. The ability for grains to grow under cryogenic conditions is not well understood.

Molecular dynamics (MD) simulations have provided some insight into the role of nanocrystalline grain boundary structure and motion under deformation [14-16]. Gianola *et al.*

[9] investigated grain growth in nanocrystalline Al and showed that discontinuous grain growth leads to the production of larger grains. The grain growth driving force was attributed to the applied stress and not to inherent sources such as the grain boundary curvature. Tucker and Foiles [17] recently reported MD simulations to study the rate-dependency of grain growth in nanocrystalline Ni due to surface indentation at room temperature. Post-processing algorithms identified individual grains and tracked the evolution of fundamental deformation mechanisms. Differences in the growth of the grains and the strain accommodation were correlated to differences in dislocation and twinning processes. Grains underwent refinement during the initial stages of indentation because of deformation accompanying dislocation nucleation/migration, twinning, and grain boundary plasticity [17]. As indentation continued, some grains near the indenter preferentially grew at the expense of smaller grains, while grains far from the indenter remain unaffected. This simulation did not indicate whether the grain growth is preferred in grains with particular grain boundary structures or if high or low-angle grain boundaries migrate more efficiently during indentation.

Zhang *et al.* [1] presented that the rate of grain growth and the hardness both increased when the deformation temperature was reduced to 77 K, an observation that was interpreted to indicate that growth was likely stress-induced and not thermally activated. In a paper recently published by the authors [12], a nanocrystalline  $\langle 111 \rangle$  Cu thin film with a high density of as-deposited twin boundaries was indented while submerged in liquid nitrogen. After post-processing, the grains were found to undergo substantial grain growth in the ‘pile-up’ region of the indent, while the region at the center of the indent impression underwent grain refinement. Subsequent quantification using transmission electron microscopy-based precession-enhanced electron diffraction (PED) determined the crystallographic texture and grain-to-grain

misorientation. The grains within the undeformed region of the film retained a high density of  $\Sigma 3$ -type twin boundaries, whereas the pile-up region showed significant grain coarsening, prevalent  $\Sigma 7$  subgrain formations and an order of magnitude decrease in  $\Sigma 3$  twin boundaries [12]. Coupling these experimental results with prior simulations, it was suggested that detwinning is likely the contributing mechanism that allowed the grains to coarsen as a result of significantly low homologous temperatures, where diffusion based mobility would be inactive.

It is commonly accepted that the grain boundaries within a polycrystalline material differ in their structure, and in turn, their physical properties. Specifically, populations of grain boundaries are categorized into several sets of sub-populations, with special boundaries being one of the most extensively used categories [18]. Twin boundaries form one of the subsets of special boundaries in face-centered cubic (FCC) metals [18]. They are distinguished by low surface energy and mobility variations (low mobility for coherent twin boundaries and high mobility for non-coherent twin boundaries), special misorientations, and a flat, step-like, geometry with sharp dihedral angles [18]. Despite the fact that twin boundaries are frequently observed in materials of technological importance, their geometry and effect on grain growth and related properties in polycrystals is still a matter of debate [18]. It has been suggested that they have a negligible effect on the flow stress [19], but this conclusion has been challenged [20]. Recently, there have been studies conducted on the properties of twin boundaries and their role in the mechanisms that take place during the deformation of polycrystalline materials [18, 21-23]. MD simulations have shown that twin boundaries can act as dislocation sources facilitating dislocation activity [24] as well as dislocation sinks [25].

Twin boundaries are not the only subset of special boundaries that may be contributing to grain growth. Coincidence site lattice (CSL) boundaries have been the focus of numerous

studies [26-29]. Historically, the energy of a grain boundary was interpreted in terms of its  $S$  value, where a small value of  $S$  (high density of coincident boundary sites) suggests the lattices mesh well together, leading to lower boundary energy, however this pre-existing notion is currently under some scrutiny from researchers [27, 30]. It is unclear if these boundaries contribute to the grain growth behavior in metals.

To determine the role that twin play in cryogenic indentation induced grain growth of nanostructured Cu thin films, a series of nanostructured Cu films with and without a high density of twins was studied. For the twins, the orientation of the film texture was compared between  $\langle 100 \rangle$  and  $\langle 111 \rangle$ , which would ideally modify the resolved shear stress from the indent on the twin plane. The results of these experiments are compared, and the role of the grain structure is investigated. The character of grain boundaries was examined by utilizing the ASTAR platform, which provides the possibility of reliable orientation/phase mapping with a spatial resolution as low as 3 nm [31].

### 5.3 Experimental

As previously reported by the authors [12], Cu films approximately 500 nm thick were grown via a pulsed laser deposition (PLD) process onto polished silicon substrates. To form the twinned structure, the films were deposited at room temperature with a base pressure of  $4.7 \times 10^{-7}$  Torr. After deposition, in all three cases, the films had adopted a columnar-type grain morphology normal to the substrate surface with a high density of twin boundaries either horizontally or inclined to the substrate surface. This type of grain structure has been identified as ‘nanotwinned’ [12] and will continue to be referred to as such in this paper. Depending on the line-of-sight of the deposition target to the substrate, and thus the plum energy on impact, the

film exhibited two different textures; the center region was  $\langle 111 \rangle$  and the outer perimeter was  $\langle 100 \rangle$ , Figure 1(a) and 1(b). The pole figures from the orientation analysis were collected on a Bruker D8 with GADDS diffractometer. For this work, these two textures will be considered as two different cases, a  $\langle 100 \rangle$  nanotwinned and a  $\langle 111 \rangle$  nanotwinned.

To determine the role of twin boundaries in grain growth, a nanostructured film was grown with little-to-no twin formation in the grains. This  $\sim 750$  nm thick film was deposited via PLD onto a polished silicon substrate at an initial temperature of 117 K and a base pressure of  $5.3 \times 10^{-7}$  Torr. The resulting grains were columnar, without twin boundaries. This type of grain structure is described as ‘untwinned’ throughout the rest of this paper.

The indentation of the nanotwinned and the untwinned Cu films was carried out using a custom-built immersion indenter, affixed with a modified Vickers indenter tip. To make the indents in this experiment comparable to the indent in the previous experiment [12], a 0.5 N normal force was implemented, and the sample was submerged in liquid nitrogen during indentation. The indenter tip was lowered at a rate of approximately 0.08 mm/s, until the indenter tip contacted the sample surface and was then held for 60 seconds. Details of the experimental instrumentation can be found in reference [12].

TEM cross-sectional foils containing the undeformed and the indented regions of the films were prepared at room temperature using a FEI Quanta 3D dual beam focused ion beam (FIB) equipped with an *in-situ* Omniprobe lift out micromanipulator according to a predefined lift-out procedure [32]. During the final milling steps, the acceleration voltage was reduced from 30 to 5 keV to reduce surface milling damage [33]. After the foil was attached to a TEM grid, the specimen was further cleaned using a Gatan Precision Ion Polishing System (PIPS) operating at 2.5keV, 1.0 mA, and an inclination angle of 8 degrees. This last step was found to

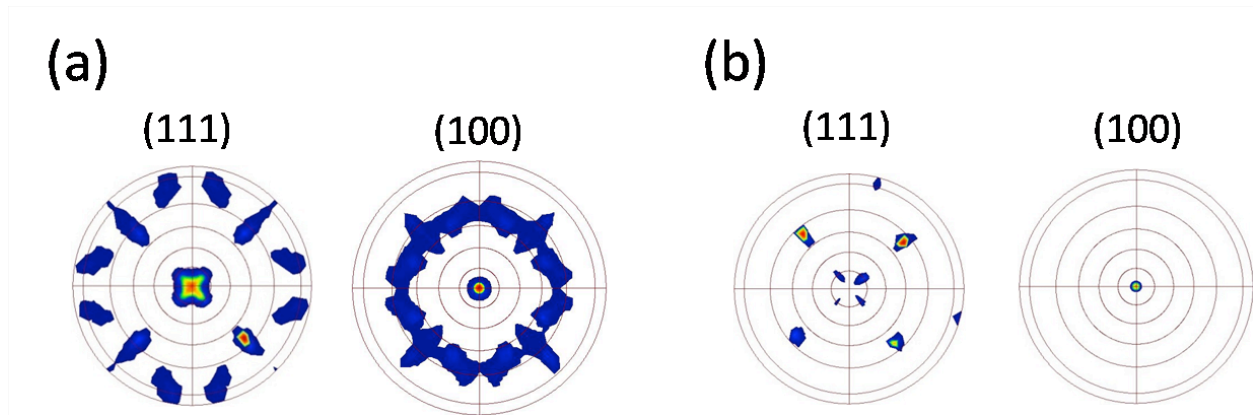


**Figure 5.1.** X-ray diffraction pole figures from the nanotwinned Cu film **a)**  $\langle 111 \rangle$  texture **b)**  $\langle 100 \rangle$  texture

significantly improve foil quality by removing any residual FIB damage, yielding crisp brightfield images and precession enhanced diffraction patterns [12]. Comparing the indented region to the non-indented region in the same foil provided confidence that the specimen preparation did not produce artifacts in the data analysis and interpretation.

The TEM foils were then analyzed in an FEI Tecnai F20 Supertwin TEM operating at an accelerating voltage of 200 kV and fitted with a NanoMEGAS© ASTAR PED orientation identification platform [34]. The ASTAR platform generates pseudo-kinematical electron diffraction conditions, which allows grain orientation to be measured. This facilitates the collection and analysis of not only grain size but also the misorientation distributions. The precession angle used for the analysis was 1 degree at step sizes of 10 nm.

After collecting the PED data, the orientation of the diffraction pattern collected at each point was identified and was mapped using the nanoMEGAS software. In order to provide detailed grain size and texture analysis, the orientation information was converted and exported for optimization through the OIM Analysis 5 software platform. The conservative data processing parameters chosen in this study were a grain tolerance angle of 5 degrees and a minimum grain size of 20 nm, as well as a neighbor confidence interval correlations with a confidence interval of 0.05.

## **5.4 Results**

The cross-sectional inverse pole figure orientation map of the undeformed region of the nanotwinned Cu film with the  $\langle 100 \rangle$  texture is presented in Figure 2(a). The grains were generally columnar in nature with smaller grains found at the substrate surface, where the deposition process initiated. These smaller grains were separated by low angle and  $\Sigma 5$

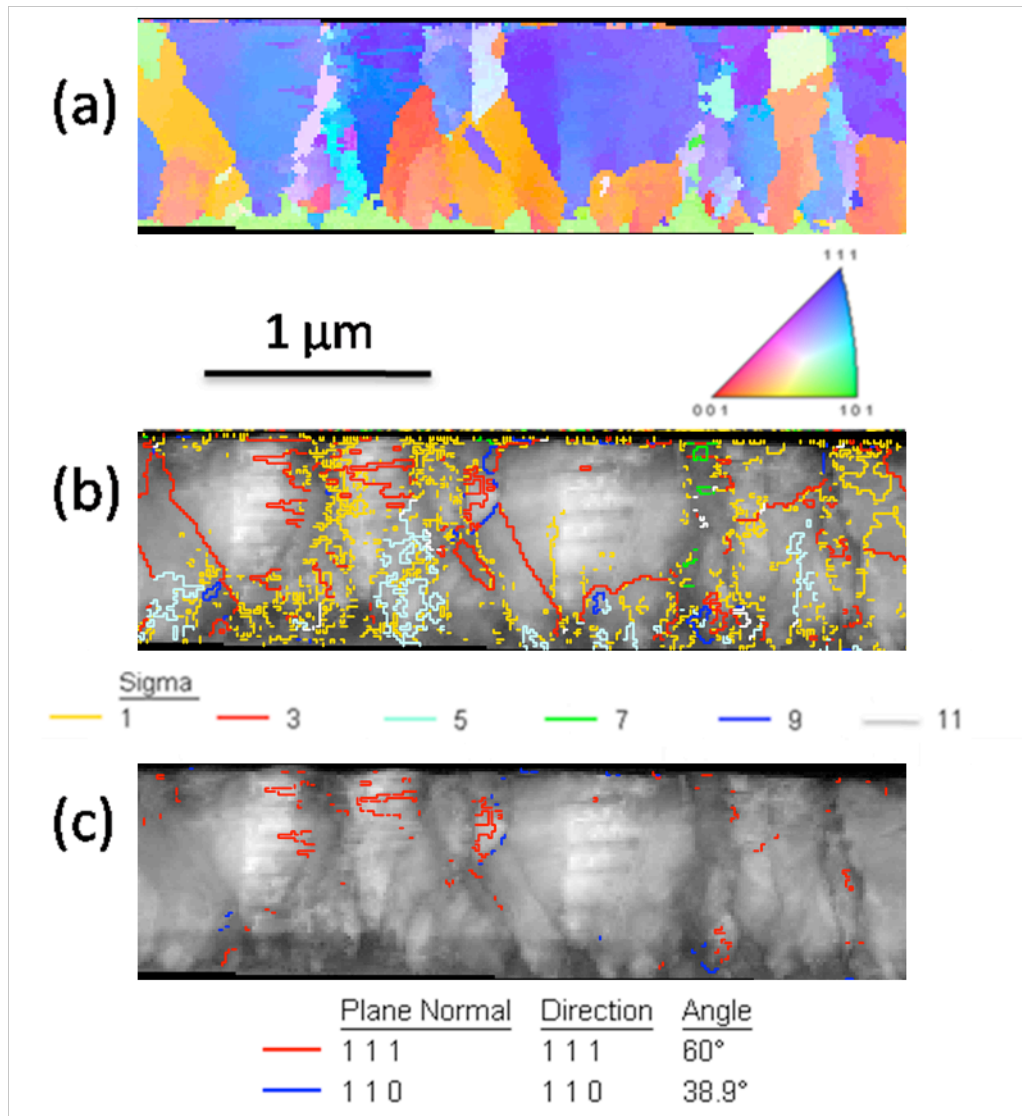


**Figure 5.2.** Undeformed nanotwinned  $\langle 100 \rangle$  Cu film in cross-section **a)** inverse pole figure orientation map **b)** image quality map with CSL boundaries overlaid **c)** image quality map with twin boundaries overlaid

boundaries, as is shown in Figure 2(b), determined using Brandon's criterion [35]. The grayscale in Figure 2(b) represents an image quality map of the scanned region with specific low- $\Sigma$  CSL boundaries overlaid in color. Additionally, in Figure 2(c), is an image quality map with the twin boundaries overlaid. While there were twins found in the undeformed grains, the density of these twins is qualitatively not as high as the previously studied  $\langle 111 \rangle$  nanotwinned Cu film [12].

Next, the cross-sectional inverse pole figure orientation map of the undeformed region of the untwinned Cu film is presented in Figure 3(a). Once again, the majority of the grains shown were columnar in nature. The PLD process employed, whether executed at room temperature or onto a substrate cooled to 117 K, allowed for the Cu to first form seed grains along the substrate surface separated by low angle boundaries before it evolves into the columnar structure. In this untwinned case, there appears to be a higher density of low angle boundaries at the substrate surface as compared to the nanotwinned films. Figure 3(b) presents an image quality map of the undeformed region with the CSL boundaries, again calculated in accordance with Brandon's criterion [35], overlaid. As the untwinned Cu film progressed upwards from the initial growth stage, the columnar grains were separated by  $\Sigma 1$  boundaries,  $\Sigma 3$  boundaries, and  $\Sigma 7$  boundaries, as opposed to the nanotwinned Cu in Figure 2(b), which qualitatively showed a higher prevalence of  $\Sigma 5$  boundaries. This difference in the initial growth stage is attributed to the substrate being cooled to 77 K in the untwinned case. In addition to the initial growth stage orientation differences, the deposition temperature prevented twin formations in the columnar grains [12].

After cryogenic indentation and sample preparation were performed, the Cu specimens had three distinct regions, as shown in the representative micrograph in Figure 4(a). The three

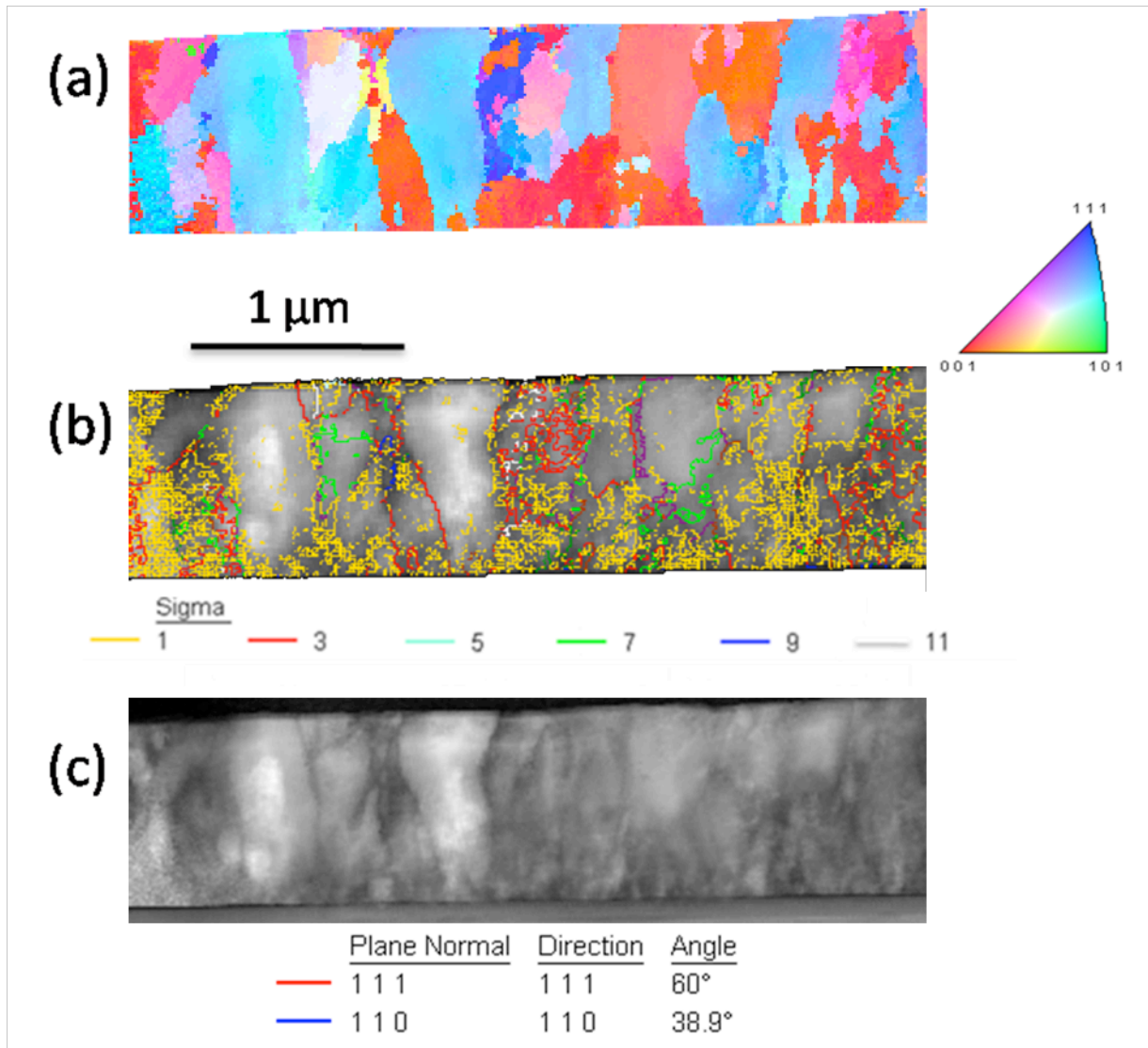


**Figure 5.3.** Undeformed untwinned Cu film in cross-section **a)** inverse pole figure orientation map **b)** image quality map with CSL boundaries overlaid **c)** image quality map with twin boundaries overlaid

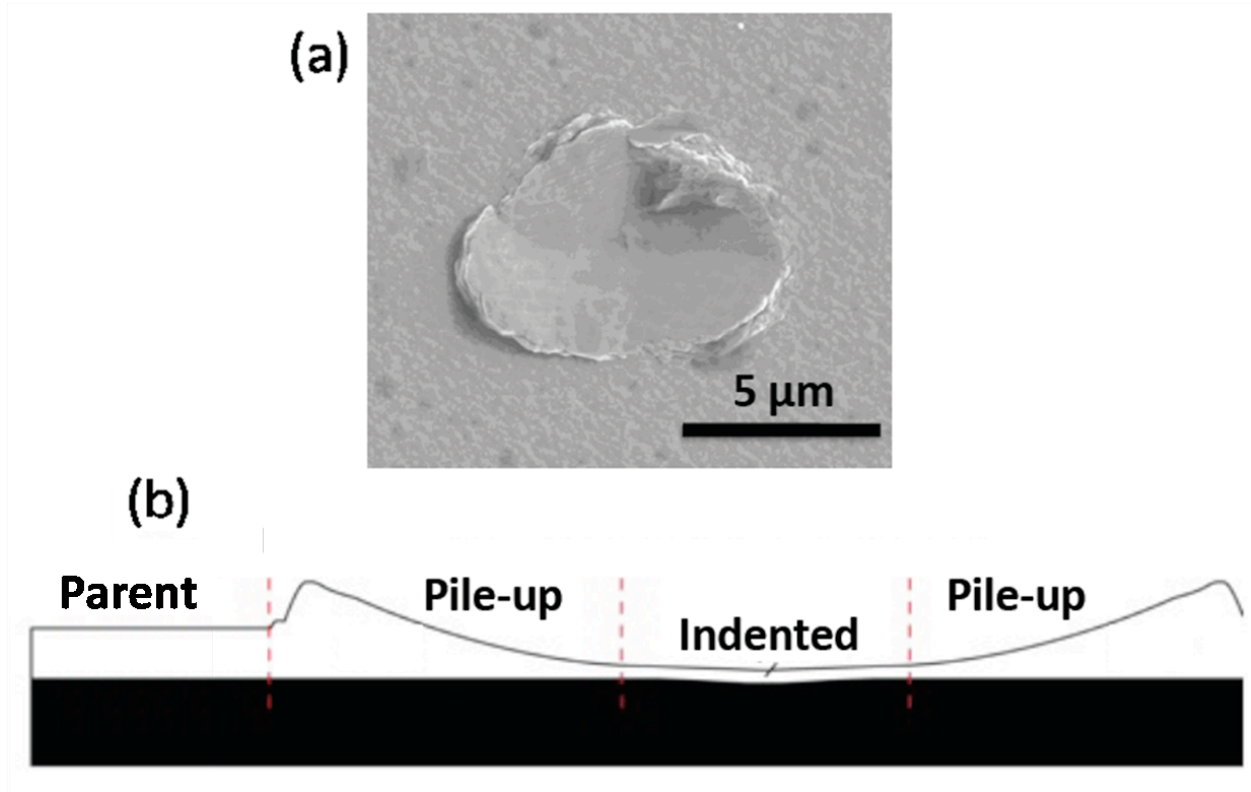


**Figure 5.4.** Representative indent after cryogenic indentation **a)** SEM micrograph **b)** graphical cross-section of the indent

regions are designated as ‘parent’, ‘pile-up’, and ‘indented’ graphically represented in Figure 4(b). PED orientation scans were completed for both the  $\langle 100 \rangle$  nanotwinned and the untwinned Cu specimens in a manner previously reported for the  $\langle 111 \rangle$  in reference [12]. The inverse pole figure orientation map of the  $\langle 100 \rangle$  nanotwinned foil is presented in Figure 5(a). Each of the three regions of the indent possessed a distinct grain structure. Within the pile-up region of the indent, there were several grains that grew to a size much larger than the parent state. In Figure 5(b), an image quality map of the scan is presented with the CSL boundaries overlaid. The large grains were bounded by  $\Sigma 3$  and  $\Sigma 9$  boundary types. There were very few low angle boundaries and few  $\Sigma 5$  boundaries in the pile-up region, although they were both populous in the parent region. In Figure 5(c), the twin boundaries are outlined over the image quality map, with a prevalence of these boundaries located in the large grains.

In the orientation map presented in Figure 6(a), the deformation-induced grain and twin morphology of the untwinned Cu is vastly different than that previously observed in the nanotwinned Cu films, Figure 5 and reference [12]. There was clear grain deformation in the pile-up region and grain refinement under the indent. The CSL boundaries overlaid on the image quality map in Figure 6(b) shows that there was a high density of low angle boundaries in the pile-up and indented regions of the untwinned film. Qualitatively, these low angle boundaries appear to be more populous in the pile-up region than they were initially in the parent of the untwinned foil. This is opposite of what was observed in the  $\langle 100 \rangle$  nanotwinned specimen and the previous  $\langle 111 \rangle$  nanotwinned Cu [12], with these films showing significant grain growth in the pile-up.

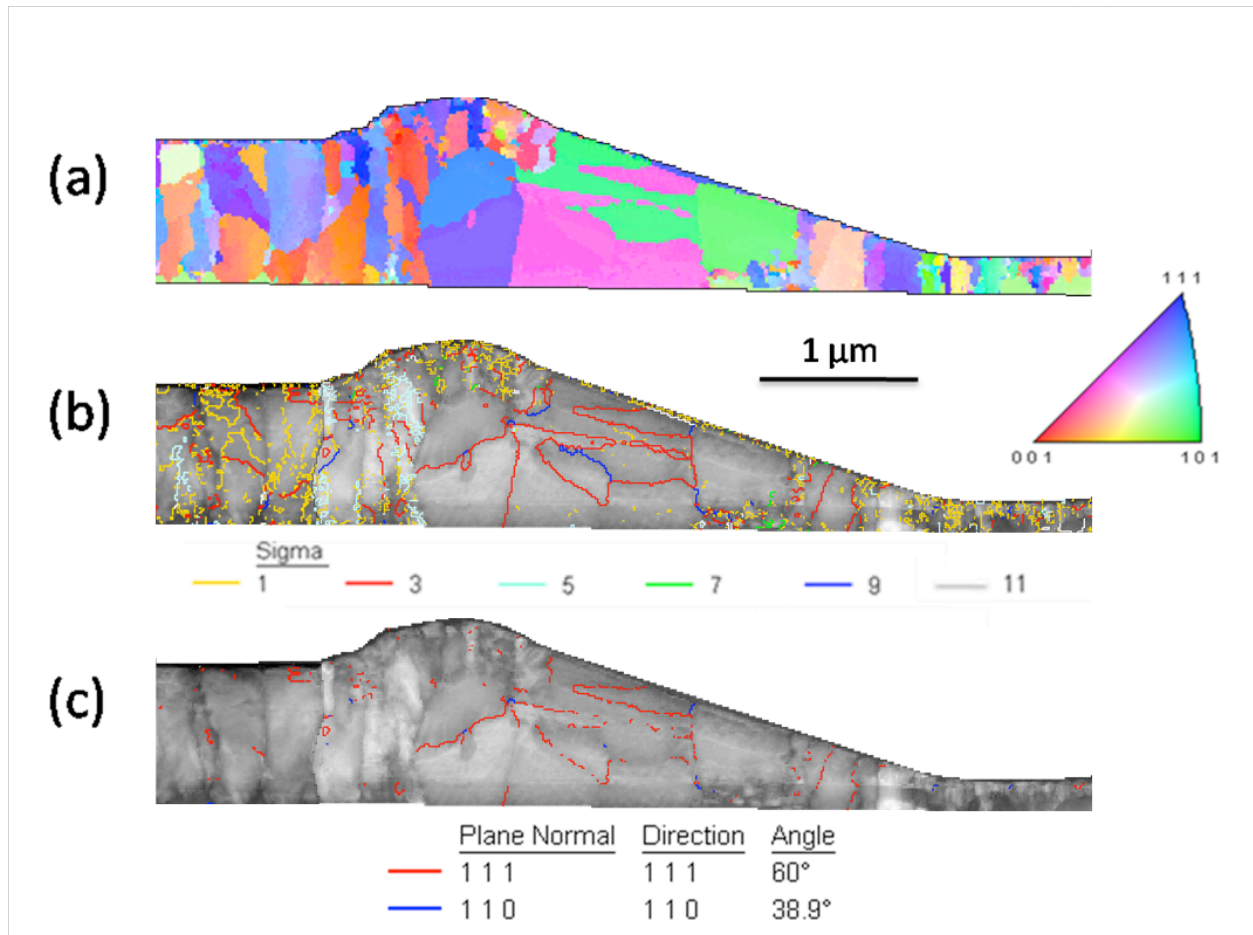


**Figure 5.5** Indented nanotwinned <100> Cu film in cross-section **a)** inverse pole figure orientation map **b)** image quality map with CSL boundaries overlaid **c)** image quality map with twin boundaries overlaid

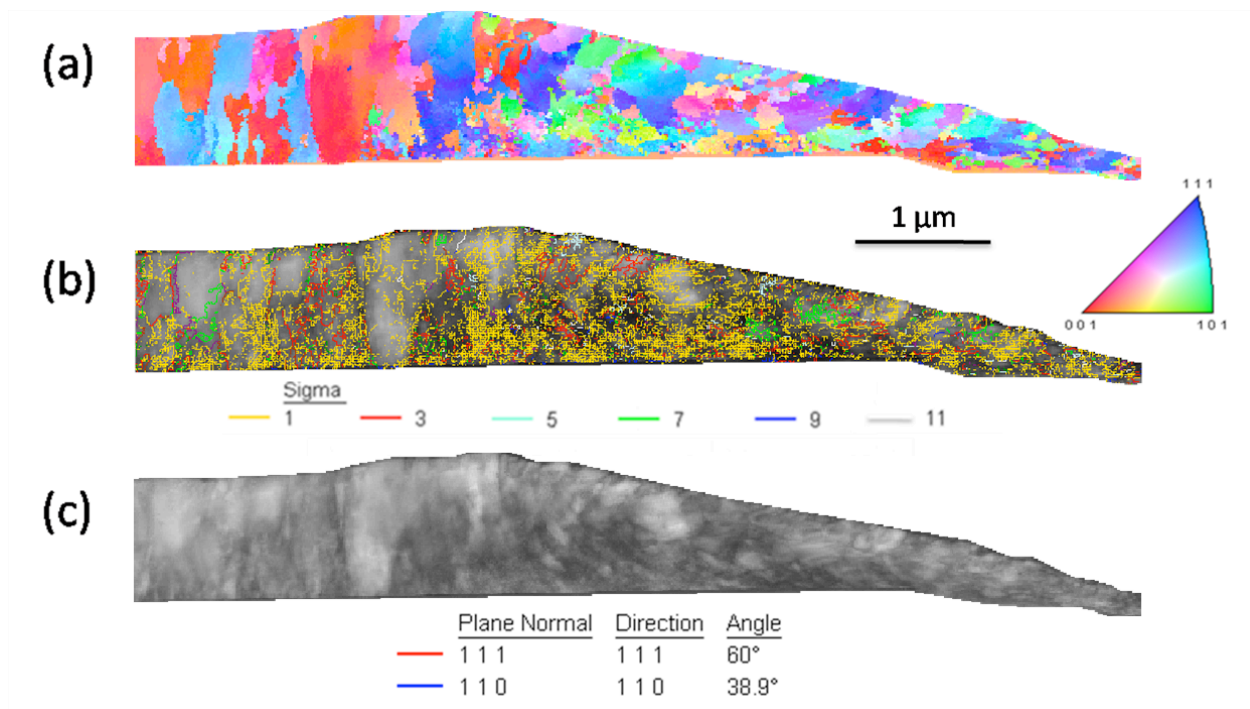


**Figure 5.6.** Indented untwinned Cu film in cross-section **a)** inverse pole figure orientation map **b)** image quality map with CSL boundaries overlaid **c)** image quality map with twin boundaries overlaid

## 5.5 Discussion

The nature of the original grain structure, governed by the deposition, plays a significant role in the grain growth behavior of these Cu thin films. Since the goal of this research was to determine the role of twin boundaries in the deformation behavior of Cu films being indented at 77 K, being able to identify the grain size, the grain-to-grain misorientation, and the twin boundary content before and after deformation was critical in understanding the role of twin boundaries on the deformation mechanisms. By using the conservative optimization parameters outlined above, there was a chance that some of the smallest grains and some of the identified low angle boundaries were artifacts of the automated data analysis process. The authors chose to keep these conservative parameters, however, so that the data presented was most representative of the films, and not manufactured by post-processing. As the PED technique continues to mature, better optimization processes may become available, but the authors have utilized state-of-the-art software platforms to improve the fidelity of the data.

When twin boundaries are present in the undeformed structure (whether they be  $\langle 100 \rangle$  or  $\langle 111 \rangle$ ), cryogenic indentation leads to grain growth in the pile-up region. When the twin boundaries are not present, there seems to be grain refinement in the pile-up region. The simplest way to quantitatively depict this difference is by plotting the cumulative grain size distributions for the parent, pile-up, and the indented regions found in the untwinned, the  $\langle 100 \rangle$  nanotwinned, and the  $\langle 111 \rangle$  nanotwinned shown in Figure 7(a-c), respectively. To generate these plots, each grain was binned separately, and the cumulative area fraction was presented. Based on Figure 7(a), all three of the films had similar grain size distributions. Additionally, in Figure 7(c), the grain refinement observed within the indented region was similar for all three

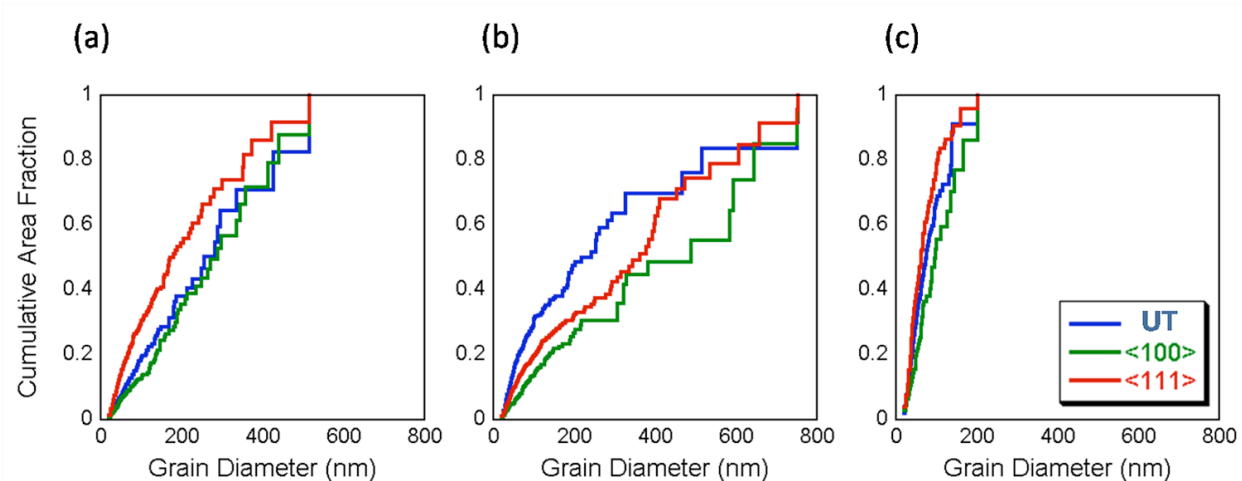


**Figure 5.7.** Cumulative grain size plots for the **a)** parent region **b)** pile-up region **c)** indented region. The <111> data is from reference [12]. UT refers to the nanostructured metal (without twins), whereas <100> and <111> refer to the two nanotwinned materials.

films. They each contained grains that all measured less than 250 nm in diameter and exhibited a monomodal distribution.

The region in which the main differences between the three films is found in the pile-up on either side of the indent, Figure 7(b). The untwinned film underwent grain refinement, with more than 75% of the grains (by area) having diameters less than 300 nm. Originally, approximately 60% of the grains in the parent material of the untwinned film had a diameter less than 300 nm. There were a few outlier grains with a relatively larger size. Upon reviewing Figure 6, these larger grains are located at or near the border separating the parent and pile up regions, which is not a clear distinct cut-off. Hence, these larger grains may be artifacts of residual grains from the parent material that did not experience significant evolution under deformation.

In the previously studied  $\langle 111 \rangle$  nanotwinned Cu [12], more than 80% of the grains (by area) had a diameter less than 400 nm. In the pile-up region, only 50% of the grains (by area) had a grain diameter less than 400 nm. There was considerable grain growth observed, with approximately 20% of the grains (by area) having a diameter larger than 600 nm. Finally, in the  $\langle 100 \rangle$  nanotwinned Cu examined in this paper, there was also considerable grain growth observed in the pile-up region. Initially, in the parent region, 75% of the grains (by area) had a diameter less than 400 nm. After indentation, in the pile-up region, 45% of the grains (by area) had a grain size larger than 600 nm. The ledges within the cumulative distribution plots are representative of grains that evolved as a result of mechanical load on the film.

In an effort to understand how special grain boundaries play a role in this difference in grain growth, the CSL boundary fractions for the parent, pile-up, and indented regions of the untwinned, the  $\langle 100 \rangle$  nanotwinned, and the  $\langle 111 \rangle$  nanotwinned Cu were examined, and they

are presented in Figure 8(a-c), respectively. In the parent region, Figure 8(a), the films had similar distributions of CSL boundaries. There was a high fraction of low angle boundaries and a fraction of  $\Sigma 3$  boundaries between 10 and 20% for all three of the deposited Cu films. Both of the nanotwinned films contained  $\Sigma 5$  boundaries, and the untwinned specimen contained a small fraction of  $\Sigma 7$  boundaries. In the region under the indent, Figure 8(c), the three films again have very similar special boundary distributions. The low angle boundary fractions have decreased slightly for the untwinned and  $\langle 111 \rangle$  nanotwinned films. Interestingly, the low angle boundary fraction for the  $\langle 100 \rangle$  nanotwinned film stayed approximately equivalent. In this indented region, the  $\Sigma 3$  boundary fraction for all three films decreased to less than 10%, and the  $\Sigma 5$  and  $\Sigma 7$  fractions decreased as well.

The pile-up regions of the indents show drastic differences in the boundary character between the three films, Figure 8(b). The untwinned specimen experienced almost no change in low angle boundary fraction, but the fraction of the  $\Sigma 3$  and  $\Sigma 7$  boundaries decreased significantly. In the foil containing the  $\langle 100 \rangle$  twin boundaries, the low angle boundary fraction decreased from the initial value of almost 40% to approximately 20% by boundary length. As a result of the grain growth in the pile-up region and the coupled decrease in low angle boundary fraction, there is a sharp *increase* in the  $\Sigma 3$  boundary fraction and an increase in the  $\Sigma 5$  boundary fraction. This is the only specimen that experienced growth in these two boundary types. The  $\langle 111 \rangle$  nanotwinned specimen and the untwinned Cu, however, both experienced a *loss* of  $\Sigma 3$  boundaries and almost a complete loss of  $\Sigma 5$  boundaries. The  $\langle 111 \rangle$  nanotwinned specimen did, however, experience an increase in the fraction of  $\Sigma 7$  boundaries. Initially, the fraction of  $\Sigma 7$  boundaries was less than 2%, but in the pile-up region of the indent, this fraction increased to over 20% [12]. This increase in the  $\Sigma 7$  boundary fraction is attributed to the formation of the

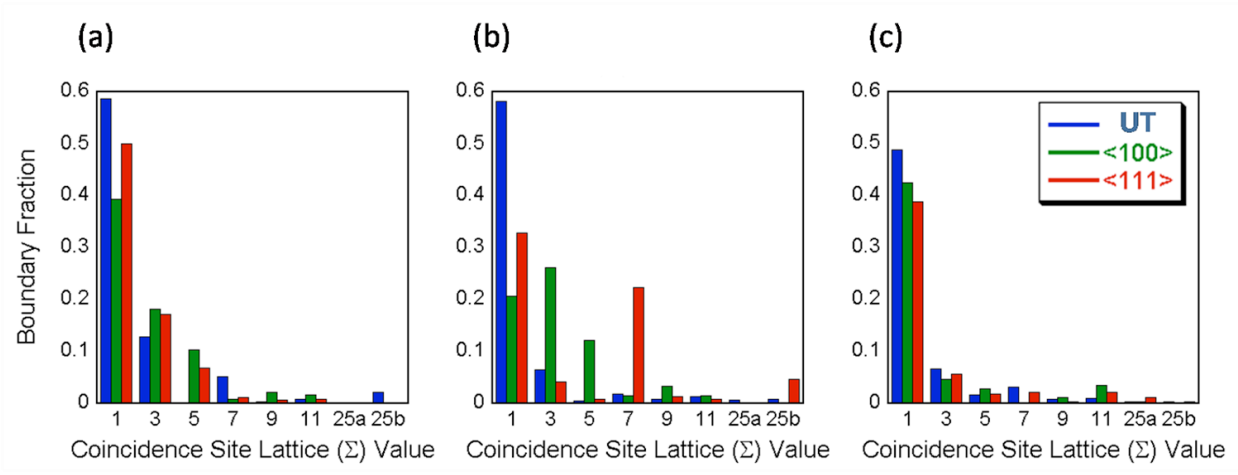


**Figure 5.8.** CSL boundary fractions for the **a)** parent region **b)** pile-up region **c)** indented region. The  $\langle 111 \rangle$  data is from reference [12].

subgrains observed between the large  $\Sigma 3$  boundaries [12]. This subgrain formation is not entirely unanticipated because it is reasonable to assume that a polycrystal should be able to reduce the excess energy stored in the grain boundaries by reducing the grain boundary area as well as by grain boundary rotation [36]. The growth of these subgrains, by subgrain coalescence, was first reported by Hu [37]. Two neighboring subgrains coalesce by the elimination of the common low-angle grain boundary between them and become one larger, elongated subgrain [36]. Knowing this, these subgrains are further attributed to the process of the grown-in twin boundaries detwinning in response to the shear force along the flank of the indenter tip.

The distinct differences in grain size and CSL boundary type within the three regions of the indents are likely influenced by the complex stress state and boundary conditions that are imposed during the indentation process. At the center of the indent, the stress state is dominated by compression, whereas at the flanks of the indents near the edges, more substantial shear stresses exist. The similarity in these regions indicates that, while the CSL boundaries do play a significant role in grain boundary movement, they may not be the only contributing factor to the difference observed.

Dynamic recrystallization in nanocrystalline metals is one possible mechanism for grain formation and growth [38, 39]. While the present study cannot definitively discount the possibility of a dynamic recrystallization process being responsible for the present observations, the very low temperature regime of the current observations appear to be more consistent with detwinning and related mechanisms for grain growth.

Sansoz and Dupont [40] performed molecular statics calculations at 0 K for nanocrystalline Al, under mechanically-induced grain growth conditions. The growth of the grains in their simulation was attributed to a shear-coupled boundary motion mechanism [41].

This model, however, seems to fall short for the experimentally observed Cu system. In the untwinned Cu, there is no observed mechanically-induced grain growth. Instead, what is observed is actually the refinement of the grains under the indent and in the pile-up regions. In contrast,  $\langle 100 \rangle$  and  $\langle 111 \rangle$  nanotwinned Cu exhibited substantial grain growth. The presence of the twin boundaries is the only discernable difference between these samples.

Wang *et al.* [42], Li *et al.* [43], and Jang *et al.* [44] showed that detwinning can occur relatively easily for thin films, and the driving force for such a mechanism is attributed to the variation in the excess energy of coherent twin boundaries [42]. From the results for the  $\langle 111 \rangle$  nanotwinned Cu foil, it can be inferred that the high density of twins, and their subsequent detwinning, can be a dominant deformation mechanism and can result in grain coarsening and grain growth. In the  $\langle 111 \rangle$  film, twin boundaries were observed in the parent material that were oriented parallel to the substrate surface at a very high density. After indentation, the addition of mechanical stress allowed for catastrophic grain growth, with the twins no longer present. The pile-up region contained large grains that contain several small grains. In the main pile-up, these small grains were separated from the large grain by  $\Sigma 7$  boundaries. The specific behavior of  $\Sigma 7$  boundaries is not as well elucidated through numerical simulations as compared to  $\Sigma 3$ ,  $\Sigma 5$ , or  $\Sigma 9$  boundaries [26, 27, 29]. From this experimental study one could infer that the  $\Sigma 7$  forms in the wake of the detwinning process.

This is not surprising, since recent research [45-48] performed on growth twins in nanostructured FCC materials has presented detwinning processes as a dominating deformation mechanism at the early stages of plastic straining. Cheng *et al.* [48] noted that dislocation arrays are often seen at the migrating twin boundary front of the receding twins and are highly active in the detwinning process. Tucker and Foiles [17] showed that grain boundary relaxation and

atomic rearrangement during indentation can result in the emission of trailing partial dislocations that can eliminate stacking faults left behind leading partial dislocations. These dislocation arrays form not only at the ends of the receding twins, but also at the sites of those dislocation walls that formed during processing. There is collective glide of the partial dislocations at both twin ends, leading to detwinning [48]. This local dislocation movement allows the twinned region to convert back to the matrix stacking by dislocation movement, and the twin boundary disappears because of dislocation emission [48]. This was assumed to be the case for the  $\langle 111 \rangle$  nanotwinned Cu.

In the  $\langle 100 \rangle$  nanotwinned Cu specimen, the density of twins is significantly lower than the  $\langle 111 \rangle$  specimen. In both films, qualitatively, the twins appear to be predominately parallel to the substrate, with a few inclined twins, Figure 2 and reference [12], however, this is only a two-dimensional view of the system. The twins may in fact be at some angle to the substrate, as it is expected that two different textures should have differently angled twin boundaries but cannot be captured in a two-dimensional TEM foil. The pile-up region where grain growth was observed is known to have the most significant shear stresses. The large grains in the pile-up region of the  $\langle 100 \rangle$  nanotwinned Cu are outlined by  $\Sigma 3$  boundaries and  $\Sigma 9$  boundaries, of which the  $\Sigma 9$  forms at the triple junction with two  $\Sigma 3$  boundaries. In Figure 8(b), there is an increase in the boundary fraction of  $\Sigma 3$  boundaries for the  $\langle 100 \rangle$  nanotwinned film as a result of deformation in the pile-up region. While not all  $\Sigma 3$  boundaries are twin boundaries, the coupling of the increased  $\Sigma 3$  fraction with the twin map in Figure 5(c) is suggestive that the twin boundaries substantially increased in length within the pile-up region. The large grains, Figure 5(a-b), in this case differ from those of the  $\langle 111 \rangle$  nanotwinned Cu film [12] since these did not contain subgrains. This difference in behavior is attributed to the twin boundaries in the  $\langle 100 \rangle$

and the  $\langle 111 \rangle$  textures responding to the applied load differently. The orientation of the twin boundaries, with respect to the indenter tip and to the substrate surface, is inherently different in these two textures. A difference in twin boundary orientation relates to a difference in the experienced resolved shear stress, which would be manifested in a difference in the observed grain growth.

The untwinned Cu film did not have any observed grown-in twin boundaries. This difference in twin content appears to have led to a difference in behavior when loaded under cryogenic conditions. The applied force from the indenter tip produced a similar shearing stress in the pile-up region. Without the twin boundaries in the parent material, the shearing stress led only to the distortion and refinement of the grains, as is presented in Figures 6(a-b). The shearing effect on the grains allowed for the evolution of many low angle grain boundaries within the pile-up region – something that was not observed in either one of the nanotwinned cases (Figure 8(b)).

Though grain growth was reported in previous nanostructured Cu films [1,7], the detailed characterization of the grain morphology was not reported. It is unclear if twins, if present, could have facilitated the reported grain growth. If twins were present, the increased mobility associated with these boundaries and possible detwinning could explain the faster growth that Zhang *et al.* [1, 7] reported. In our studies, when the twin boundary is perpendicular to the loading direction, which occurs directly under the indent tip, then detwinning is not intuitive because the resolved shear stress would be minimal. However, when the twins are inclined to the load, as is the case along the shank of the indenter tip and within the pile-up region, the appropriate shear stresses would be present and facilitate detwinning which has been previously observed [49]. To further understand how these twin boundaries contribute to the observed grain

growth in the pile-up region and to assess the orientation dependence of their behavior, *in situ* indentation would be required. In addition, such an *in situ* study would confirm if grain growth occurs at cryogenic temperature or when the film returns to ambient temperatures. These studies are currently underway.

## 5.6 Conclusion

Cu thin films were deposited via a PLD process onto polished Si substrates to produce nanostructured films with and without a high density of twin boundaries. For the twinned films, two different film orientations,  $\langle 100 \rangle$  and  $\langle 111 \rangle$ , were compared. Each film was subjected to indentation using a load of 0.5 N, so that the deformation behavior could be compared to that of a previously studied  $\langle 111 \rangle$  nanotwinned Cu [12]. Subsequent quantification, using PED, determined the grain size evolution and the grain-to-grain misorientation. Three regions were identified within the TEM foil: (i) parent, which preserved the as-deposited grain structure, (ii) pile-up and (iii) refined grains under the indent. Grain growth was observed in the pile-up region of both of the nanotwinned Cu samples where as the untwinned Cu film underwent grain distortion and refinement. It is proposed that the twin boundary mobility and a complex detwinning mechanism involving dislocation interaction at the twin front allows for shear stress-driven grain growth since only the material containing twin boundaries experienced substantial grain growth. While the two different textures both underwent grain growth, the grain boundary characters evolved in two different manners. The  $\langle 100 \rangle$  nanotwinned Cu experienced an increase in  $\Sigma 3$  boundary content and the  $\langle 111 \rangle$  nanotwinned Cu showed an increase in  $\Sigma 7$  content with subgrain formations. This distinction may be attributed to a difference in the twin boundary density between the two textures as well as a difference in texture (i.e. the inherent

differences in the angle of the twin boundaries between the <100> and the <111> films with respect to the indenter).

## 5.7 Acknowledgements

This work was supported by the US Department of Energy, Office of Basic Energy Sciences. JGB and GBT received additional supplementary support from NSF- EPS-1158862. FIB access was provided by DOE's Center for Integrated NanoTechnology (CINT). Sandia National Laboratories is a multi-program laboratory managed and operated by Sandia Corporation, a wholly owned subsidiary of Lockheed Martin Corporation, for the U.S. Department of Energy's National Nuclear Security Administration under contract DE-AC04-94AL85000.

## 5.8 References

1. S. Brandstetter, K. Zhang, A. Escudro, J.R. Weertman, H. Van Swygenhoven. *Scripta Mater.* 58 (2008) 61.
2. C.M. Hefferan, S.F. Li, J. Lind, U. Lienert, A.D. Rollett, R.M. Suter. *Mater. Sci. Forum* 715-716 (2012) 447.
3. B.S. Gunther, A. Kumpmann, H.D. Kunze, *Scripta Metall. Mater.* 27 (1992) 833.
4. K.E. Harris, V.V. Singh, A.H. King. *Acta Mater.* 46 (1998) 2623.
5. J.A. Haber, W.E. Buhro, *J. Am. Chem. Soc.* 120 (1998) 10847.
6. M. Jin, A.M. Minor, E.A. Stach, J.W. Morris Jr., *Acta Mater.* 52 (2004) 5381.
7. K. Zhang, J.R. Weertman, J.A. Eastman, *Appl. Phys. Lett.* 87 (2005) 061921.
8. D.S. Gianola, D.H. Warner, J.F. Molinari, K.R. Hemker, *Scripta Mater.* 55 (2006) 649.
9. D.S. Gianola, S. Van Petegem, M. Legros, S. Brandstetter, H. Van Swygenhoven, K.J. Hemker, *Acta Mater.* 54 (2006) 2253.
10. G.J. Fan, L.F. Fu, H. Choo, P.K. Liaw, N.D. Browning, *Acta Mater.* 54 (2006) 4781.

11. D.S. Gianola, B.G. Mendis, X.M. Cheng, K.J. Hemker, *Mater. Sci. Eng. A*, doi:10.1016/j.msea.2006.12.155.
12. J.G. Brons, H.A. Padilla, G.B. Thompson, B.L. Boyce. *Scripta Mater.* 68 (2013) 781.
13. Gottstein, G. and L.S. Shvindlerman, *Grain boundary migration in metals: Thermodynamics, kinetics, applications* 1999, Boca Raton: CRC Press.
14. J.W. Cahn, Y. Mishin, A. Suzuki, *Acta Mater.* 54 (2006) 4953.
15. M. Horstemeyer, M. Baskes, V. Prantil, J. Philliber, S. Vonderheide, *Model. Simul. Mater. Sci. Eng.* 11 (2003) 265.
16. L. Brewer, D. Follstaedt, K. Hattar, J. Knapp, M. Rodriguez, I. Robertson, *Adv. Mater.* 22 (2010) 1161.
17. G.J. Tucker, S.M. Foiles. *Mater. Sci. Eng. A* 571 (2013) 207.
18. J. Bystrzycki, K.J. Kuryzdowski, W. Przetakiewicz. *Mater. Sci. Eng. A* 225 (1997) 188.
19. R.A. Varin and K.J. Kurzydowski, *Mater. Sci. Eng., t01* (1988) 221.
20. K. Konopka, *PhD Thesis*, Warsaw University of Technology, 1993.
21. W.J. Babyak, F.N. Rhines, *Trans. Am. Inst. Min., Metall. Pet. Eng.* 218 (1960) 21.
22. X. Zhang, A. Misra, H. Wang, A.L. Lima, M.F. Hundley, R.G. Hoagland, *J. Appl. Phys.* 97 (2005) 094302.
23. X. Zhang, A. Misra, H. Wang, M. Nastasi, J.D. Embury, T.E. Mitchell, R.G. Hoagland, J.P. Hirth, *Appl. Phys. Lett.* 84 (2004) 1096.
24. L. Capolungo, D.E. Spearot, M. Cherkaoui, D.L. McDowell, J. Qu, K.I. Jacob. *Journal of the Mechanics and Physics of Solids* 55 (2007) 2300-2327.
25. Z.H. Jin, P. Gumbsch, K. Albe, E. Ma, K. Lu, H. Gleiter, H. Hahn. *Acta Mater.* 56 (2008) 1126.
26. S.J. Dillon, G.S. Rohrer. *Acta Mater.* 57 (2009) 1.
27. D.L. Olmsted, S.M. Foiles, E.A. Holm. *Acta Mater.* 57 (2009) 3694.
28. S.M. Schlegel, S. Hopkins, M. Frary. *Scripta Mater.* 61 (2009) 88.
29. G.S. Rohrer. *J. Mater. Sci.* 46 (2011) 5881.

30. S. J. Shih, K. J. Dudeck, S. Y. Choi, M. Baeurer, M. Hoffmann, D. J. H. Cockayne, *Journal of Physics: Conference Series* **94**, (2008) 012008.
31. Y.G. Zheng, H.W. Zhang, Z. Chen, C. Lu, Y.W. Mai. *Physical Letters A* **373** (2009) 570-574.
32. L.A. Giannuzzi, F.A. Stevie, *Introduction to Focused Ion Beams*, Springer, New York, 2005.
33. G.B. Thompson, M.K. Miller, H.L. Fraser, *Ultramicroscopy* **107** (2-3) (2007) 131.
34. A. Avilov, K. Kuligin, S. Nicopoulos, M. Nickolskiy, K. Boulahya, J. Portillo, G. Lepeshov, B. Sobolev, J.P. Collette, N. Martin, A.C. Robbins, P. Fischione, *Ultramicroscopy* **107** (2007) 431.
35. D. Brandon, *Acta Metall.* **14** (1966) 1479.
36. A.J. Haslam, S.R. Phillpot, D. Wolf, D. Moldovan, H. Gleiter. *Mater. Sci. Eng. A* **318** (2001) 293.
37. H. Hu, *Trans. AIME* **224** (1962) 75.
38. U. Andrade, M.A. Meyers, K.S. Vecchio, A.H. Chokshi, *Acta Metall.* **42** (1994) 3183.
39. C.C. Koch, *Scripta Mater.* **49** (2003) 657.
40. F. Sansoz, V. Dupont, *Appl. Phys. Lett.* **89** (2006) 111901.
41. J.W. Cahn, Y. Mishin, A. Suzuki, *Acta Mater.* **54** (2006) 4953.
42. J. Wang, N. Li, O. Anderoglu, X. Zhang, A. Misra, J.Y. Huang, J.P. Hirth, *Acta Mater* **6** (2010) 2262.
43. N. Li, J. Wang, A. Misra, X. Zhang, J.Y. Huang, J.P. Hirth, *Acta Mater.* **59** (2011) 5989.
44. D. Jang, C. Cai, J.R. Greer, *NanoLetters* **11** (2011) 1743.
45. J. Luo, Z. Wang, *Mater. Sci. Forum* **15–17** (2006) 643.
46. Y.B. Wang, M.L. Sui, E. Ma, *Philos. Mag. Lett.* **87** (2007) 935.
47. J. Wang, N. Li, O. Anderoglu, X. Zhang, A. Misra, J.Y. Huang, J.P. Hirth, *Acta Mater.* **58** (2010) 2262.
48. C. Chen, J. Liu, Z. Wang, *Mater. Sci. Eng. A* **558** (2012) 285.

49. O. Anderoglu, A. Misra, J. Wang, R.G. Hoagland, J.P. Hirth, X. Zhang, *Inter. J. Plasticity*, 26 (2010) 875

## CHAPTER 6

### CONCLUSIONS AND FUTURE WORK

In the case where grain boundary motion was driven by the grain boundary curvature and the addition of thermal energy, during the annealing of the Cu film, a manner of grain growth was observed that allowed for a monomodal grain size distribution to be maintained. It was evident that the low angle grain boundaries ( $<15^\circ$ ) were consumed by measured increases in the boundary fractions of the  $\Sigma 3$ ,  $\Sigma 5$ ,  $\Sigma 7$ , and  $\Sigma 9$  boundaries. With the addition of thermal energy into the system, these low- $\Sigma$  CSL boundaries were thermodynamically favorable for growth due to the low grain boundary energy associated with the symmetry of the boundaries. Additionally, of the  $\Sigma 3$  boundaries identified within the system, many were identified as twin boundaries. This was to be expected, since it is well known that Cu forms twin boundaries in response to mechanical loading, annealing, and from deposition. These twin boundaries, however, were observed to allow for the grain growth and were responsible for the increase in the  $\Sigma 3$  boundary fraction.

Alternatively, Ni was found to undergo a manner of grain growth that led to stages of grain size distributions that transitioned from monomodal to bimodal and then to monomodal again, although this second monomodal stage described a set of grains that were irregularly shaped. While the bimodal grain size distribution was present, the boundary fractions of the  $\Sigma 3$  and  $\Sigma 9$  CSL boundaries peaked. Once these boundary fractions reduced to their ambient values,

this bimodal distribution was no longer present, indicating their involvement in the abnormal growth behavior. Although there were also continual increases in the boundary fractions of the  $\Sigma 5$ ,  $\Sigma 7$ , and  $\Sigma 11$  CSL boundaries, it was determined that the  $\Sigma 3$  and  $\Sigma 9$  boundaries allowed for the irregular growth of some of the Ni grains by minimizing the strain energy of the system.

When alloying Cu and Ni at a fraction of  $\text{Cu}_{80}\text{Ni}_{20}$ , it was determined that a mode of grain growth was present that allowed for the film to maintain a monomodal distribution of grain sizes, similar to the Cu, although the distribution was much broader in this case. The grains that grew large in this alloy system, however, were of a different orientation than what was thermodynamically favorable for the Cu or the Ni system. The large grains were identified to be in a  $\{-113\}$  orientation. This growth was accompanied by a large fraction of low angle grain boundaries and increases in the boundary fractions of the  $\Sigma 3$ ,  $\Sigma 5$ ,  $\Sigma 7$ ,  $\Sigma 9$ , and  $\Sigma 11$  CSL boundaries. Upon investigation, the  $\Sigma 9$  boundaries were identified as the boundaries that allowed for the growth of the  $\{-113\}$  grains in the alloyed system.

In the case where grain boundary migration was driven by the application of a mechanical load at cryogenic temperatures, three regions were identified to undergo different forms of microstructural evolution. These regions were characterized as (1) the parent region, (2) the pile-up region, and (3) the indented region (the grains under the center of the indenter tip). When twin boundaries were present within the nanostructured Cu, there was observed grain growth in the pile-up region of the indent. For nanotwinned Cu with a  $\langle 111 \rangle$  texture, this growth was attributed to a detwinning mechanism that left behind several  $\Sigma 7$  subgrains within the large grains. In the  $\langle 100 \rangle$  textured nanotwinned film, however, the grain growth that occurred was not attributed to a complete detwinning. Instead, there was still a high density of twin boundaries found outlining the large grains in the pile-up region. In both films, however, the

region under the center of the indenter underwent grain refinement. It is proposed that the grain growth occurred, even at cryogenic temperatures, because of the shear forces acting on the twin boundaries within the flank of the indented region. This observed growth is in contrast to what was observed in the nanostructure Cu film without twin boundaries. As a result of the cryogenic indentation in the un-twinned case, the grains in the pile-up region responded to the shear stresses by undergoing refinement and distortion.

While this research provides experimental validation to many published simulations, there is still work that can be done in the future for *in situ* annealing experiments and for cryogenic indentation research. Future annealing research could focus on alloyed thin films. This work showed that the addition of an alloying element alters the grain growth mechanisms, and in this case, it was attributed to the alloying element coming out of solid solution and segregating to the grain boundaries. Future work could be designed in order to quantify this segregation to specific grain boundaries. Additionally, in this case, the films were deposited onto silicon nitride windows, which did not allow for atom probe tomography due to its insulating properties. Future work could quantify not only the segregation of solute atoms to grain boundaries but could compare the relative solute content present at specific CSL and twin boundaries.

In the cryogenic study, future experimental work could be done to determine if the same growth behavior is seen in other metal films with grown-in twin boundaries. This research showed that when twin boundaries are present in the microstructure, growth occurs in the pile-up region – where shear stresses are present. Additionally, future work could investigate the cryogenic indentation induced growth mechanisms of nanotwinned Cu in a bulk form. This study investigated the indentation of thin films, but future work could look into a more three-

dimensional stress field to determine the depth at which this growth is allowed. There has been limited modeling that has been done to elucidate this behavior, but there have not been any experimental studies performed on the indentation of a nanotwinned bulk sample. Future modeling work could be performed in order to investigate the specific detwinning processes associated with shear stresses at cryogenic temperatures. This could elucidate whether or not the observed differences in grain growth between the  $\langle 111 \rangle$  and the  $\langle 100 \rangle$  nanotwinned films in this research was due to a difference in texture or due to a difference in twin boundary density. Whichever the case may be, the experimental results of this study can provide forward feeding direction for future computational studies.

## CHAPTER 7

### REFERENCES

1. E.A. Holm, S.M. Foiles. *Science* 328 (2010) 1138.
2. O. Anderoglu, A. Misra, H. Wang, X. Zhang. *J. Appl. Phys.* 103 (2008) 094322-1.
3. E.A. Holm, G.N. Hassold, M.A. Miodownik. *Acta Mater.* 49 (2001) 2981.
4. G. Gottstein, L.S. Shvindlerman. *Grain Boundary Migration in Metals*. CRC Press: 2010.
5. G. Gottstein. *Physical Foundations of Materials Science*. Springer: New York, 2004.
6. L. Lu, Y. Shen, X. Chen, L. Qian, K. Lu. *Science* 304 (2004) 423.
7. J.M. Howe. *Interfaces in Materials: Atomic Structure, Thermodynamics and Kinetics of Solid-Vapor, Solid-Liquid and Solid-Solid Interfaces*. Wiley: 1997.
8. B.L. Boyce, H.A. Padilla. *Metall. Mater. Trans. A* 42A (2011) 1793.
9. M. Hillert. *Acta Metallurgica*. 13 (1965) 227.
10. N.P. Louat, *Acta Metall.* 22 (1971) 721.
11. M. Zinke-Allmang, L.C. Feldman, M.H. Grabov, *Surf Sci Rep.* 16 (1992) 377.
12. C.M. Hefferan, S.F. Li, J. Lind, U. Lienert, A.D. Rollett, R.M. Suter. *Mater Sci Forum* 715-716 (2012) 447.
13. G. Riontino, C. Antonoio, L. Battezzati, F. Marino, M.C. Tabasso. *J Mater. Sci.* 14 (1979) 86.
14. G.S. Rohrer. *J Mater Sci* 46 (2011) 5881.
15. K.S. Kumar, H. Van Swygenhoven, S. Suresh. *Acta Mater* 51 (2003) 5743.

16. K.S. Kumar, S. Suresh, M.F. Chisholm, J.A. Horton, P. Wang. *Acta Mater.* 51 (2003) 387.
17. J. Schiøtz, K.W. Jacobsen. *Science.* 301 (2003) 1357.
18. H. Van Swygenhoven. *Mater. Sci. Eng. A.* 483 (2008) 33.
19. X.Y. Li, Y.J. Wei, L. Lu, K. Lu, H.J. Gao. *Nature.* 464 (2010) 877.
20. B.L. Boyce, H.A. Padilla. *Metall. Mater. Trans. A.* 42A (2011) 1793.
21. H.A. Padilla, B.L. Boyce. *Exp. Mech.* 50 (2010) 5.
22. Y. Estrin, A. Vinogradov. *Int. J. Fatigue.* 32 (2010) 898.
23. V.Y. Gertsman, R. Birringer. *Scripta Metall. Mater.* 30 (1994) 577.
24. A.B. Witney, P.G. Sanders, J.R. Weertman, J.A. Eastman. *Scripta Metall. Mater.* 33 (1995) 2025.
25. D.S. Gianola, S.V. Petegem, M. Legros, S. Brandstetter, H.V. Swygenhoven, K.J. Hemker. *Acta Mater.* 54 (2006) 2253.
26. C.C. Battaile, W.A. Counts, G.W. Wellman, T.E. Buchheit, E.A. Holm. *Metall. Mater. Trans. A.* 38 (2007) 2513.
27. H. Zhang, M.I. Mendeleev, D.J. Srolovitz. *Acta Mater.* 52 (2004) 2569.
28. D. Farkas, S. Mohanty, J. Monk. *Mater. Sci. Eng. A.* 493 (2008) 33.
29. J. Monk, D. Farkas. *Phys. Rev. B.* 75 (2007) 045414.
30. J. Schiøtz. *Mater. Sci. Eng. A.* 375 (2004) 975.
31. D.L. Olmsted, E.A. Holm, S.M. Foiles. *Acta Mater.* 57 (2009) 3704.
32. D.L. Olmsted, S.M. Foiles, E.A. Holm. *Acta Mater.* 57 (2009) 3694.
33. E.A. Holm, N. Zacharopoulos, D.J. Srolovitz. *Acta Mater.* 46 (1998) 953.
34. G. Dieter: *Mechanical Metallurgy, 3rd ed.*, McGraw-Hill: New York, NY 1986.
35. D. Jia, K.T. Ramesh, E. Ma. *Acta Mater.* 51 (2003) 3495.
36. A. Hasnaoui, H. Van Swygenhoven, P.M. Derlet. *Phys. Rev. B.* 66 (2002) 184112.

37. D. Moldovan, V. Yamakov, D. Wolf, S.R. Phillpot. Phys. Rev. Lett. 89 (2002) 206101.
38. K. Zhang, J.R. Weertman, J.A. Eastman. Appl Phys Lett. 85 (2004) 5197.
39. F. Sansoz, V. Dupont. Appl Phys Lett. 89 (2006)
40. S.P. Hau-Riege and C.V. Thompson. Appl Phys Lett. 76 (2000) 309.
41. C.V. Thompson. J. Appl. Phys. 58 (1985) 763.
42. C.V. Thompson, H.J. Frost, F. Spaepen. Acta Met. 25 (1987) 887.
43. C.V. Thompson, J. Floro, J.I. Smith. J Appl Phys. 67 (1990) 4099.
44. C.V. Thompson. Interface Sci. 6 (1998) 85.
45. R.E. Reed-Hill. *Physical Metallurgy Principles*. PWS Engineering: New York, NY 1973.
46. K.G.F. Janssens, D. Olmsted, E.A. Holm, S.M. Foiles, S.J. Plimpton, P.M. Derlet. Nature Materials. 5 (2006) 124.
47. J.B. Koo and D.Y. Yoon. Metal Mater Trans A. 32 (2001) 1911.
48. X. Zhang, A. Misra, H. Wang, M. Nastasi, J.D. Embury, T.E. Mitchell, R.G. Hoagland, J.P. Hirth. Appl Phys Lett. 84 (2004) 1096.
49. A. Misra, X. Zhang, D. Hammon, R.G. Hoagland. Acta Mater. 53 (2005) 221.
50. X. Zhang, H. Wang, X.H. Chen, L. Lu, K. Lu, R.G. Hoagland, A. Misra. Appl Phys Lett. 88 (2006) 173116.
51. O. Anderoglu, A. Misra, H. Wang, F. Ronning, M.F. Hundley, X. Zhang. Appl Phys Lett. 93 (2008) 083108.
52. J.P. Hirth, J. Lothe, *Theory of dislocations*. Krieger, Melbourne (FL) 1992.
53. V. Yamakov, D. Wolf, S.R. Phillpot, H. Gleiter. Acta Mater. 50 (2002) 5005.
54. J. Wang, H. Huang. Appl Phys Lett, 85 (2004) 5983.
55. J. Wang, O. Anderoglu, J.P. Hirth, A. Misra, X. Zhang. Appl Phys Lett. 95 (2009) 21908.
56. Q. Hu, L. Li, N.M. Ghoniem. Acta Mater. 57 (2009) 4866.
57. J. Wang, H. Huang. Mater Res Soc Symp Proc. 849 (2004) 91.

58. J. Wang, H. Huang, S.V. Kesapragada, D. Gall. *Nano Lett*, 5 (2005) 2505.
59. J. Wang, H. Huang. *Appl Phys Lett*. 88 (2006) 203112.
60. O. Anderoglu, A. Misra, J. Wang, R.G. Hoagland, J.P. Hirth, X. Zhang. *Int J Plasticity*. 26 (2010) 875.
61. X. Zhang, A. Misra, H. Wang, A.L. Lima, M.F. Hundley, R.G. Hoagland. *J Appl Phys*. 97 (2005) 094302.
62. L. Lu, X. Chen, X. Huang, K. Lu. *Science*. 323 (2009) 607.
63. E. Ma, Y.M. Wang, Q.H. Lu, M.L. Sui, L. Lu, K. Lu. *Appl Phys Lett*. 85 (2004) 4932.
64. T. Zhu, J. Li, A. Samanta, H.G. Kim, S. Suresh. *Proc Natl Acad Sci USA*. 104 (2007) 3031.
65. K.A. Afanasyev, F. Sansoz. *Nano Lett*. 7 (2007) 2056.
66. F. Sansoz, H. Huang, D.H. Warner. *JOM*. 60 (2008) 79.
67. J. Wang, N. Li, O. Anderoglu, X. Zhang, A. Misra, J.Y. Huang, J.P. Hirth. *Acta Mater*. 58 (2010) 2262.
68. C. Chen, J. Liu, Z. Wang. *Mater Sci Eng A*. 558 (2012) 285.
69. P. Moeck, S. Rouvimov, E.F. Rauch, M. Veron, H. Kirmse, I. Hausler, W. Neumann, D. Bultreys, Y. Maniette, S. Nicolopoulos. *Cryst Res Tech*. 46 (2011) 589.
70. E.F. Rauch, J. Portillo, S. Nicolopoulos, D. Bultreys, S. Rouvimov, P. Moeck. *Z. Kristallogr*. 225 (2010) 103.
71. Vincent, P.A Midgley, *Ultramicroscopy*. 53 (1994) 271.
72. P. Moeck and S. Rouvimov. *Z Kristallogr*. 225 (2010) 110.
73. TSL Orientation Imaging Microscopy (OIM) Data Analysis 5 Software Help File.

## **CHAPTER 8**

### **APPENDICES**

**Appendix A.** Procedure for the collection of a PED scan using the nanoMEGAS ASTAR system

1. Load sample into FEI Tecnai TEM
2. Select sample holder in Tecnai user interface
3. Turn on Digistar P1000 nanoMEGAS communication controller
4. Turn on nanoMEGAS GIS box
5. Turn on nanoMEGAS Laptop
6. Open Digistar Control software on laptop

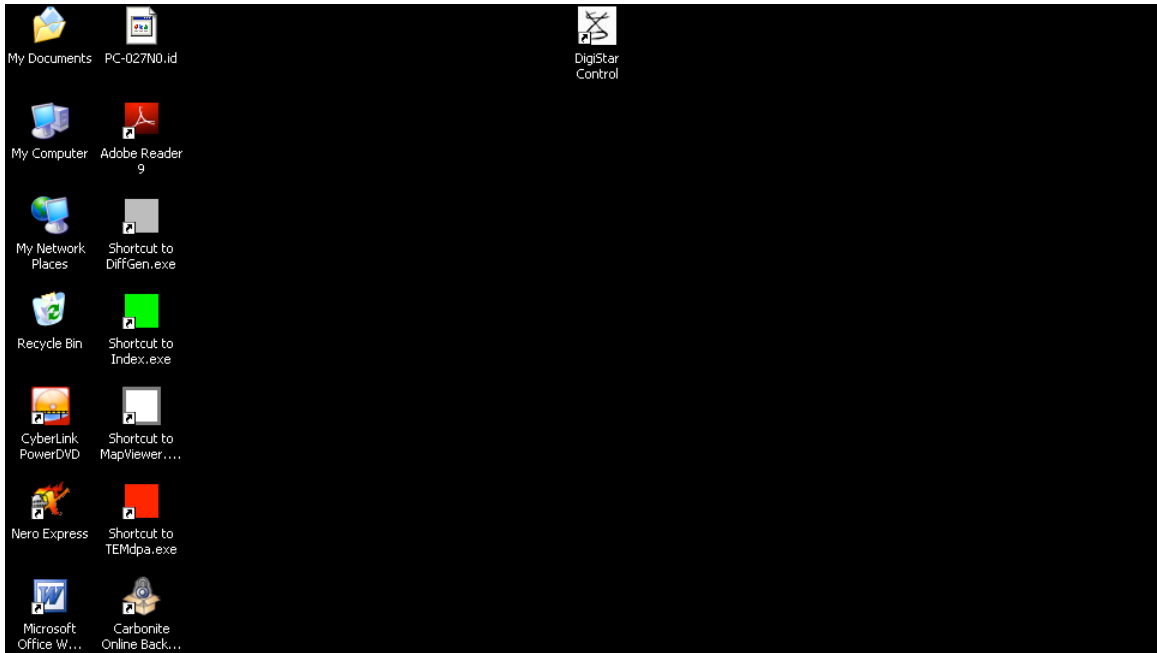


**Figure A.1.** nanoMEGAS desktop showing the Digistar Control software icon

7. Click Beam Scan on

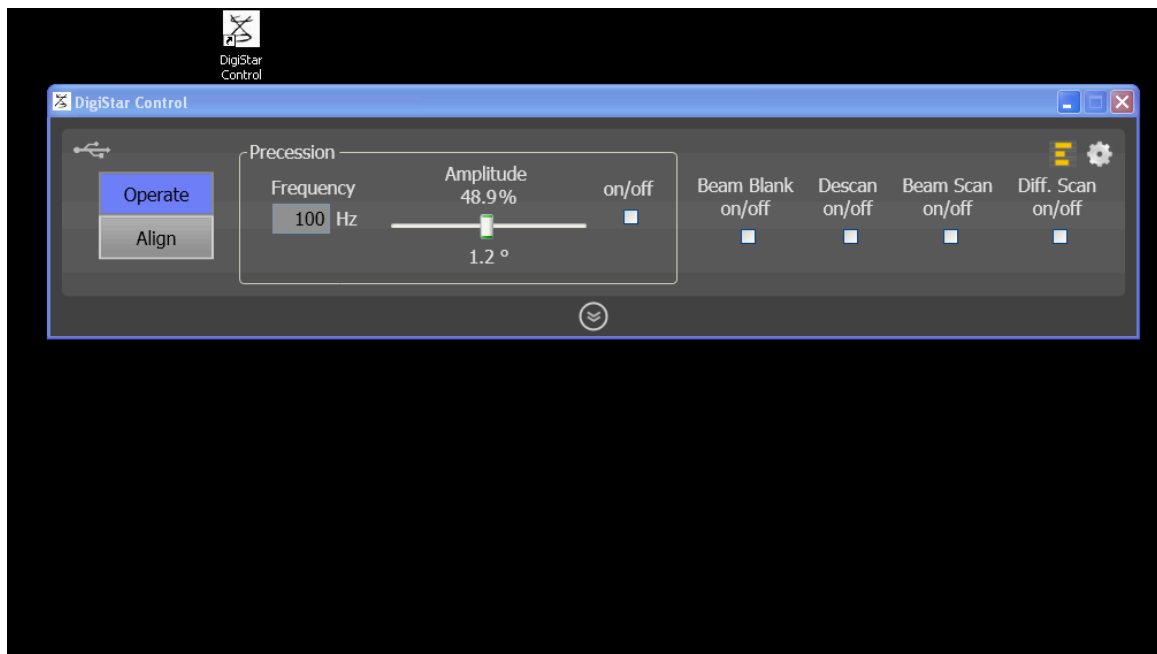


**Figure A.2.** Digistar control software platform showing the location of the Beam Scan button

8. Set C2 aperture to 1

9. Set FEG register to nanoMEGAS (SA, Spot size of 9)

10. Align using normal procedures

- a. C2 alignment at 125kx
- b. Condenser stigmation at 400kx
- c. Find eucentric height
- d. Beam tilt pivot points at 400kx
- e. Rotation centering at 86kx
- f. Re-stigmatate at 400kx

11. Open RED Software (TEMdpa.exe)

- a. Check to make sure the factory settings are still the preset values
  - i. Format 7 Mode 7, Y8
  - ii. AOI width: 144, height: 144, x offset: 24, y offset: 0, Speed: 400, Packets: 496

## 12. Precession Alignment

- a. Achieve optimal focus
  - i. Click scan diffraction pattern (under configuration tab), adjust focus until the transmitted spot does not translate
- b. In Digistar software, click operate
- c. Select degree of precession ( $1^\circ$ )
- d. Click Precession on
- e. Go to Bright Field image
- f. Click Beam Pivot Point at 32kx
  - i. Use all four knobs on digistar controller to make one fine spot
- g. Click Descan Align
  - i. Go into diffraction mode
  - ii. Make transmitted beam one fine spot
- h. Click Image Pivot Point
  - i. Go to bright field image
  - ii. Bring the beam to one fine spot (corrects anything descan align disrupted)

13. Bring up small phosphorus screen

14. Place Stingray camera over window, turn off lights and TEM monitors

15. Name the scan under 'Serial Name'

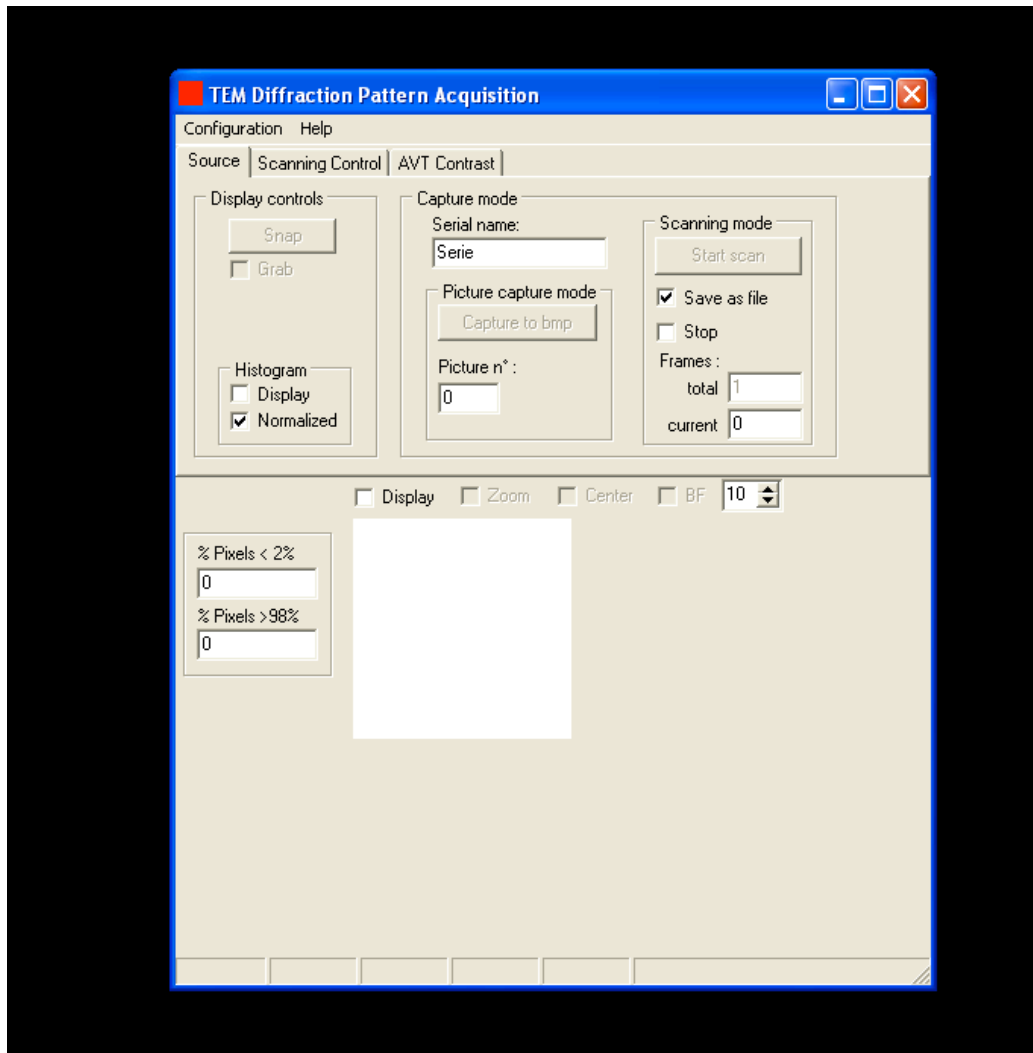


Figure A.3. nanoMEGAS's Red software interface

16. Click Grab to go live from the camera

17. Configuration tab

- a. Voltage 200000V
- b. X scale 0.5 nm/step
- c. Y scale 0.5 nm/step
- d. Image calibration 170.0 ppcm
- e. Camera Length 6.2 cm
- f. Target Drawing 100
- g. Initial Orientation  $0^\circ$

## 18. Scanning Control

- a. For a 2  $\mu\text{m}$  x 2  $\mu\text{m}$  scan box,
  - i. X axis: Point Count of 200, Step Width of 20
  - ii. Y axis: Point Count of 200, Step Width of 20
- b. With precession on, the PC and SW have to be a factor of ten of each other

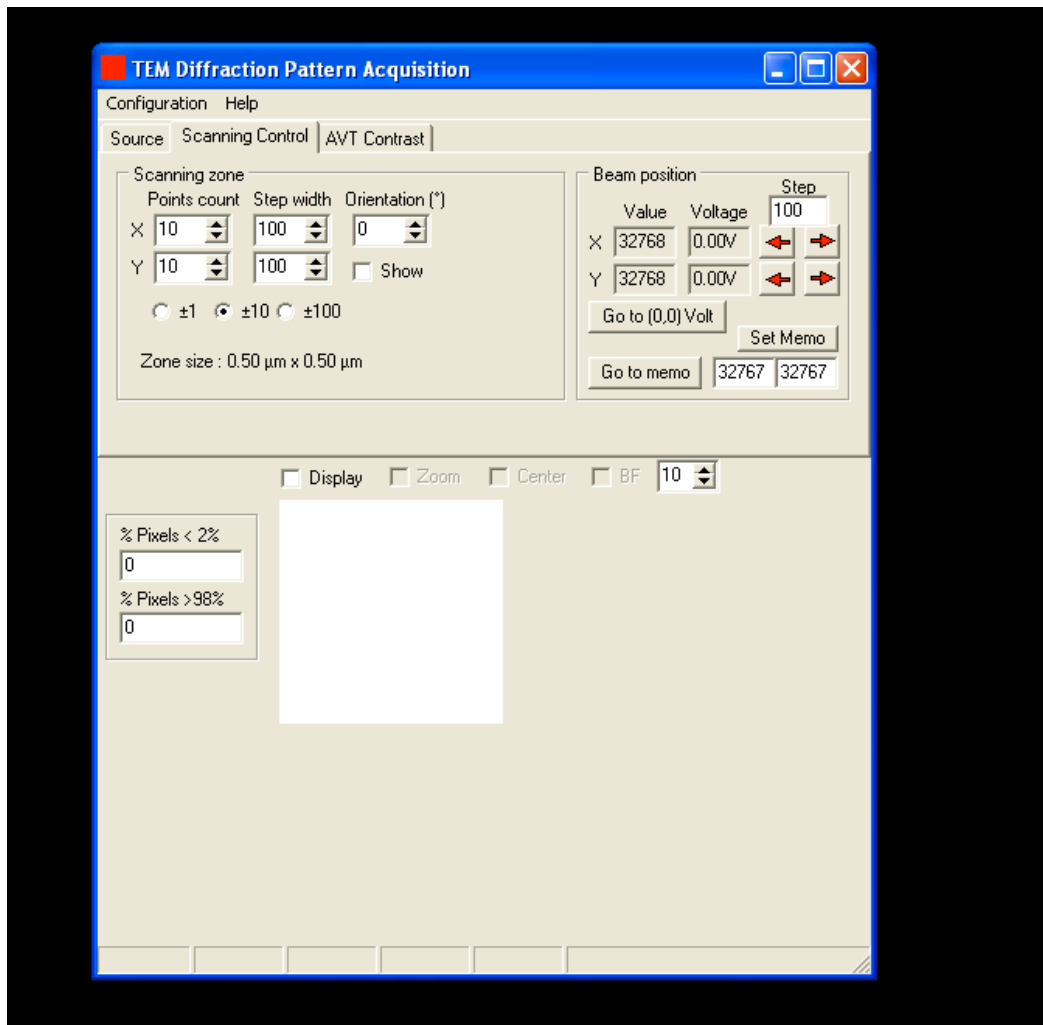


**Figure A.4.** nanoMEGAS's Red software showing the scanning control tab

19. Click show to see the scanning area in Bright Field image
  20. Go into diffraction mode, center the transmitted beam
    - a. Insure the pattern is not translating by using the focus knob
  21. Unclick Grab, Start Scan
  22. Check that all the blocfile information is correct
  23. Click Update Blocfile
  24. When the scan is completed, the file will be on the C drive in a folder named blocfiles within ASTAR
- From here down, all analysis can be done off-line

### Creating a Bank of Diffraction Patterns for Analysis

1. Open the GRAY software (DiffGen.exe)

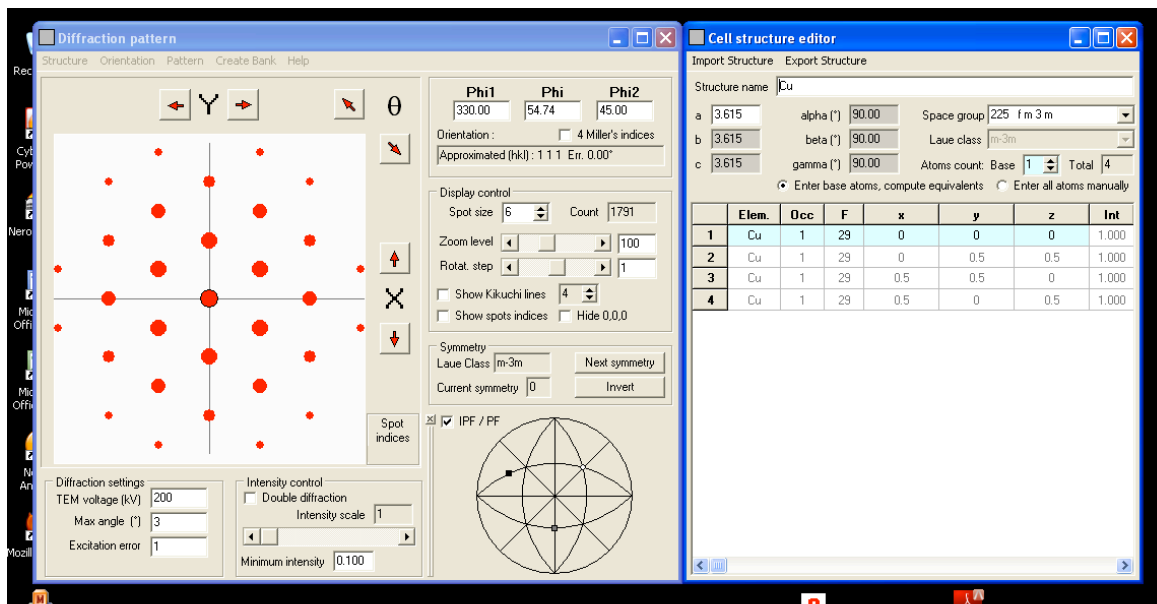
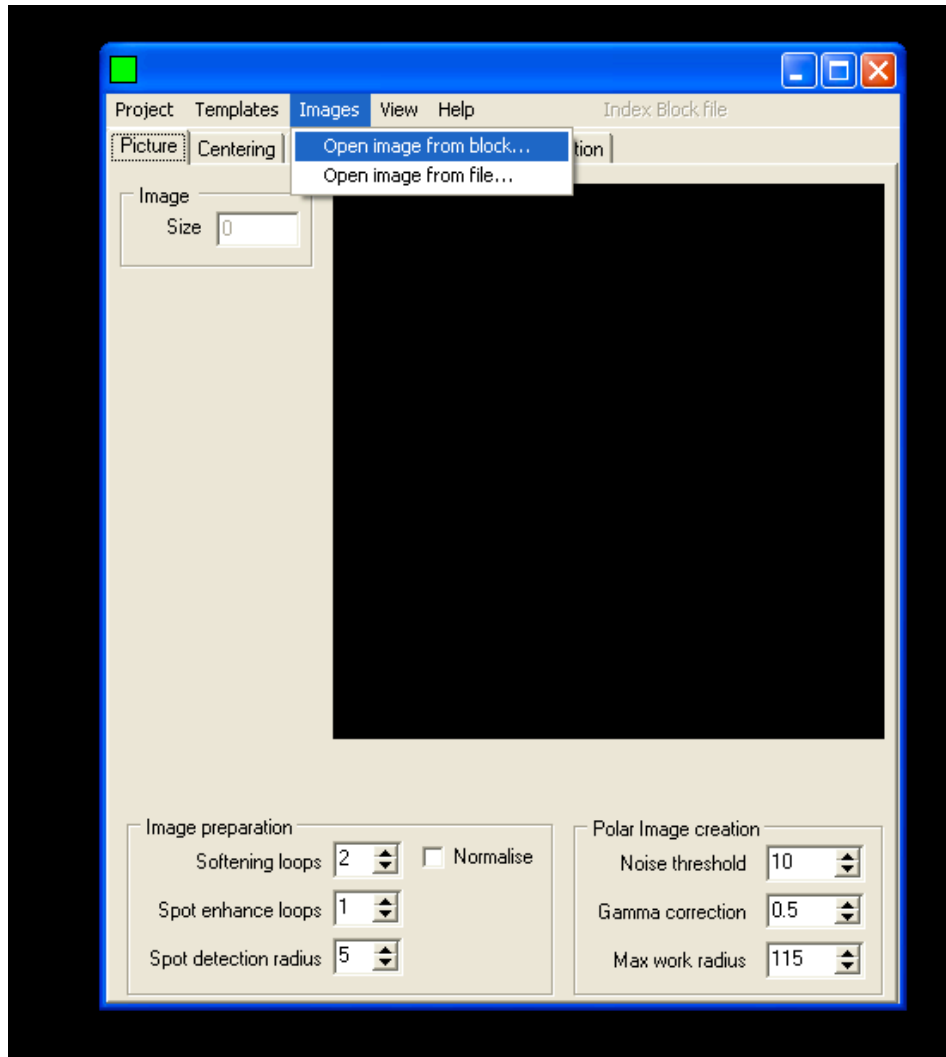


Figure A.5. nanoMEGAS's Grey software showing the template bank creation

2. Diffraction settings
  - a. Input TEM voltage of 200 KV
  - b. Maximum convergence angle of 3-4°
  - c. Excitation error of 1
3. For cubic materials, use a step count of 50
4. For lower symmetries, use a step count of 100
5. Import structure on the right screen
6. Click Create Bank
  - a. Create File, NOT replace current
7. Save created bank to the analysis folder

#### Analyzing the blocfile

1. Open the GREEN software
2. Start a New Project (or Open an Existing)
3. Images drop down menu
  - a. Open image from block



**Figure A.6.** nanoMEGAS's Green software showing how to open an image from a block file

- b. Select block file from the analysis folder
- c. Edit the virtual bright field image by altering the virtual field zoom
- d. Click and drag on virtual bright field to find a strong diffraction pattern
- e. Click Open

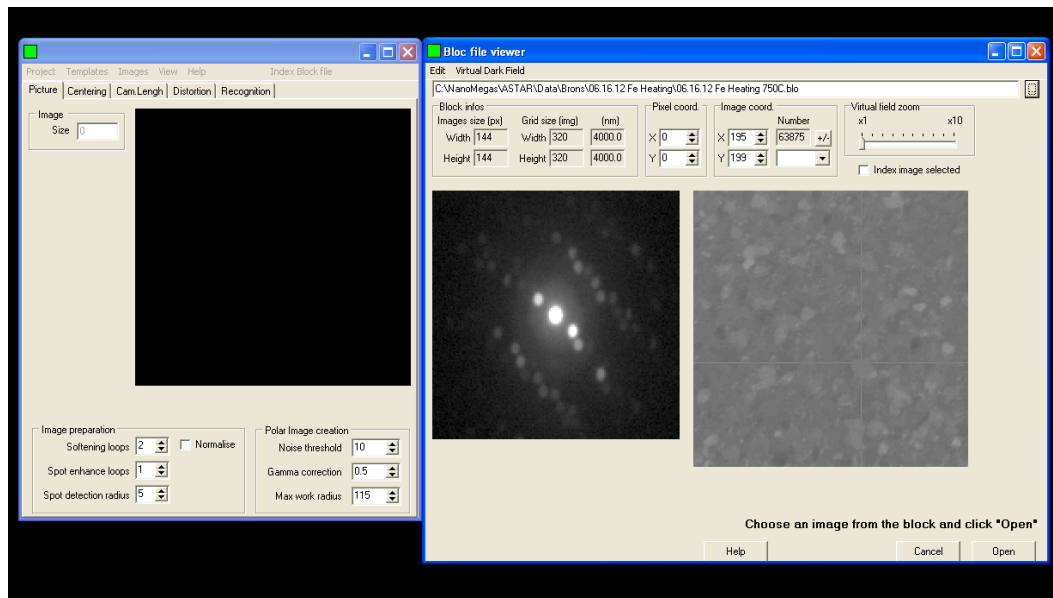


**Figure A.7.** nanoMEGAS's Green software showing how to select a diffraction pattern from the orientation scan.

4. Template drop down menu

a. Add template bank

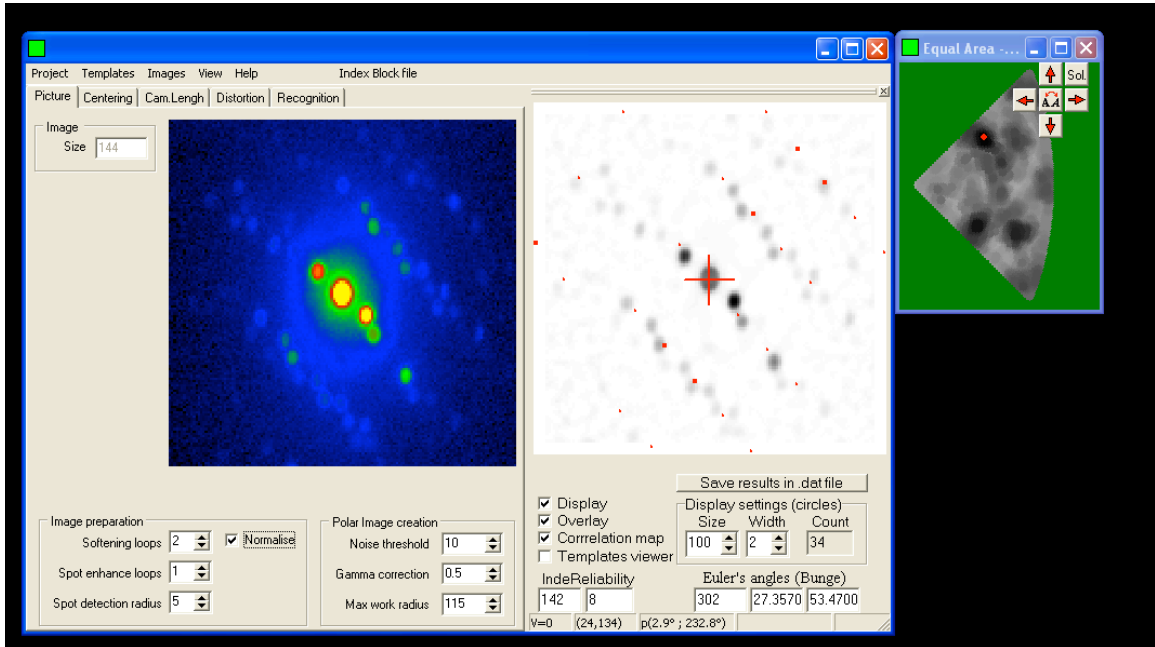


Figure A.8. nanoMEGAS's Green software showing how to add a template bank

5. Picture tab

- a. Spot detection radius of 2.15-3 as a default
- b. Softening loops of 2
- c. Spot enhance loops of 1
- d. Noise threshold of 10
- e. Gamma correction of 0.5
- f. Max working radius of 115

6. Centering tab

- a. Smoothing radius allows a unique max just under saturation (5-10 px)
- b. Center shift max (10 px)
- c. Click Auto Center

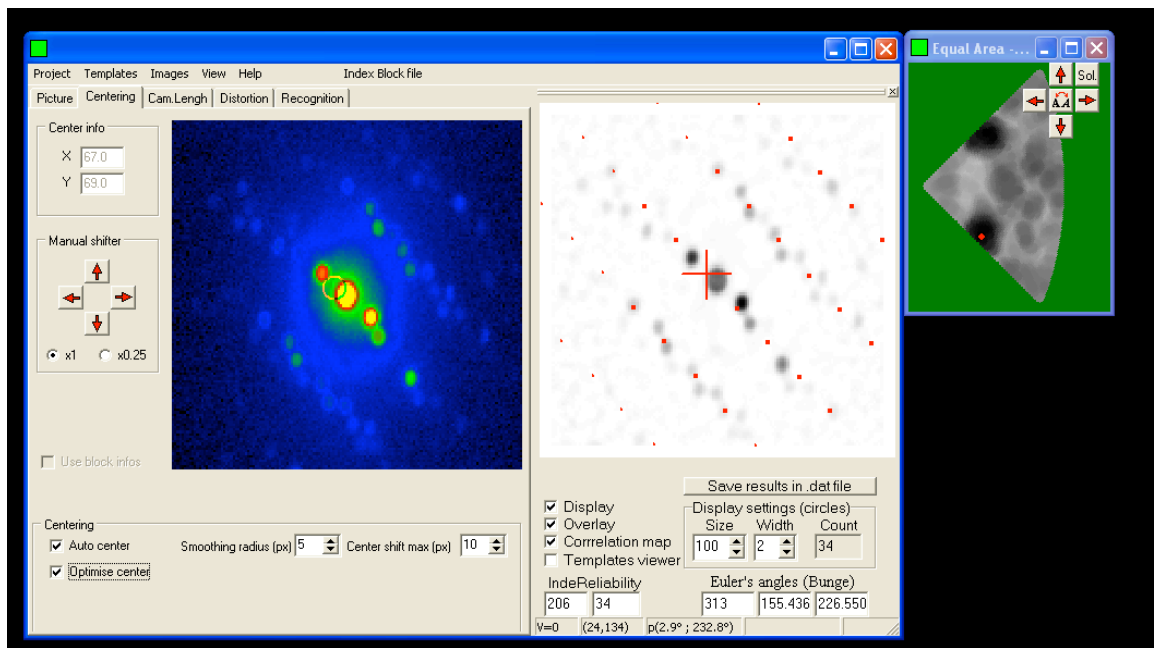


**Figure A.9.** nanoMEGAS's Green software showing how to optimize the diffraction pattern's center spot

## 7. Camera Length tab

- Scan camera length
- Identify clear intensity maximum
- Left click to zoom in on local maximum
- Right click on local maximum to set to block file

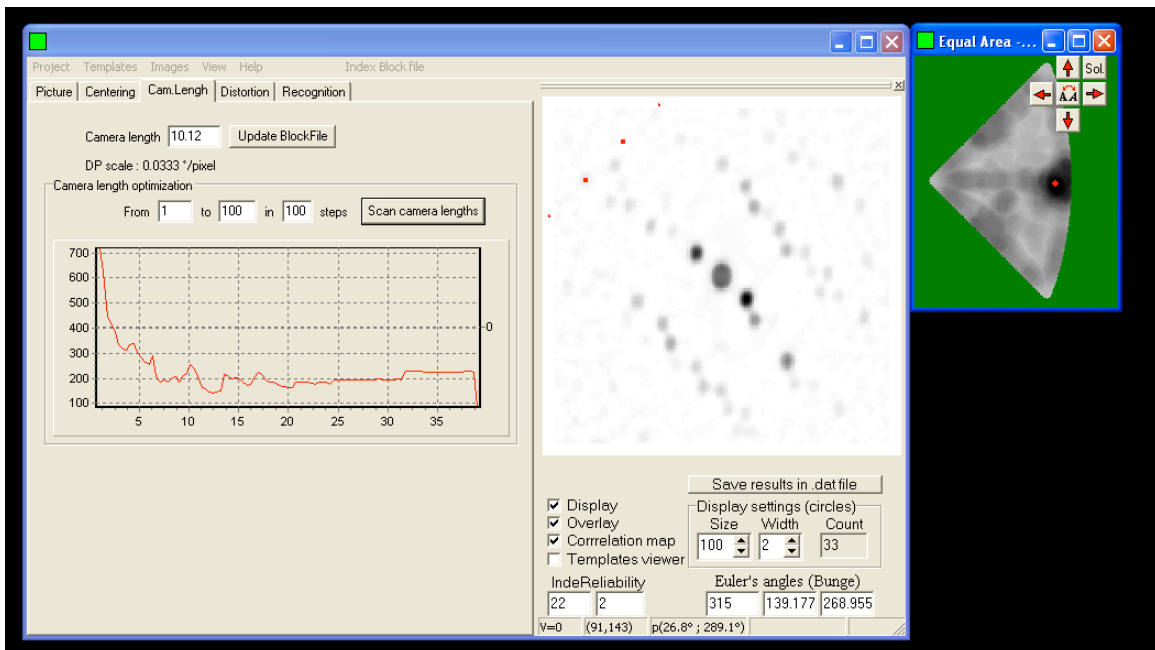
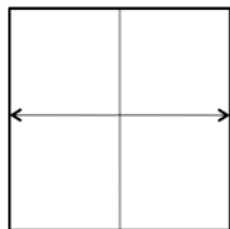


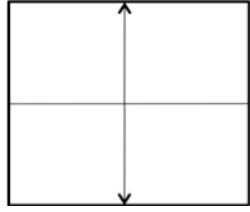
**Figure A.10.** nanoMEGAS's Green software showing how to optimize the camera length

## 8. Distortion tab

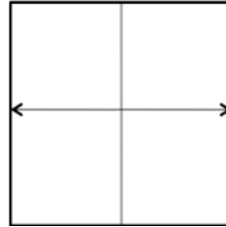
- Input any known disorientations



- of -40 to start

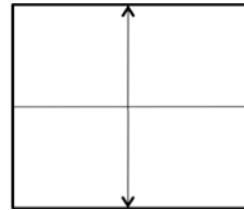


c. of 25 to start



d. Under Parameter to Optimize, click on then scan values

e. Use the left click to zoom in and the right click to identify a maximum



f. Under Parameter to Optimize, click on then scan values

g. Use the left click to zoom in and the right click to identify a maximum

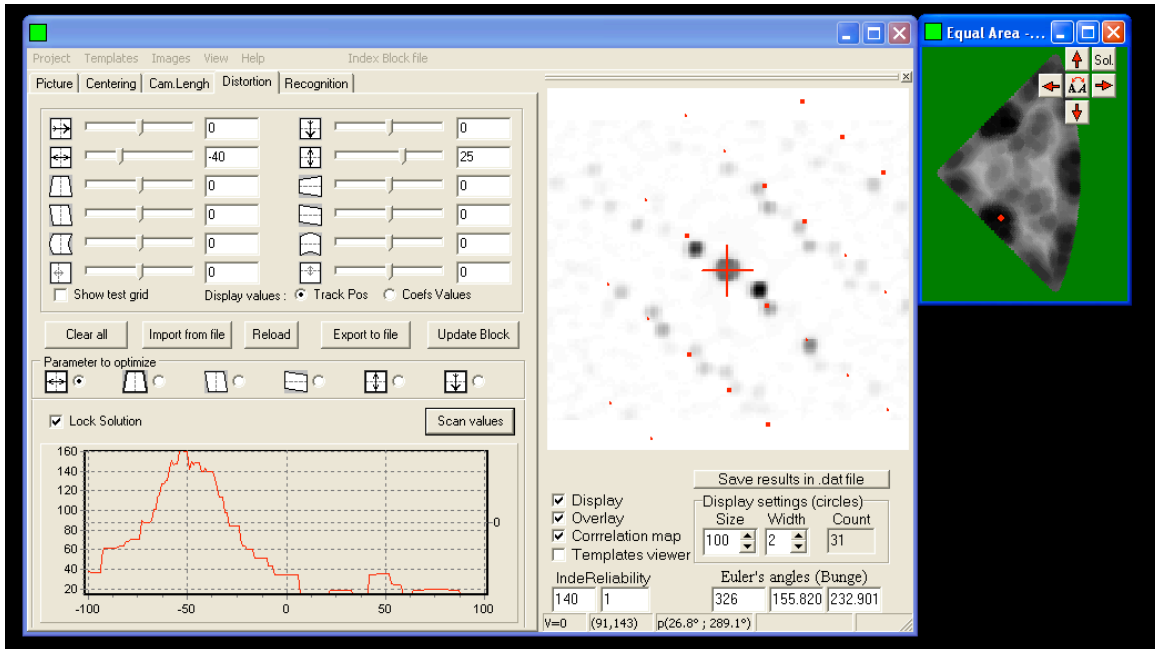
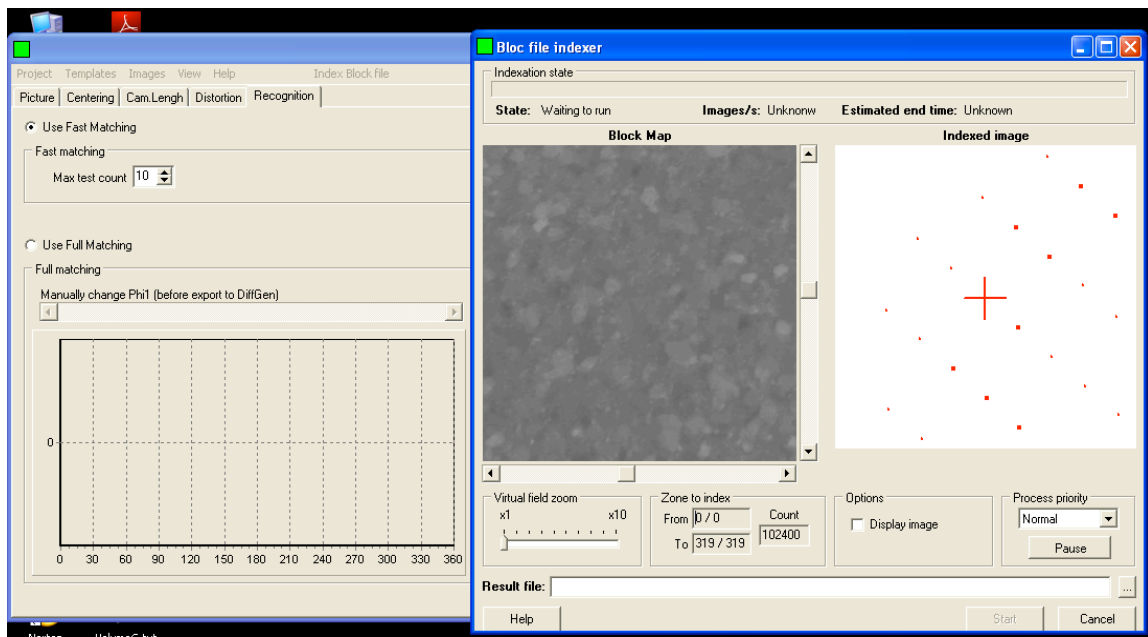


Figure A.11. nanoMEGAS's Green software showing how to optimize the distortion values

9. Click Index Block File
  - a. Name the Result file, Save to analysis folder
  - b. Click Start



**Figure A.12.** nanoMEGAS's Green software showing how to index the collected block file

### Viewing the indexed maps

1. Open the WHITE software (MapView.exe)

2. Click Files
  - a. Open Result File
  - b. Select Result File from analysis folder

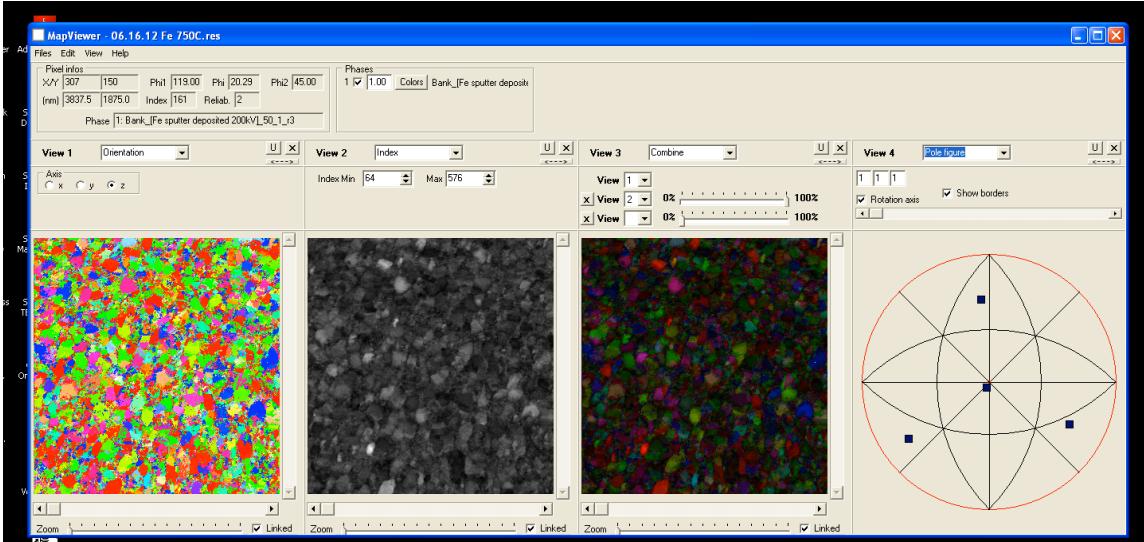


**Figure A.13.** nanoMEGAS's White software showing how to view the indexed orientation maps

### 3. Exporting the scan file for TSL OIM 5 Analysis

- a. Click File
- b. Export - .ang

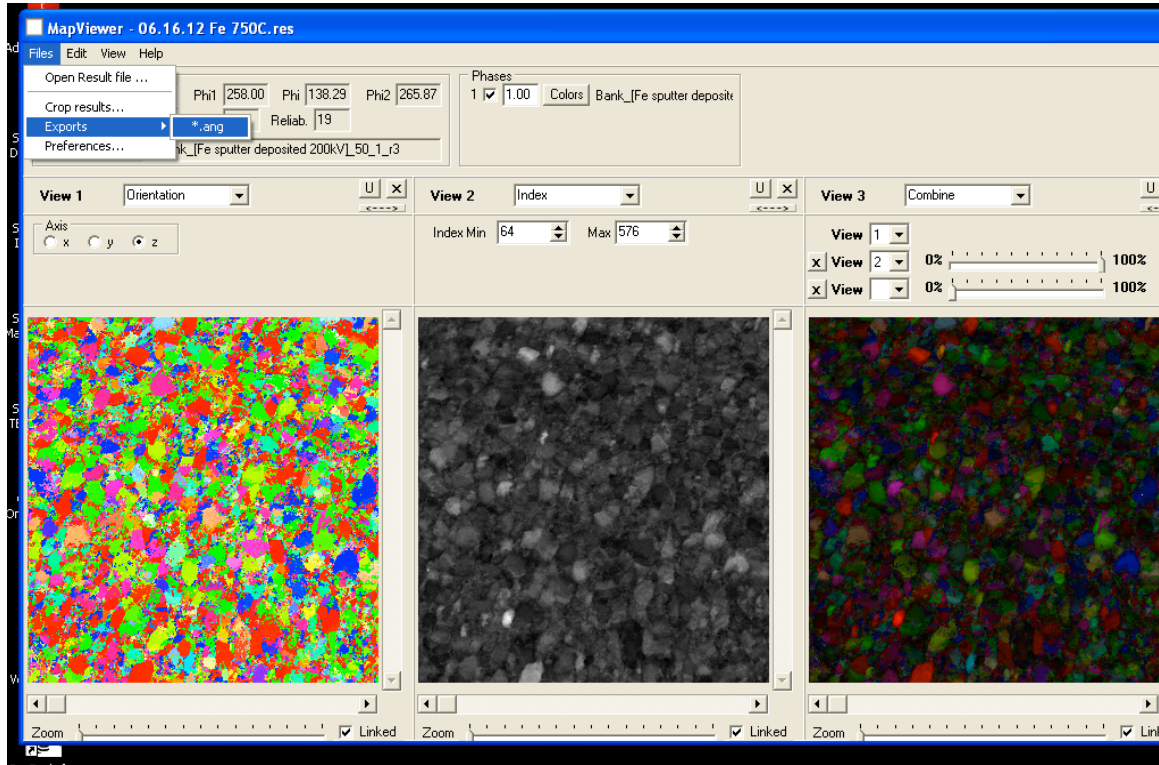


**Figure A.14.** nanoMEGAS’s White software showing how to export the orientation map to a .ang file

A few housekeeping notes:

- The files created from the PED orientation mapping scans are several gigabytes, please remove the collected files from the folder labeled ‘blocfiles’ as soon as the scans are completed and move them to a backed up folder.

- When the orientation mapping is completed, please move all of collected files from the laptop onto an external hard drive so that the analysis can be done on the support computer and so the laptop does not end up slowing down due to too much saved data
- The laptop is what runs the nanoMEGAS, please be very careful with it and with what is loaded onto it.
- The precession alignment can take up to another hour after the TEM is aligned, and each scan can take from 15 minutes to hours depending on the scanned area of interest, please schedule time accordingly.
- The Stingray camera is very light sensitive, do not open the door during the scan or bump the table, as these will cause the run to be a failure.

## Appendix B. Preparation of PED-Ready TEM Foils

1. At a tilt of  $52^\circ$ , blindly deposit Pt at a voltage of 30 keV and a current of 0.1 nA over a region  $45 \times 5 \mu\text{m}$  in area with a thickness of 200 nm. This layer will protect the surface of the film from any potential ion damage during imaging and focusing.
2. At a tilt of  $52^\circ$ , focus on the sample using the ion beam, and deposit Pt at a voltage of 30 keV and a current of 0.3 nA over a region  $40 \times 2 \mu\text{m}$  with a thickness of  $3 \mu\text{m}$ . This Pt bar will be the cap for the TEM foil.
3. At a tilt of  $52^\circ$ , perform a 'Regular Cross Section' cut over a box adjacent to the bottom long edge of the Pt bar, measuring  $42 \times 8 \mu\text{m}$  to a depth of  $7 \mu\text{m}$  with a voltage of 30 keV and a current of 3 nA.
4. Repeat Step 3 on the top side of the Pt bar.
5. At a tilt of  $52^\circ$ , perform a 'Cleaning Cross Section' cut over a box adjacent to the bottom edge Pt bar, measuring  $42 \times 0.5 \mu\text{m}$  to a depth of  $7 \mu\text{m}$  with a voltage of 30 keV and a current of 1 nA.
6. Repeat Step 5 on the top side of the Pt bar.
7. Tilt the stage down to  $22^\circ$  and perform a cut along the bottom of the foil measuring  $38 \times 0.5 \mu\text{m}$  to a depth of  $2 \mu\text{m}$  with a voltage of 30 keV and a current of 0.3 nA.
8. At a tilt of  $22^\circ$ , completely cut the left side of the foil free from the substrate with a box measuring  $0.5 \times 7 \mu\text{m}$  with a voltage of 30 keV and a current of 0.3 nA.
9. At a tilt of  $22^\circ$ , cut through the right side of the foil with a box measuring  $0.5 \times 5 \mu\text{m}$  with a voltage of 30 keV and a current of 0.3 nA, being sure to leave the top attached.

10. Tilt to  $0^\circ$ . Insert the Omniprobe *in situ* manipulator and attach the probe to the free end of the foil using Pt deposition at a voltage of 30 keV and a current of 0.1 nA.
11. At a tilt of  $0^\circ$ , cut the attached edge of the foil free from the substrate at a voltage of 30 keV and a current of 0.1 nA.
12. Attach the lifted out foil to a Cu Omniprobe grid using the Pt deposition at a voltage of 30 keV and a current of 0.1 nA.
13. Cut the Omniprobe free from the foil at a voltage of 30 keV and a current of 0.1 nA.
14. Compucentrically rotate the foil  $-135^\circ$  and deposit Pt along the back edge of the foil, connecting to the Cu Omniprobe, grid at a thickness of 500 nm at a voltage of 30 keV and current of 0.1 nA.
15. Tilt to the angle at which the TEM foil is normal to the ion column (approximately  $52^\circ$ ) and insure that the scan rotation is set to  $180^\circ$ .
16. Tilt  $-1.5^\circ$  relative to the normal and thin the bottom of the foil using a 'Cleaning Cross Section' measuring the length of the foil by 200 nm, starting from the bottom and working upwards, at a voltage of 30 keV and a current of 50 pA. Using the 'Cleaning Cross Section' for the thinning process was found to produce more uniform foils, as compared to traditional rectangle cuts.
17. Tilt  $1.5^\circ$  relative to the normal and thin the top of the foil using a 'Cleaning Cross Section' measuring the length of the foil by 200 nm, starting from the top and working downwards, at a voltage of 30 keV and a current of 50 pA.
18. Repeat Step 16 and Step 17 until the thickness of the foil is approximately 150 nm.

19. Tilt  $-1.5^\circ$  relative to the normal and scan over the length of the TEM foil using a voltage of 5 keV and a current of 0.23 nA. This has been found to clean some of the damage done from thinning.
20. Tilt  $1.5^\circ$  relative to the normal and scan over the length of the TEM foil using a voltage of 5 keV and a current of 0.23 nA.
21. Remove the foil attached to the Omniprobe grid from the FIB and load it into the Gatan PIPS.
22. Using a voltage of 2.5 keV and a top and bottom angle of  $8^\circ$ , the PIPS was utilized for 6 minutes in order to remove any residual FIB